Electronic Thesis and Dissertation Repository

10-9-2020 2:30 PM

Experimental Modelling of Downburst and Downburst line Outflows

Kyle Graat, *The University of Western Ontario*

Supervisor: Savory, Eric, *The University of Western Ontario*
A thesis submitted in partial fulfillment of the requirements for the Master of Engineering
Science degree in Mechanical and Materials Engineering
© Kyle Graat 2020

Follow this and additional works at: https://ir.lib.uwo.ca/etd

Part of the Other Mechanical Engineering Commons

Abstract

The outflow velocity vector fields of simulated stationary thunderstorm downbursts and downburst lines were resolved in two plane orientations, vertical and horizontal, using a dense fluid release system and Particle Image Velocimetry. Single event releases were scaled to show agreement with past studies based on radial velocity magnitude and location and radial and vertical front propagation. The vortex trajectory of a single event using the vortex aspect ratio supported density's role in the outflow after the time and location of the maximum radial velocity. The interaction between two release events varied temporally and spatially and showed that the interaction region's lateral outflow produces the highest velocities of up to 1.5 times that of a single event while velocities in the vertical plane remained unaffected. Scaled separation distances greater than 3 km produce weak outflow interactions with no increased velocities beyond those of a single event.

Keywords

Thunderstorm outflow, downburst, microburst, burst swath, downburst line, Particle Image Velocimetry, dense fluid release, baroclinic vorticity, Experimental Fluid Mechanics

Summary for Lay Audience

Thunderstorms can produce high wind velocities from strong downdrafts know as downbursts. Downbursts produce strong near-ground wind flows that pose a structural aviation engineering hazard that must be designed for. These hazardous winds were modelled at a reduced scale using a dense fluid release cylinder. An imaging technique called Particle Image Velocimetry was used to capture the outflow's velocity from the release cylinder. Single release events were found to compare to past studies based on the location and value of the highest near-ground velocities and the descent and spread of the outflow. The system was expanded to include a second cylinder to explore the velocities produced in the collision region of two release events with the second event released at different times and over different separation distances. Outflow collisions spaced far apart were found to exist as individual events where the near-ground velocities are no higher than a single event, and the vortices meet to lift each other upwards to create elevated vertical velocities. Outflow collisions from events spaced close together and released close in time produced high ground velocities that, with values up to 1.5 times that of a single event and vortices that are forced to remain close to the ground.

Dedication

This thesis is dedicated to my late Grandmother, Matilda Graat, who gave me her pure unconditional love.

Acknowledgments

I would like to thank my supervisor, Dr. Eric Savory, for his unwavering support and guidance throughout this project's long journey. I would like to thank Dr. Savory for believing in my capacity and for providing the opportunity to push my limits, make mistakes, and grow as a professional.

I would like to thank Ron Struke of the Western Engineering Faculty Electronics Shop for his invaluable electronics and programming help, lab manager Walid Altahan for supporting the hydraulic flume facility, and Dan Sweiger from the University Machine Services for helping design and build the required mechanical parts.

I would like to thank Rose Babaei Koli for her initial help in introducing the experimental technique, Shivani Ashitkumar Jariwala, for her help in running experiments and Alex Coote for his help with the initial set of experimental runs.

Table of Contents

List of Tables

List of Figures

Nomenclature

C_d	Diameter of the releases cylinder	[m]
C_x	Circcumfential arc segment	[m]
D_c	Diameter of the cylinder	[m]
g	Acceleration of gravity	[m/s^2]
H	Hight of the release cylinder	[m]
K_1	Nondimensional scale factor for u_{ave}	
K_2	Nondimensional scale factor for u_{rms}	
Q	Release cylinder volume	[cm^3]
r	Radius of the release cylinder	[m]
R	Radial distance from a release event centre	[m]
R_0	Characteristic length	[m]
t	Time	[s]
T	Scaled time	
T_0	Characteristic time	[s]
T_{min}	Time at the lowest point in vortex trajectory	[s]
T_{max}	Time at the maximum radial velocity	[s]
ΔT	Time delay	[s]
ΔT_v	Physical time step size	[s]
ΔT_{0v}	Nondimensional time step size	[s]

u	Horizontal velocity in the x-z plane	[m/s]
u_{rms}	Fluctuating radial velocity about the mean	[m/s]
u_{ave}	Mean radial velocity	[m/s]
u_{scaled}	Circumferentially scaled radial velocity	[m/s]
v	Vertical velocity in the x-z plane	[m]
v	kinematic viscosity	[m^2/s]
V	Velocity magnitude	[m/]
V_0	Characteristic velocity	[m]
V_{max}	Maximum in-plane velocity	[m]
w	Velocity in the x-y plane	[m]
$w_{ambiant}$	Mass of the ambient fluid	[%]
w_{dense}	Mas of the dense fluid	[%]
X	Horizontal dimension from origin	[m]
X_d	Release cylinder separation distance	[m]
X_{min}	Horizontal dimension of vortex core's min height	[m]
Y	Vertical dimension in the x-y plane	[m]
Z	Vertical dimension above the ground plane	[m]
Z_{min}	Vertical dimension of vortex core's min height	[m]
Z_f	Dense fluid leading boundary during descent	[m]
Z_{f0}	Initial height of the dense fluid leading boundary	[m]

δ_L	Threshold value for λ_2 in vortex core width	
δ_λ	Threshold value for λ_2	
λ_2	Lambda Criterion	
ρ	density	$[kg/m^3]$
$\Delta \rho$	Difference in density	$[kg/m^3]$

Chapter 1

1   Introduction

Thunderstorms are a common climatological phenomenon that inflicts damage through lightning, hail, flooding, and strong wind fields in the form of tornados and straight-line winds (Byers and Braham, 1949). Of all these, straight-line winds cause an estimated 40% of the damage caused by thunderstorms (Ashley and Mote, 2005; Metz and Bosart, 2010) and are responsible for the most widespread destruction of transportation, infrastructure, and the environment (Fujita and Wakimoto, 1981; wakimoto, 2001; Johns and Hirt, 1987). Damaging straight-line winds diverge in a uniform direction above speeds of 90 km/h or 25 m/s and are associated with burst swaths from the downdraft portion of the convective cycle in a thunderstorm as microburst and downbursts (Byers and Braham 1949, Fujita 1985, Wolfson 1988). Understanding the near-surface flow field and associated straight-line winds produced by downdrafts by the use of scaled experimental models is critical to creating guidelines for engineers in establishing wind loads in designing infrastructure.

1.1   Downbursts and Downburst Lines: Their Origin

A Downburst was initially defined as an intense downdraft was the rate of descent of its constituent air parcel(s) were equal to or greater than that of 3.6 *m/s* at 91 *m* of elevation, a rate equivalent to that of a landing airplane, which was determined to be a velocity high enough to pose as an aviation hazard (Fujita and Caracena, 1977). The term was created by Dr. Fujita to distinguish the level of hazard present in the wind fields observed from thunderstorm derived downdrafts much the same for which was done for tornados with the Fujita scale (Fujita, 1971). The definition was later refined for use in meteorology: a downburst is a downdraft that has a characteristic impinging divergent outflow of locally intense straight-line winds (burst swaths) that can exceed 40 *m/s* at a radial extent of up to 4 km from the event center (Fujita, 1978, Wakimoto 2001).

Downbursts originate from the thermodynamic and kinematic processes within thunderstorms, meteorologically referred to as Deep Moist Convection Systems (DMCs) (Doswell, 2000). In general, moist warm air ascends upwards to the troposphere, which creates a distinctive Cumulonimbus cloud structure and mixes with cooler air. A combination of temperature and pressure differences force moist air to condensate. The condensate builds a pool of dense cold air. As the cool, dense air increases in mass, it starts to descend as a strong, negatively buoyant plume or gravity head (Byers and Braham, 1949; Wakimoto, 2001). A combination of precipitation drag and boundary shear influence the falling mass as it matures from a downdraft into a downburst (Fujita, 1985). The interaction between the dense falling air and surrounding atmosphere induces a vortex ring (Figure 1-1) to form as the air mass reaches the ground.
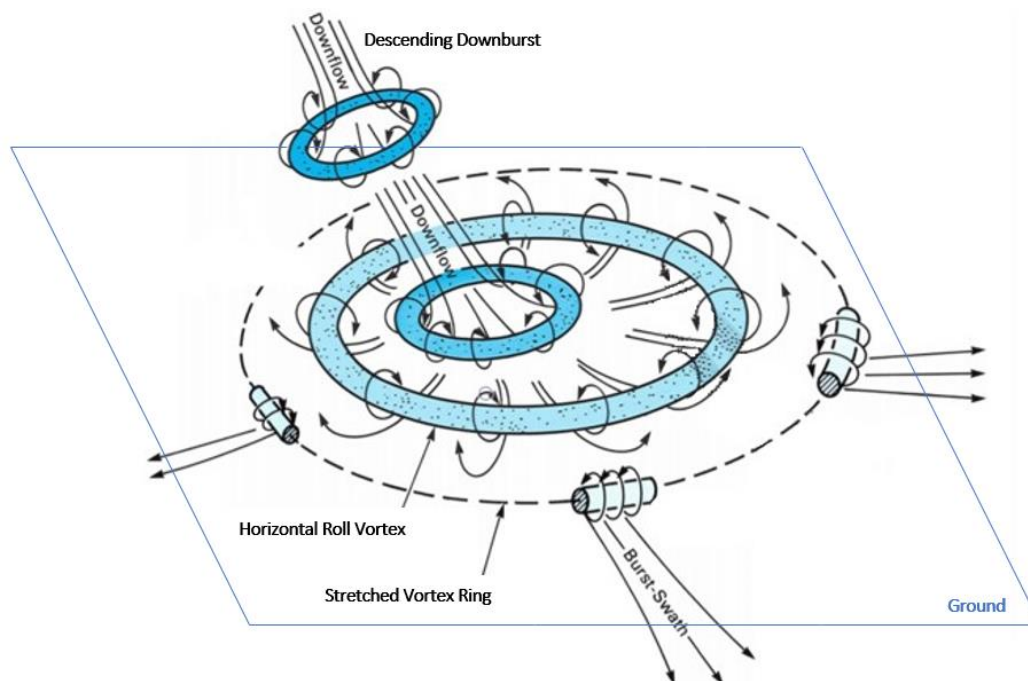
Figure 1-1 – Main flow features of a downburst vortex ring (adapted from Wolfson, 1988)

Once a downburst strikes the ground, the vortex ring spreads out radially, breaking down into runaway vortex rolls, and the residual downflow continues to maintain the event until the total mass sinks onto the ground and losses its momentum (Fujita, 1985). The vortex ring interaction with the ground creates the characteristic straight-line wind damage (from burst-swaths) observed from downburst events (Figure 1-2 and Figure 1-3).

Figure 1-2 – Tree damage, red arrows showing downed trees from a gust front, the blue arrows show downed trees from a downburst (Taszarek et al., 2019)
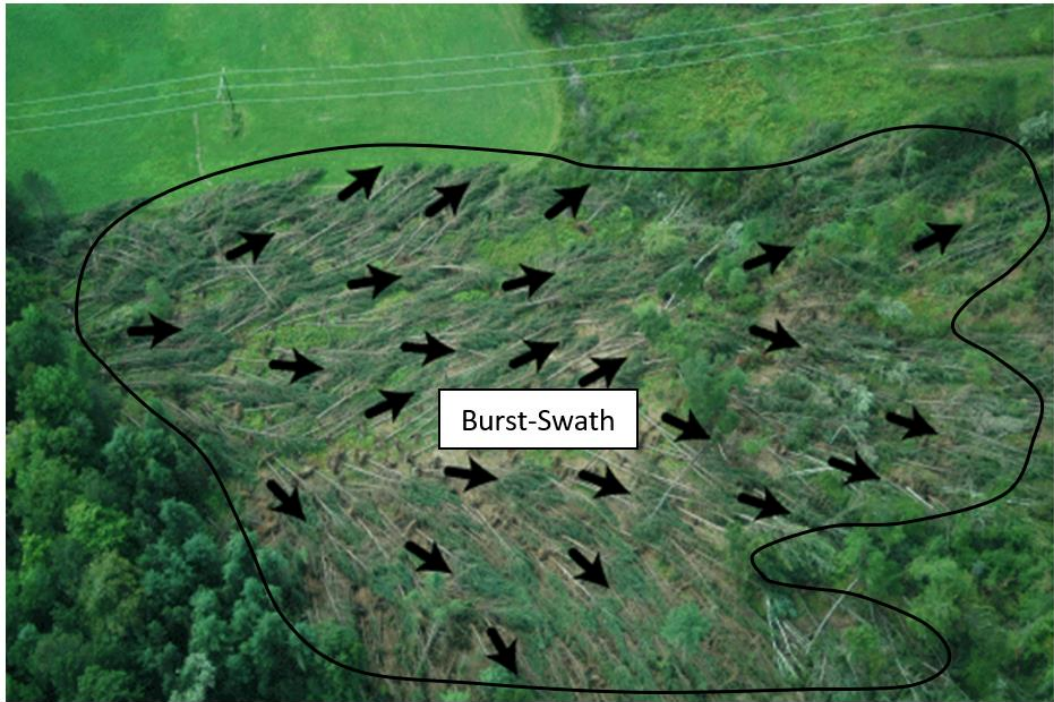
Figure 1-3 – Burst swath damage of trees, the direction shown by arrows (Atkins, 2010)

The interaction with the ground forces the vortex ring to stretch and convect along the ground, before dissipating, due to continuous vorticity generation as the rest of the dense air mass continues to fall into the ground. This convection and stretching adds strength to the vortex structure and amplifies the near-surface radial velocity. A secondary vortex close to the ground plane (Yao and Lundgren, 1996) also results in a highly complex wind field. Buoyancy forcing (referred to as baroclinic vorticity generation) is the mechanism for this continuous vorticity generation. Eq. 1-1 expressed by Maekowski and Richardson (2010), describes this mathematically:

$$\frac{\partial \vec{\omega}}{\partial t} = -\left(\vec{v} \square \nabla\right)\vec{\omega} + \left(\vec{\omega} \square \nabla\right)\vec{v} + \frac{1}{\rho^2}\nabla\rho \times \nabla\rho + \nabla \times F \qquad \text{1-1}$$

Applying the Boussinesq approximation to replace the initial density term in all the momentum equations except in the numerator of the buoyancy term of the vertical momentum equation and neglecting the viscous effects, Maekowski and Richardson (2010) showed that the vorticity simplifies to:

$$\frac{\partial \vec{\omega}}{\partial t} = \left(\vec{v} \square \nabla\right)\vec{\omega} - \left(\vec{\omega} \square \nabla\right)\vec{v} + \nabla \times B + \nabla \times F \qquad \text{1-2}$$

where B is the buoyancy term. Considering only the y-component (noted as η) (Vermeire et al., 2011b) leads to:

$$\frac{\partial \eta}{\partial t} + \left(\vec{v} \square \nabla\right)\eta = \left(\vec{\omega} \square \nabla\right)\vec{v} - \frac{\partial B}{\partial x} \qquad \text{1-3}$$

The above term represents the horizontal y-component of vorticity, which defines the formation of the ring vortex structure. The x-component represents the same description, but in the x-direction and can be ignored for understanding. The two terms on the right-hand side detail the distribution and production of vorticity. Following the order as written, the first term describes the stretching of vorticity about the y-axis and vorticity's tilting about the x or z axes. The second term represents the production of vorticity due to buoyancy forcing (baroclinic vorticity generation). The other terms only describe the distribution of vorticity as generated by other mechanisms.

Downburst simulations performed in Vermeire et al. (2011b) showed that the stretching term becomes significant after impingement, around less than 0.5 *km* above the impinging surface. The stretching and tilting of vorticity have little influence in the evolution of a downburst when it is aloft but becomes more critical in the near-surface outflow. Vermeire et al. (2011b) concluded that the buoyancy forcing term is the only significant vorticity production term present. Therefore, the buoyancy gradient's strength dictates the production of vorticity and affects the strength of the circulations in the flow and their resulting vortex structures. As a result, the wind speed profile in a downburst outflow is much different from well-studied synoptic winds (Figure 1-4).
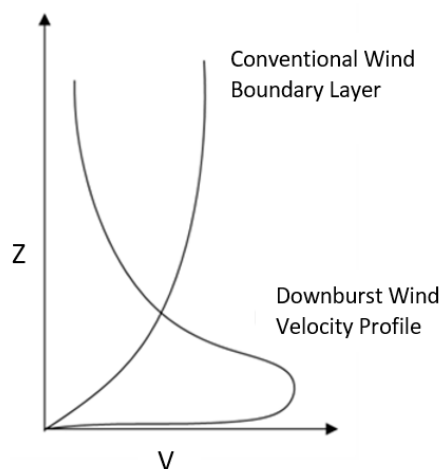
Figure 1-4 - A conventional wind speed boundary layer from synoptic winds compared to the wind speed profile generated by thunderstorm downbursts (adapted from Vermeire, 2011)

Higher velocities near the ground occur due to the passing roll vortex compared to that of synoptic winds. A stationary observer would experience a transient load with a sharp horizontal gradient in horizontal velocity as the roll vortex passes. This transient loading is caused by the sharp horizontal velocity gradient that is of interest to wind and structural engineers. The region, outside the initial contact and just after the roll vortex reaches the ground, are where the highest velocities, between 30 to 92 *m/s*, have been reported in nature, as well as experimentally and numerically (Fujita, 1981; Fujita, 1985; Wakimoto, 2001; Vermeire et al., 2011; Orf et al., 2012; Oreskovic, 2016). The dynamic interaction between atmospheric conditions and the thermodynamic process that generates downbursts leads to different types and scales of downbursts.

Downbursts are subdivided into two distinct scales of events, microburst or macrobursts, depending on the extent of damage incurred (Fujita, 1990). A microburst has damaging winds that can extend up to 2.5 miles and have horizontal wind gusts going up to 75 *m/s*, while macrobursts have damage fields over 2.5 *miles* with a horizontal wind speed of 60 *m/s*. The additional classification considers that the speed of the horizontal outflow and the scale of damage is dependent on the complex interaction between the volume of the cold air, its density distribution, and the effect of shear during descent (Fujita, 1974). Fujita and Wakimoto (1981) further classified downdrafts into five distinct scales (Figure 1-5) depending on their damage patterns as they relate to their respective parent storm (Fujita and Wakimoto, 1981). Their study's result was a suggested scale that started with the full-scale downburst producing storm, the family of downburst clusters or the derecho and reduced in size to the smallest observed damage pattern created by a singular microburst event. A derecho will contain some or all of the scales of downburst events.

MISO-scale		MESO-scale		MASO-scale
100m	1000m	10km	100km	1000km
MISO-β	MISO-α	MESO-β	MESO-α	MASO-β
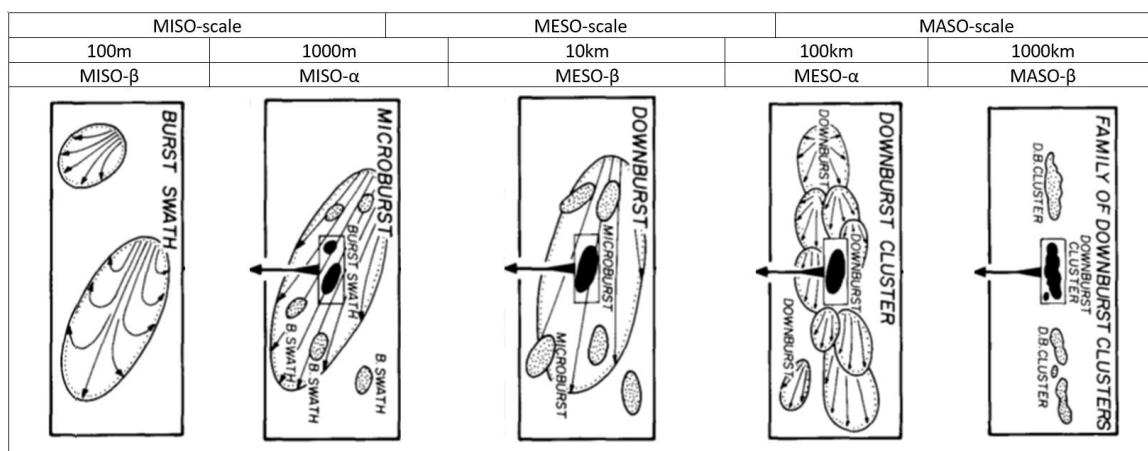
Figure 1-5 – Five scales of outflow associated with thunderstorm downbursts (adapted from Fujita, 1981)

The scale begins at the Maso-scale (known as Maso-beta, Figure 1-5), in the 1000's of km range, which encompasses the whole storm (derecho, squall-line, a family of downburst clusters). Below the Maso-scale are the Meso-scale and Miso-scales, each sub-reduced into alpha and beta to go from the 100's *km* range to 10's *m* range with the smallest wind damage being burst swaths from the vortex ring outflow. The research presented will focus

on downburst lines formed in the alpha Meso-scale (in the 100's *km* range; downburst clusters) and outflow characteristics in the smallest scales, the Meso-β scale. In addition to scale, Fujita (1990) expanded the classification of downburst into types. Downburst events can vary in size from Macrobursts with damaging winds at speeds of 60 *m/s* that spread beyond 4 *km* in horizontal extent and last for 30 min, to Microbursts with a damaging length less than 4 *km,* but wind speeds up to 75 *m/s* that last for 2 – 5 *min* (Fujita, 1990). The types continue with Mid-air, twisting, ground, and dry downburst (Fujita, 1990). The classification of scale and type paired with the physical process that led to the definition of a downburst were formed from field studies.

1.2   Literature Review

Section 1.2 is a review of past studies that fall into one of three primary methods for investigating the flow fields of downbursts and downbursts lines: field measurements of full-scale downburst outflows, laboratory recreated downbursts and downburst outflows, and numerically simulated downbursts. Section 1.2.1 provides a review of downburst field studies, and section 1.2.2 details the wind engineering models used to simulate downbursts with a discussion on limitations of each technique. Section 1.2.3 reviews past field measurements and numerical studies on downburst lines and clusters.

1.2.1   Field Studies of Downbursts

Field studies conducted throughout the 1970s and 1980s identified the main characteristics of downbursts and downbursts lines outflows. Projects in the United States of America, such as the Northern Illinois Meteorological Research on Downburst (NIMROD (Fujita, 1978)) and the Joint Airport Wind Shear project (JAWS (McCarthy et al. 1982)), developed a majority of the information used to define the wind fields of downburst events. NIMROD was initiated in 1978. Three DOPPLER radar stations placed 60 Km apart in a triangular pattern west of Chicago investigated thunderstorm outflows between 15 May 1978 and 30 June 1978. Fifty events were recorded with horizontal wind speeds reaching 31 *m/s* above

45 *m* from ground level (Wilson and Wakimoto, 2001). The spacing of the DOPPLER units was found to provide limited resolution, which impacted the detail of which downburst outflows could be studied.

The JAWS project was launched in Denver, Colorado, on May 15, 1982, as a follow-up to the discoveries made in project NIMROD, with DOLPPER closer spacing between 15 and 28 km. A data set of 186 downbursts resulted and was featured in notable works by Hjelmfelt (1987, 1988), Wilson et al. (1984), Proctor (1989). Figure 1-6 is a pictorial summary of the JAWS downburst anatomy analyzed by Hjelmfelt (1988).
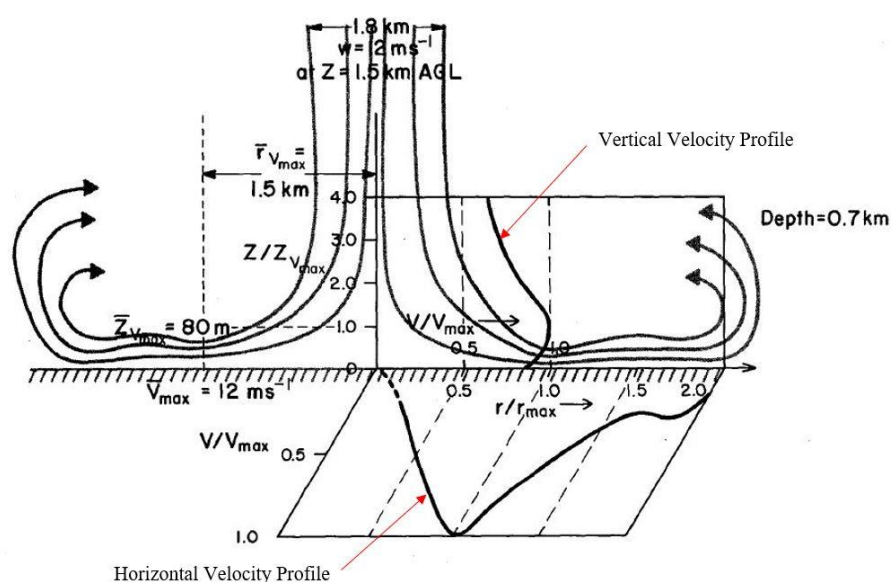
Figure 1-6 - The definition of the critical velocity profiles in a downburst outflow (Adapted from Hjelmfelt, 1988)

The significant finding in JAWS was that high based clouds could produce strong downburst outflows, significantly when aided by precipitation (Proctor, 1988). Proctor (1989) and Wakimoto (1994) provided further support or a precipitations role in the thermodynamic influences that increased the strength of downburst outflows. Since these two landmark field studies, additional studies such as Microburst and Severe Thunderstorms (MIST) (Orville et al. 1989), Wind Engineering Research Field Laboratory (WERFL) (Lambardo et al., 2014) and field studies in Europe (Duranona et al., 2006; Jarvi

et al., 2007; Solari et al., 2015), and studies from Australia (Greets, 2001; Rowcraft, 2014) have continued to add to the field data of downburst outflows. From a wind engineering perspective, these studies highlighted that thunderstorm downburst outflows produce transient wind fields (Goff, 1976) with different profiles from synoptic winds (Letchford and Chay, 2002; Vermeire, 2011; Solari, 2019). Field Studies place a heavy reliance on radar and probe stations placed over large areas in regions where downbursts are suspected to occur. Vast distances between measurement locations have limited the spatial and temporal resolution that radar-based studies have, as noted in NIMROD (Fujita, 1979), especially in the near-surface region of the discharge (Alahyari and Longmire, 1994). While the studies served to provide an insight into the outflow of thunderstorm downbursts, their primary focus was on the meteorological aspects more so than the near-surface transient wind loading. The wind engineering community is interested in how the strong transit horizontal wind loads affect structures; wind engineers have developed a series of models to aid in this investigation.

1.2.2   Wind Engineering Models of Downbursts

The wind engineering community has developed a series of numerical and experimental methods to investigate the near-surface region of thunderstorm downburst wind fields. Within these, two main approaches have arisen: simplified models using axial jets and more sophisticated approaches using density and buoyancy. The axial jet model replaces any influence that the thermodynamic processes and buoyancy have on the formation and development of downburst outflows with an impulse jet (Letchford and Chay, 2002; Zhang et al., 2013). Approaches that use density and buoyancy focus on recreating the physics behind downburst outflows with emphases on modelling baroclinic vorticity generation (Vermeire et al., 2011).

Along with these two primary approaches, two other models, the vortex ring and the slot jet model, also exist. The Ring vortex model (Ivan, 1986; Schultz, 1990; Jesson and Sterling, 2018) replicates the vortex ring along the ground plane only over creating the entire outflow by a descending air mass (Chen and Letchford, 2004). The vortex ring model

was shown to model the main flow features in a downburst outflow to an appropriate degree of accuracy (Jesson and Sterling, 2018). However, the impinging jet model has shown to be better than the vortex ring model at predicting the radial outflow of downbursts (Holmes and Oliver, 2000; Savory et al., 2001). The slot jet also referred to as a wall jet, reduces the downburst's analysis to only the outflow.
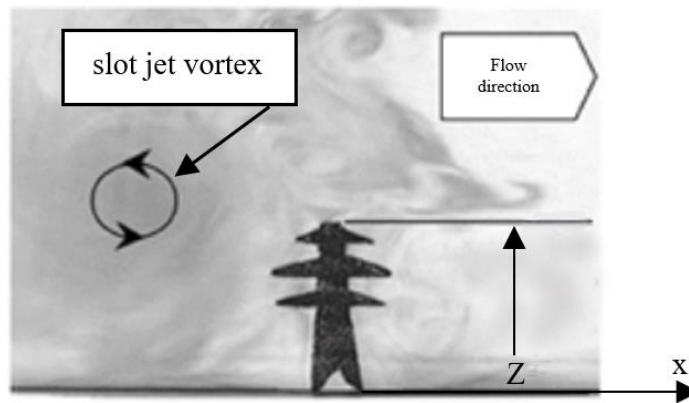
Figure 1-7 – Example of a horizontal vortex roll produced by a slot jet in a boundary layer wind tunnel (adapted from Lin et al., 2007)

The slot jet utilizes a flow through a slot along the floor of a boundary layer wind tunnel (Figure 1-7) (Lin and Savory, 2006; Lin et al., 2007; Lin and Savory, 2010). As a result, a better resolution of the near-surface region of the outflow is achieved. However, this model was found not to reproduce the vortex structure as the primary vortex lifts from the surface. This lift does not model the dynamic separation reattachment that has been postulated as an essential feature (Mason et al., 2005). Like the vortex model, the neglect of the three-dimensional flow structures of a downburst outflow limits the slot jet compared to other techniques (Lin and Savory, 2006).

The impinging jet model (IJ) was first proposed by Fujita (Fujita, 1985) and later featured in the work of Hjelmfelt (1987) and Proctor (1988, 1989). Proctor (1988) used an axisymmetric numerical model to simulate the thermodynamics and microphysics that form downburst outflows. Proctor's (1988) study found that the instantaneous vertical profiles of the outflow matched well with the NIMROD (Fujita, 1978) data and laboratory experiments of steady impinging jets (Bakke, 1957). Since then, the impinging jet model

has evolved to use impulsively driven axis-symmetric circular jets to impinge on the ground plane (Landreth and Adrian, 1990; Zhang et al., 2013). Landreth and Adrian (1990) measured the outflow of an impinging jet over a flat surface showing the preliminary application to thunderstorm outflows.
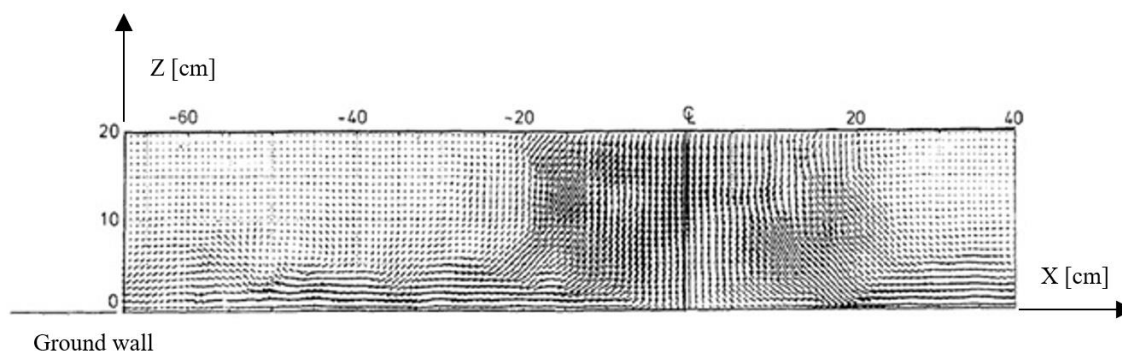
Figure 1-8 – PIV velocity vector field example of a low Re number impinging jet (adapted from Landreth and Adrian, 1990)

The IJ experiment by Landreth and Adrian (1990) was able to show that an impulse IJ model could develop the same outflow characteristics of a downburst. These included the formation of the secondary vortex, as seen in Figure 1-8.

Experiments by Chay and Letchford (2002), Mason et al. (2005), Xu and Hangan (2008), McMonville et al. (2009), Chowdhury (2018) and Romanic and Hangan (2019), in addition to numerical simulations by Wood et al. (2001), Kim and Hangan (2007), Sengupta and Sarkar (2008), Mason et al. (2009), Adb-Elaal et al. (2013), and Zhang et al. (2013), have shown the IJ model to produce agreeable velocity profiles upon impingement to full-scale downbursts. Holmes and Oliver (2000) and Wood (2001) have proposed empirical models based on a steady circular wall jet to offer a simple means of predicting a downburst's outflow characteristics from the impingement centre up to the region of the maximum radial velocity.

Although the impinging jet model can produce similar velocity profiles in its outflow that match field data, the transient features of an impinging jet flow compared to those of real downbursts remain unknown (Zhang et al. 2013). The NIMROD project (Fujita, 1978; Hjelmfelt, 1988) extracted the vertical and horizontal velocity profiles from Doppler radar

data with a scanning time of 2-15 *min* (Lin et al., 2007). The radar scanning time was significant relative to the downburst duration (< 5 *min*), and therefore the transient nature of the outflow velocity was missed (lin et al., 2007). The fact that the IJ model compares well with the NIMROD data could be a reflection of only capturing the average or mean velocity profiles over the instantaneous velocity profiles. Xu and Hangan (2008) studied the sensitivity of axis-symmetric jets to the Reynolds number, impingement boundary conditions, and the inlet conditions. They found that the surface velocity field is Re dependent, and the nozzle to ground distance for heights less than the vortex ring formation length produce higher maximum radial velocities. Kim and Hangan (2007) that higher Reynolds number forces the location of the maximum radial velocity outward from the jet centre and lower to the ground plane. Kim and Hangan (2007) also established that the maximum speeds are achieved at the height of less than 5% of an axial jet inlet diameter. Laboratory axil jet models need to have large outlet diameters (>0.2 m) to enable enough room for measuring the near-surface velocity in the outflow. This scale leaves the Jet model subject to confinement effects (Xu and Hangan, 2008). The WindEEE facility (Figure 1-9) was developed to overcome the limitations on scale and confinement.
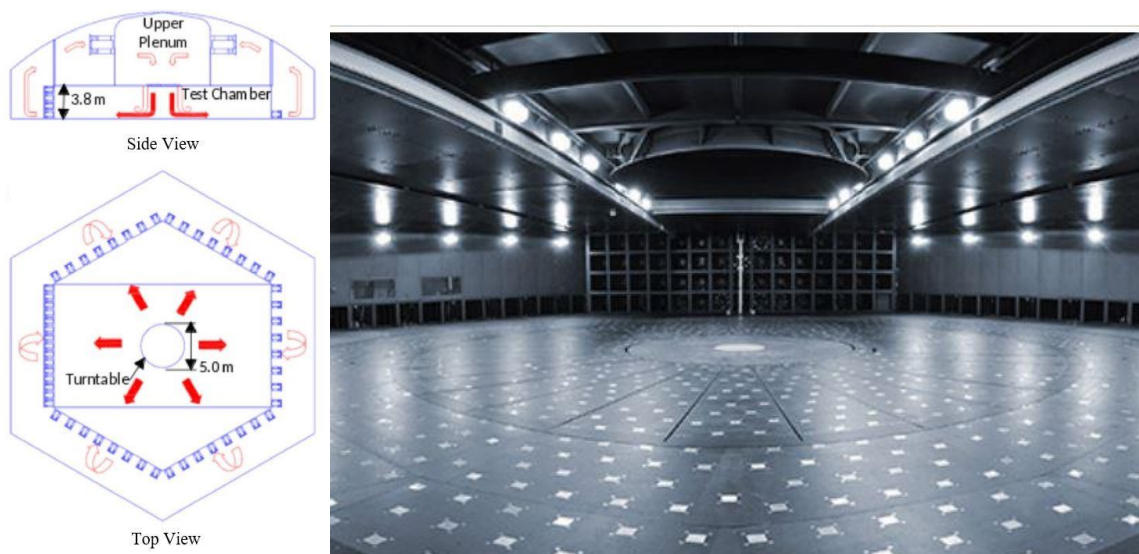
Figure 1-9 – Schematic and pictorial overview of the IJ producing section of the WindEEE facility (adapted from Romanic et al., 2019) retrieved from https://www.eng.uwo.ca/windeee/media_photo.html

Work by Chowdhury (2018), Romanic and Hangan (2019), and Romanic et al. (2020) have used WindEEE to investigate the transient outflow features of the IJ model. Chowdhury (2018) and Romainc et al. (2020) have shown improved scaling methods to natural downbursts that include the IJ model's transient features. Chowdhury (2018) also demonstrated the use of the roll vortex trajectory as a possible scaling method. Despite these developments, limitations still exist in the IJ model.

Kim and Hangan (2007) performed Unsteady Reynolds-Averaged Navier-Stokes (URANS) simulations of an impinging jet and found that the outflow vortex ring was formed by a Kelvin-Helmholtz instability at the shear interface between the nozzle and ambient fluid, which has not been observed in downburst events. Zhang et al. (2013) compared the PIV results of an experimental axial jet model to numerical results of a cooling source model downburst. They concluded that the axial jet model could not reproduce the instantaneous radial velocity profile at the maximum wind speed condition compared to field study data. Also, Zhang et al. (2013) found that the axial jet model produces a vortex ring that propagates in a wavy fashion were as in other models (such as the cooling source and two-fluid density model), the vortex ring spreads at a constant height (Alahyari and Longmire, 1995).

Numerical simulations overcome the limitations of spatial and temporal resolution and include the physical process responsible for forming a downburst. Anderson et al. (1992), Orf and Anderson (1996) and Orf and Anderson (1999) introduced a dry sub-cloud model called the Wisconsin Model Engine (WME). They imposed thermal forcing through an ellipsoidal Cooling Source (CS) function. The CS function is prescribed parameters that model the microphysical processes that form downbursts in nature. The CS function is imposed as the cosine squared of the distance from the centre of this region. This cooling intensity generates the negative buoyant mass that drops and impinges on the ground as a downburst (Figure 1-10). Small flow structures, the complexities of colliding outflows, and the effect of precipitation on the outflow strength have all been studied with high resolution using this model.
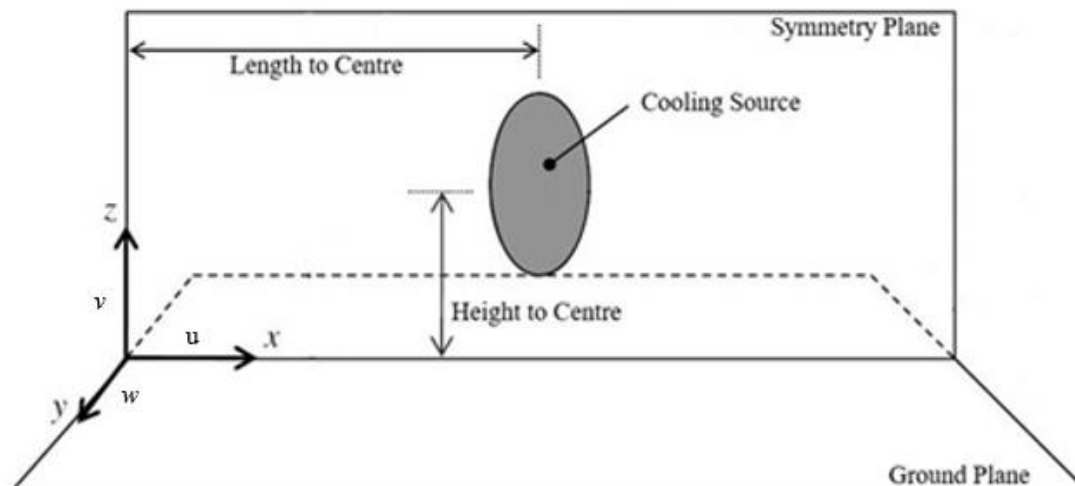
Figure 1-10 – Overview of a CS numerical domain (adapted from Mason et al. 2010)

Lin et al. (2007) applied the same CS forcing function approach with the more sophisticated Cloud Model 1 (CM1) (Bryan and Fritsch, 2002), designed for high-resolution numerical studies of deep moist convection systems. Orf et al. (2012), Vermeire et al. (2011a,b) Oreskovic (2016) have presented further CS simulations based on CM1. Orf et al. (2012) used the CS approach based on CM1 to model the effect that snow, graupel, and precipitation had on the strength of a downburst outflow (Figure 1-11). Orf et al. (2012) proposed a circumferential averaging model for the nonuniform outflow of CS simulations. They proved that axisymmetric models, though idealized, are still useful in estimating the peak radial velocity. Vermeire compared the CS model based on CM1 to an impulsively driven IJ and found that the IJ model could not capture the buoyancy-driven effects found in downbursts.
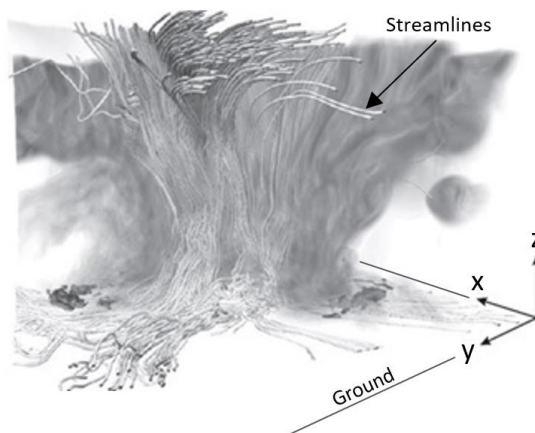
Figure 1-11 – Example of a high-resolution CM1 based numerical downburst with stream tubes of steady wind, and gray Isosurfaces enclosing winds exceeding 25 *m/s* (adapted Orf et al., 2012)

The CS numerical approach has also been used with less sophisticated numerical schemes. Mason et al. (2009) used Unsteady Reynolds-Average Navier-Stokes (URANS) simulations on a commercial software package to simulate how various physical CS parameters affected the simulated outflow. Zhang et al. (2013) also employed URANS for simulating a downburst outflow using the CS approach. Zhang et al. (2013) demonstrated that the CS numerical model was better at reproducing the instantaneous radial velocity profiles and at representing the transient features of the primary vortex compared to the IJ model.

Although the CS numerical approach has demonstrated ability in modelling downburst outflows, like all numerical models, it is still highly dependent on the initial conditions. Mason et al. (2009) observed that the shape of the CS and other parameters, such as the ramp-up function and the elevation of the CS, have a significant effect on the outflow vortex development. Also, the physical dimensions and shape of the cold source within actual downburst-producing thunderstorms vary widely, and few CS studies have investigated this variation and its effect on scaling CS simulations. Oreskovic (2016) was able to show that the CS models are scalable in a similar way to IJ models and scalable to the Lundgren et al. (1992) dense fluid release scaling parameters.

The central concept behind the CS numerical approach is hard to model experimentally, limiting researchers' ability to validate the model. However, an analogous laboratory scaled experiment does exist. The two-fluid experimental simulations recreate negative buoyancy by releasing a more-dense salt-based solution into a less dense fluid (Lundgren et al., 1992; Alahyari and Longmire, 1994; Alahyari, 1995; Yao and Lundgren, 1996; Babaei, 2018). Lundgren et al. (1992) were able to show that the release of higher density fluid into a less dense fluid exhibited many of the aspects of a downburst. By comparison to flight DL 191 (Fujita, 1986), they produced a set of scaling parameters that scale dense fluid release events to full-scale data. Three basic scale dimensions (length scale, time scale, and velocity scale) were developed to characterize a release event (Equations 2.4-6):

$$R_0 = \left(\frac{3Q}{4\pi}\right)^{1/3} \tag{2.4}$$

$$T_0 = \left(\frac{R_0 \rho}{g \Delta \rho}\right)^{1/2} \tag{2.5}$$

$$V_0 = \frac{R_0}{T_0} \tag{2.6}$$

R_0 is the length scale based on the radius of the equivalent spherical volume, Q, of a release, T_0 is the time scale, and V_0 is the velocity scale, and g is the gravitation acceleration constant. An additional characteristic length scale, Z_0, the height from the ground plain to bottom of a release cylinder, is used to normalize the length scale. The Reynolds number is computed using the characteristic length and velocity scales (Eq 2.4 and 2.6) following the definition of Reynolds number:

$$\text{Re} = \frac{R_0 V_0}{v_a} \tag{2.7}$$

Were v_a represents the kinematic viscosity of the ambient solution. Lundgren et al. (1992) were able to show that the large scale turbulent primary and secondary vortex structures

were independent of the flow Reynolds number for large density differentials and release volumes (Re >3000).

Alahyari and Longmire (1994) and Alahyari (1995) applied Particle Image Velocimetry (PIV) to an improved version of the system from Lundgren et al. (1992). The PIV results confirmed that high outflow velocities were caused by the stretch of the horizontal vortex roll (Figure 1-12) (Alahyari and Longmire, 1995; Alahyari, 1995).
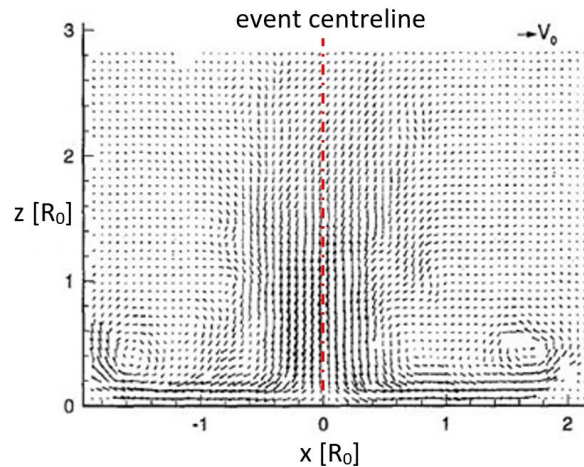
Figure 1-12 - PIV velocity vector field example from dense fluid release experiments (adapted from Alahyari and Longmire, 1994)

Yao and Lundgren (1996) showed the presents of a secondary counter-rotating vortex at the leading edge of the outflow caused by friction near the ground surface. They also showed that the later stages of the outflow match the characteristics of gravity currents. In particular, the outflow during the diverging stage has been shown to resemble the outflow during the inertial phase of axis-symmetric cylindrical gravity currents (Yao and Lundgren, 1996). The only difference is the lack of the dominant vortex structure near the leading edge of the outflow. Emphasis was provided on the radial outflow after the vortex ring has grown weaker and has lifted such that the leading edge of the outflow develops a nose. Babaei (2018) used an improved release cylinder design compared to the one used in Alahyari and Longmire (1994) and Yao and Lundgren (1996). Motor-driven top and bottom aperture gates replaced the membrane for initiating the release and improved repeatability. Babaei (2018) also found that the reduced wall porosity caused the outflow

from the new release cylinder to have increased mixing and a 23.2% reduced descent speed compared to a solid wall release cylinder. Figure 1-13 is an example of the Panner Laser-Induced Fluorescence capture of the outflow from the improved release cylinder design.

Figure 1-13 – PLIF image example of the outflow of the new cylinder design

Though this approach is used in this study, it should be noted that the technique is limited by scale. Lundgren et al. (1992) had a length scale between 1:9000 to 1:45000, and a velocity scale of 1:85, Alahyari and Longmire (1995) had a length scale of 1:25000, and a velocity scale of 1:300 and the Babaei (2018) had a length scale of 1:16000. These length and velocity scales are microscopic in comparison to numerical and IJ models and limit the resolution to which the near-surface region can be resolved. However, the buoyancy gradient can be reproduced as the primary force behind vortex generation over the Kelvin-Helmholtz instability in the IJ model. This aspect makes the use of the dense fluid release model more realistic over other experimental approaches.

A majority of these various experimental and numerical approaches have focused on modelling the outflow of single downburst events. Analysis of the JAWS data by Hjelmfelt (1988) noted that a thunderstorm's dynamics rarely resulted in only a single downburst event. Many downbursts can occur in a given storm and vary spatially and temporally such that their outflows interact. Fujita (1990) incorporated this into his classification of

downburst scales (Figure 1-5) and called them downburst clusters, referred hereafter to as downburst lines.

1.2.3   Downburst Lines

Beyond a singular event, more complex interactions can occur in the dynamic evolution of a thunderstorm leading to the outflows and associated vortex rings of two or more downbursts interacting; this leads to a significant increase in the level of wind hazard, as will be discussed later.

The interaction of downburst outflows can arise from particular types of thunderstorms. Thunderstorms form and organize into one of four specific events as they mature into large or mesoscale convective systems (MCSs) (Maddox, 1980): single cell, multicellular cluster, squall lines, and supercells (Faval and Daily, 1995). Multicellular groups and squall lines type events, known as Derechos, pronounced as Der-Ray-Cho (Hinrichs, 1888; Johns and Hirt, 1987), are of particular relevance as they are mostly downburst storms composed of a long line or a swath of multiple downburst events. In these storms, the highest surface wind speeds and largest damage footprints from downburst events have been observed (MacCarthy et al., 1982, H, 87 Hjelmfelt, 1987; Corfidi et al., 2015; Campbell et al., 2017).

Multicellular clusters and squall line type thunderstorms (Derechos) were noticed to produce multiple downburst events (Figure 1-14) in the Maso-scale and Meso-scale range, as related to the scale of airflow given by Fujita (1981) (Figure 1-5). These multiple downburst events can occur at a close range together, both spatially and temporally, forming downburst lines and clusters, and, at the largest scales, whole families of downburst lines and clusters (Fujita and Wakimoto, 1981; Hjelmfelt, 1987, 1988).
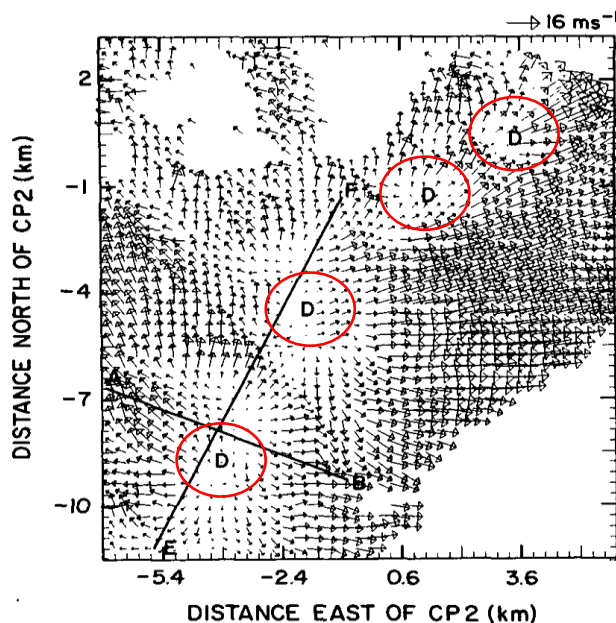
Figure 1-14 - Velocity vector field 50 m above the ground for a downburst line consisting of four individual downbursts (centres marked by D, circled in red) (adapted from Hjelmfelt, 1988)

Derecho's, are also referred to as long-lived convective windstorms (Coniglio and Stensrud, 2004) and bow-echoes (over just squall-lines). They primarily comprise families of downburst clusters and contain a frequent series of several or more downburst events over 400 km in length and span periods lasting for hours (Johns and Hirt, 1987). In the near-surface region, isolated areas of damaging winds called burst swaths are the primary mechanism for the observed surface damage. When the separation distance between individual downbursts within a downburst cluster is less than 4 km, each event's outflows interact, forming a downburst line (Hjelmfelt, 1988, Orf et al., 1996). The Joint Airport Weather Studies Project (JAWS) (McCarthy et al., 1982) and the Classify, Locate and Avoid Wind Shear Project (McCarthy and Wilson, 1986) both established that approximately 1/8th of all downburst events are downburst lines or clusters (Vermeire et al., 2011). Downbursts forming as multiple events increase the damage footprint and pose a more significant hazard over a singular event. A recent example of the possible extent of wind damage, based on the Fujita scale, from a Derecho in Poland in 2017, is shown in Figure 1-15.

Derechos have been responsible for over 153 deaths and insured/uninsured losses averaging over $100 million from wind damage in North America over nine reported storms between 1986 and 2003 (Ashley and Mote, 2005). A more recently derecho on 11 August 2017, in Poland (Figure 1-15), damaged 20,000 buildings, 9.8 million m^3 of lumber, and caused the death of 6 and injured 58 others with the financial impact unreported (Taszarek et al., 2019). This event highlights the scale of impact that downbursts and, in particular, downburst clusters have had. The morphology of a Derecho can help understand why they cover vast areas.
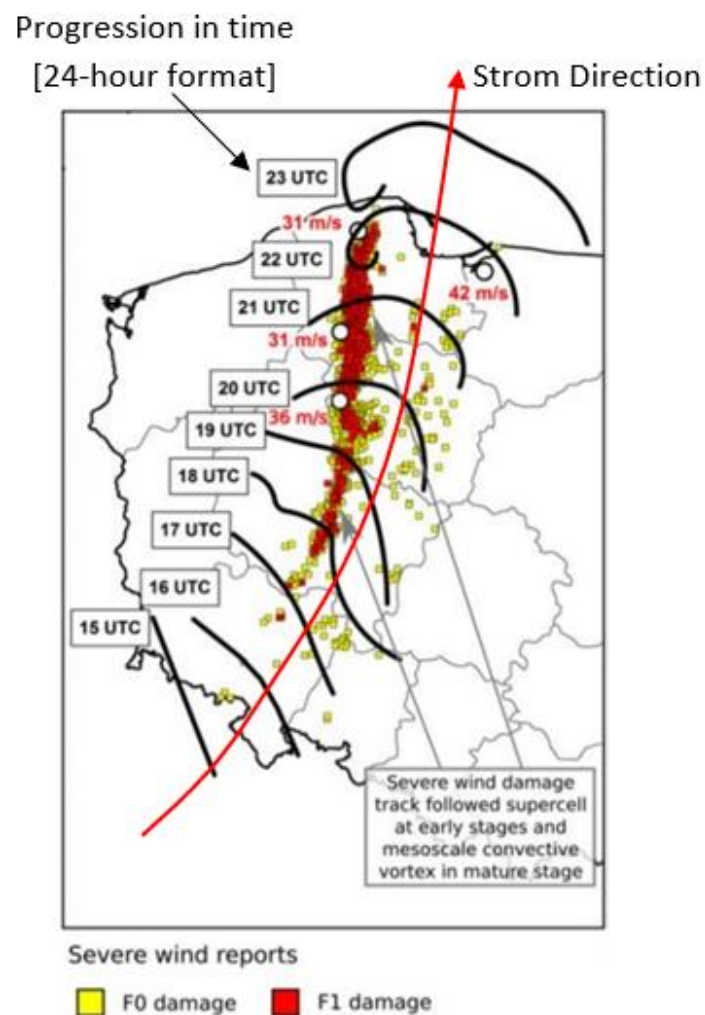
Figure 1-15 – Extent of wind speed reports of the Polish 11 August 2017 Derecho plotted with damage locations from wind speeds measured up to F1, bow eco shape indicated at different times by the black line (adapted from Taszarek et al., 2019)

Derechos are considered as a line of downstream-replicating ordinary thunderstorms that form as a type of mesoscale convective systems (MCS) (Zipser, 1982), explicitly known as derecho-producing convective systems (DCS) (Coniglio et al., 2010) and mature into large fronts of intense winds. These systems occur all year round with increased potency in the summer months (Johns and Hirt, 1987). A strong wind producing derecho can be distinguished into two basic types: serial and progressive. Serial Derechos form out of a moving low-pressure system with a strong mid-tropospheric flow causing a bow-echo of a short path and long width. In contrast, progressive Derechos form out of a short line of thunderstorms that orientate at an angle to the mean airflow progressing over a long path with a short width (Coniglio et al., 2004; Johns and Hirt, 1987).
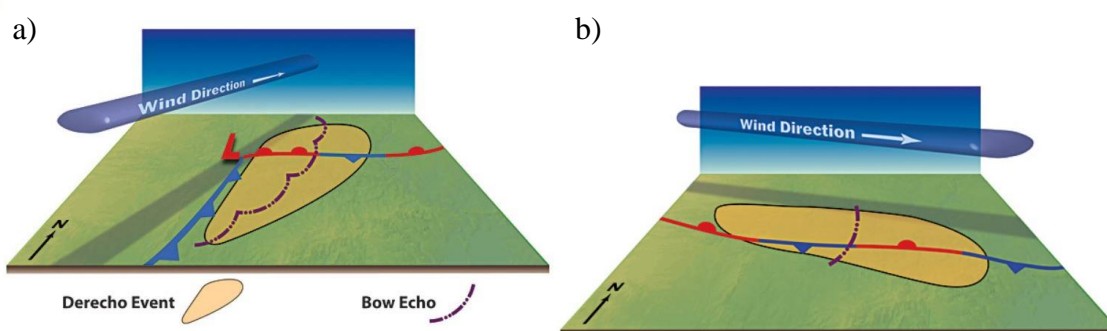
Figure 1-16 – Schematic of: a) Serial Derecho, b) progressive Derecho. NOAA, Types of Derechos, https://www.weather.gov/jetstream/derecho_types

In general, DCS's form along the front of migrating low-pressure systems as with other severe weather events (Johns and Doswell, 1992). In North America, midlevel flow moving northwest usually covers over a quasi-stationary low altitude thermal boundary, linked to either a synoptic flow or cold outflow that are present before the beginning of convection, lead to the creation of a boundary or front (Coniglio et al., 2004; Johns and Hirt, 1987). Significant low-level warm advection near this boundary and high humid low levels and relatively dry mid-level air help create strong instability and initiate the convection characteristic of DCSs. Weak Progressive DCSs form on this boundary, moving at a shallow angle from the more relaxed side to the warmer side. Strong DCSs, both progressive and serial, tend to begin in the north and progress south along this boundary following the push of a classic cold front (Johns, 1993).

It should be noted that this formation structure is attributed to the warm season DCSs as the data set for these events is significantly larger than any other time of the year (Johns and Hirt 1987, Johns et al. 1990, Hilgendorf and Johnson 1998, Wakimoto 2001, Coniglio and Stensrud 2004). Evans and Doswell (2001) and Coniglio et al. (2004) showed that DCSs occur over a broad range of unstable low-level atmospheric shear conditions and patterns of large-scale flows beyond the unique environment of North America and that the strength of the mean flow has a significant influence on the duration and intensities of the wind gusts created. More recent studies support that the organization of derecho producing mesoscale convection systems have a complex dependency on the interaction of vertical winds shear of the mean flow and the size, intensity, and time scale of their destructive force (Coniglio et al. 2010, Lombardo Colle 2012, Campbell et al. 2017);. However, as this is the case, and a significant factor in the scale and extent of damage the outflow from a Derecho can have, this study will be limited to quiescent environments.

Downburst lines were brought into perspective from the analysis of environmental data from the JAWS and CLAWS projects analyzed by Hjelmfelt (1987, 1988). Twenty downburst line events were detailed, ranging in total outflow edge-to-edge length (outflow fringe to outflow fringe, Figure 1-17) of 5 to 30 *km* with an average outflow depth of 1.4 *km* measured in the edge of the maximum peak velocity (Figure 1). Each line was found to be comprised of 2 to 6 individual microburst events that originated from a cloud base between 2.6 to 4 *km* in altitude. Of these 20 downburst line examples observed, Hjelmfelt (1987) showed that downburst lines could have outflows that are nearly homogenous along their length or can be comprised of a series of discrete microburst events depending on the spatial and temporal separation of the constituent downburst events. The outflow of a homogeneous downburst line was found to have an average outflow of 19 *km* in length compared to the 14.5 *km* average of discrete downburst lines. The outflow perpendicular to the length or the "width" of both types of lines were the same. The average outflow length was found to be 17 *km*.
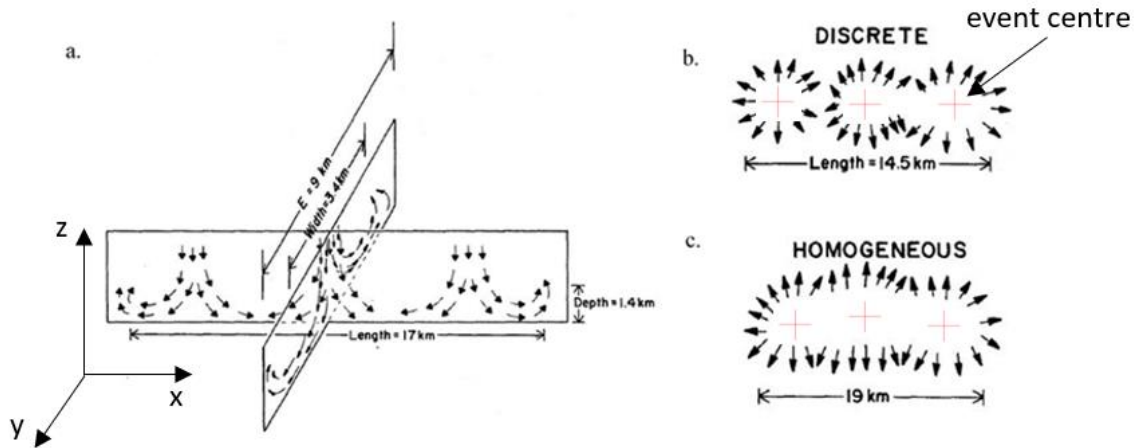
Figure 1-17 – a) Diagram of how a downburst line outflow was measured, b) horizontal outflow example of a discrete downburst line with the average length, c) horizontal outflow example of a homogeneous downburst line with average length (adapted from Hjelmfelt, 1987)

Hjelmfelt (1987) contributed the difference in the outflow lengths to the outflow fields' close interaction in the homogenous lines. This interaction leads to a sizeable accumulated swell in the line center, forcing the flow to diverge more along the line's length. This swell can be seen in the simulation renderings of semitransparent isosurfaces of potential temperature and velocity from Vermeire et al. (2011b) (Figure 2). The overall swells effect leads to higher speeds and a larger damage footprint (Vermeire et al., 2011b) and is the primary feature of a downburst line that distinguishes them from singular downburst events.
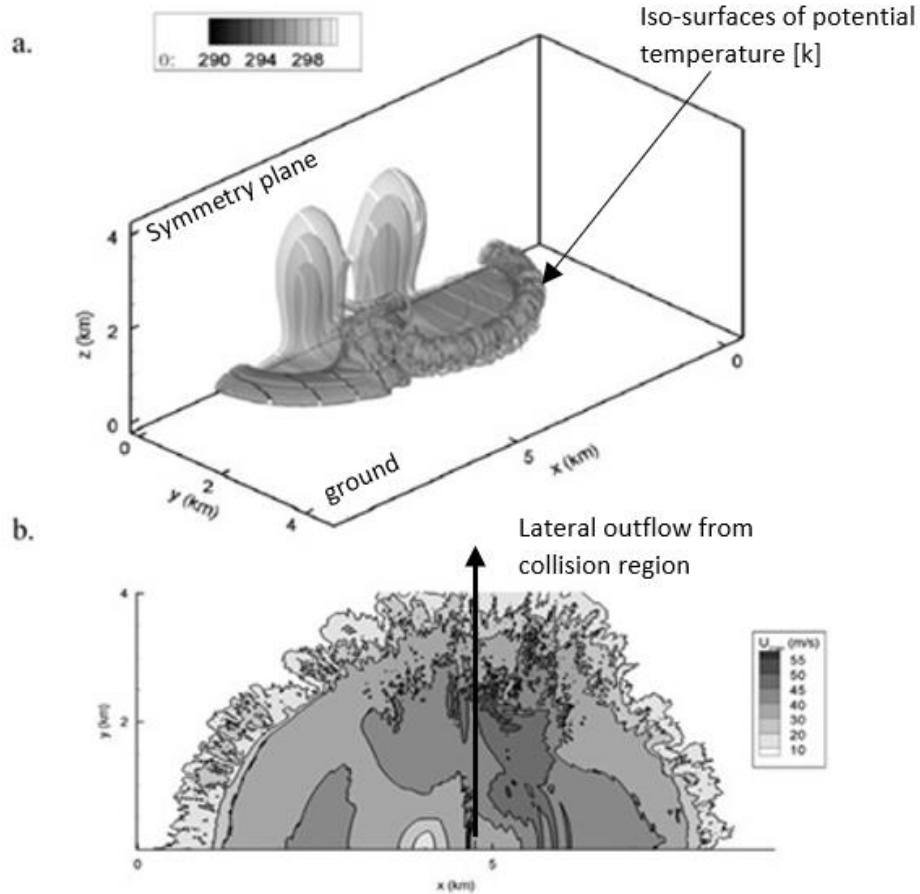
Figure 1-18 – a) semitransparent isosurfaces of potential temperature isosurfaces at 400 seconds for a complex interacting simulation with a time difference of zero, b) horizontal velocity contours through the height of the maximum radial velocity of a complex interacting case (adapted from Vermeire et al., 2011b)

The data presented by Hjelmfelt (1987) for downburst lines that resulted strictly from 2 downburst events were considered for developing comparable density-driven experiments. Table 2 summarizes the data used:

Table 1-1 - JAWS Downburst line data used for the design of two-fluid release experiments adapted from Hjelmfelt (1987)

Case	Length (km)	Width D/E (km)	Depth of outflow (km)	No. of Bursts (Max)	Cloud Type	Cloud base (km)
13 June 84	25	4/-	2.2	2	Line of Weak Cells	2.9
18 June 84	25	4/-	1.7	3	Single Strong Cell	-
20 June 84	20	2.5/15	1.0	2	Weak Small Cell	3.1
28 July 84	10	4/8	2.2	2	Single Cell	3.1
28 July 84	10	3/8	1.5	2	Line	2.8
30 July 84	14	4/15	0.5	2	Line	2.8
9 Aug 84	19	4/11	1.7	3	Line	3.1

Since Hjelmfelt's (1987) analysis and conclusions on the JAWS study, numerical simulations on downburst lines have been completed to understand further their evolution and subsequent impact with a focus on their near-surface flow fields. Cooling Source is driven (Anderson et al. 1992) Large Eddy Simulations (LES) based on the Bryan Cloud Model (CM1) (Bryan and Fritsch 2002) (detailed in section 2.3) of downburst lines designed from Hjelmfelt (1987) publication were performed by Orf et al. (1996) and later furthered by Vermeire et al. (2011b).

Orf et al. (1996) simulated line events with variation in the separation distance between the constituent events centres in combination with variation in the initial timing of each constituent event initiation to observe the effect that spatial and temporal differences between the interaction of individual microburst events have on the outflow structure of a downburst line. Vermeire et al. (2011b) further modelled and analyzed the near-surface wind fields of downburst lines in a quiescent environment to represent the set of low-shear conditions reported in the JAWS study.

Orf et al.'s (1996) numerical study explored the wind patterns that evolved as the result of the collision of 2 event-based downburst pairs as part of a downburst line separated (centre-to-centre) by 1,2,3,4 and 6 km in the simulation domain and temporally by 0, 2, and 3 min. This study showed that a downburst line forms into three distinct regimes: coalescing, complex interacting, and Soliton-like noninteracting. Coalescing downburst lines comprise single downburst events separated by less than 1 km (centre-to-centre), which form into a single more massive singular event. Spatial separation distances beyond 1 km, from 2 km and 3 km, caused a complex collision region, which increased the hazard region beyond 1 km from the event centres. The increase in hazard was attributed to the interactions between the wall jet-like outflow and roll-vortices of the constituent downburst events. Events separated by more than 3 km, in the 4 km range, the outflow of each event was shown to be developed into the typical roll-vortex structure of single downburst events (Fujita, 1985; Wilson and Wakimoto, 2001), leading to a Soliton-like collision region, similar to the discrete events defined by Hjelmfelt (1987).

Vermeire et al. (2011b) used the CS model (Anderson et al., 1992) utilized in LES parametric simulations based in CM1 (Bryan and Fritsch, 2002) to investigated the effect of spatial and temporal variation on the near-surface outflow of "two event-based" downburst lines along the lines of Orf et al. (1996), but with a focus on defining the level of hazard in the near-surface outflow region. Spatial separations of 1, 2, and 3 km were used in conjunction with temporal variations of 30, 60, 90, and 120 seconds in 12 simulations. Each simulation used an ellipsoidal Cooling Source function (Anderson et al., 1992) to produce two identical dense descending air mass 2 km above the simulation domain's bottom. The simulations' data were found to be consistent with field data from the JAWS thunderstorm downbursts and matched the coalescing and complex interacting subsets shown in Orf et al. (1996) with the characteristic highly divergent near-surface wind fields caused by the accumulated swell. The study found that the interaction of the constituent downburst outflows in a downburst line produces larger turbulence structures that are inconsistent with the structures observed in the vortex ring of a single downburst event (as noted by Orf et al., 1996) and are driven by the buoyancy induced vorticity generation which leads to unique outflow structures in the collision region (the swell). Two parameters were used to define the level of hazard present from the interaction in this

region (of the constituent events in a downburst line): the peak maximum wind speed and the surface area defined by the region of velocity from the Enhanced Fujita scale (McDonald and Mehta, 2006). Vermeire et al. (2011b) concluded that the interaction of events in the downburst line region of coalescing and complex interacting regimes were found to cause velocities with an amplification factor of 1.55 times that of the peak velocity of a single downburst event, and surface damage footprint sizes up to 70% larger than a single event (Vermeire et al., 2011b). In summary:

- Hjelmfelt's (1987) analysis of JAWS defined two downburst line types (homogenous and discrete) based on the separation distance between individual downburst events. Seven cases were identified (Table1) to establish the release height (average of 2.97 km) and for use for comparing outflow lengths (from 10 km to 25 km).

- Orf et al. (1996) indicated that the coalescing and complex interaction region formed during event outflow collisions from event centre to event centre separation distances between 1 km and 4 km leads to the highest hazard and is of interest to study.

- Vermeire et al. (2011b) simulations supported Orf et al. (1996) and established two parameters (Peak outflow velocity and damage footprint area) to define the hazard associated with the outflow of a downburst line event. Outflow velocities were found to be amplified by1.55 times that of the peak velocity of a single downburst event, and surface damage footprint sizes up to 70% larger than a single event.

Based on the work of Hjelmfelt (1988) and Vermeire et al. (2011), it is clear that the interaction of outflow between downburst events from squall lines and Derechos adds strength to the outflow. This added strength poses a more significant hazard over single downburst events. An increase in the transient loading from higher horizontal velocities can be expected and should be of high interest to structural and wind engineers. Although this is the case, no studies have been completed beyond Vermeire et al. (2011), and no experimental studies have been attempted to investigate the outflow of downburst lines.

1.3   Thesis Motivation

The hazard posed by downbursts and downbursts lines makes studying their outflow of particular interest to structural and wind Engineers. A downburst line producing storm stretching over Wisconsin, Illinois and Michigan USA and the province of Ontario, Canada of 16 July 1980 produced clusters of downbursts that caused over \$500 million in damages (Fujita, 1981). Near-surface wind speed was reported between FE0 up to FE2 and, in other cases, up to FE3 (Fujita, 1985). Wind speeds in this range of intensities have been responsible for significant infrastructure damage, particularly for power transmission line towers (Oliver et al., 2000, Holmes, 2001, Savory et al., 2001, Shehata et al., 2005).

The wind loads sustained from burst-swaths of downbursts have been indicated to be a significant contributing cause of power transmission line collapses (Shehata et al., 2005). Power transmission towers span tens of hundreds of kilometres with long stretches of cables between them, which increases their susceptibility to cascade type failures from exposure to burst-swaths from downbursts (Oliver et al., 2000; Whiteway, 2005). During the powerful derecho of September 1996, 19 power transmission towers in Manitoba were blown down, causing approximately \$10 million in damages (McCarthy and Melsness, 1996, Shehata et al., 2005). In totality, it has been estimated that near-surface high-velocity wind events, such as above, have caused over 80% of all-weather related transmission line tower damages (Savory et al., 2001).

As downbursts from out of complex microphysical and thermodynamic processes within the atmosphere, incorporating all the observed natural forcing parameters in simulated downbursts nearly impossible. The impinging jet model, as discussed, neglects many of these parameters and replaces them with momentum (Zhang et al., 2013) and does not reproduce the vortex ring based on buoyancy. The CS numerical model offers a computational means in capturing baroclinic vorticity generation. Combined with the use of CM1 (Bryan and Fritsch 2002), the CS approach can produce high temporal and spatial resolution 1:1 scaled outflows (Orf et al., 2012, Orf et al., 2014). However, these numerical methods are highly dependent on the initial forcing parameters and require further validation with experimental models and natural event observation. The dense fluid release model offers an experimental approach analogous to the CS numerical models. The dense

fluid release model simulates baroclinic vorticity generation based on the buoyancy gradient (Lundgren et al., 1992; Alahyari and Longmire, 1994; Alahyari, 1995; Babaei, 2018). This approach has also been extended into a computational model known as the Cooling Source (CS) numerical model (Anderson et al., 1992; Vermeire, 2011). With this in mind, the two-fluid model is employed in this study in an attempt to add experimental data for further comparison of numerical techniques, namely, the cooling source model used in the modelling of downburst lines (Vermeire, 2011).

1.4   Purpose

This thesis' primary purpose is to investigate the experimental application of the new two-fluid model release cylinder design for recreating scaled downburst and downburst line outflows. This study uses single stationary downburst release events and two-event downburst line releases, both in a quiescent environment, to determine how the near-surface outflow structure, vertical and horizontal wind profiles and vortical structures of the multiple release events differ from that of the single release events. This establishes how the flow regimes within the downburst line events present an elevated hazard over a single event.

1.5   Thesis Organization

The second chapter of this thesis reviews details of the experimental methods, equipment used, and analysis of the error level applied to this study. The third chapter presents the outflow velocity field of a single stationary event using the new release system. A direct comparison to past release experiments is made. The chapter discusses how the new wall features affected the outflow and concludes with an application of circumferential averaging on the outflow in the horizontal velocity vector fields. The fourth chapter uses the latest release system paired with a second identical release cylinder to investigate the effect on the outflow of a range of temporal and spatial separations between the two releases. The thesis is completed in the fifth chapter that summarizing the main conclusions and discoveries made.

1.6   References

Abd-Elaal, E.S., Mills, J.E., Ma, X., 2013. A coupled parametric-CFD study for determining ages of downbursts through investigation of different field parameters. J. Wind Eng. Ind. Aerodyn. 123, 30–42.

Alahyari, A., 1995. Dynamics of laboratory simulated microbursts. Ph.D. Dissertation, University of Minnesota.

Alahyari, A., Longmire, E.K., 1994. Particle image velocimetry in a variable density flow: application to a dynamically evolving downburst. Experiments in Fluids 17, 434-440.

Anderson, J.R., Orf, L. G., Straka, J.M., 1992. A 3-d model system for simulating thunderstorm microburst outflows. Meteorology and Atmospheric Physics, 49, 125-131.

Ashley W.S., Mote T.L., 2005. Derecho hazards in the United States. Bulletin of the American Meteorological Society 86, 11, 1577-1592.

Atkins N.T., 2010. How to distinguish between tornado and microburst (straight-line) wind damage. Lyndon State College Survey of Meteorology, MET 130 Course Notes, http://apollo.lsc.vsc.edu/classes/met130/notes/. Accessed Nov. 25, 2019.

Bakke, P., 1957. An experimental investigation of a wall jet. Journal of Fluid Mechanics 2, 5, 467-472.

Babaei, R., 2018. Experimental simulation of density-driven thunderstorm downbursts. MESc. Dissertation, The University of Western Ontario.

Bryan G.H., Fritsch J.M., 2002. A benchmark simulation for moist hydrostatic numerical models. Monthly Weather Review 130, 2917-2928.

Byers, H.R., Braham, R.R., 1948. Thunderstorm structure and circulation. J. Meteor. 5, 71-86.

Campbell, M.A. et al., 2017. Structure and Motion of Severe-Wind-Producing Mesoscale Convective Systems and Derechos in Relation to the Mean Wind. Weather and Forecasting, 32, 2, 423-439.

Chen, L., Letchford, C.W., 2004. A deterministic–stochastic hybrid model of downbursts and its impact on a cantilevered structure. Engineering Structures 26, 619-629.

Chowdhury, J., 2018. Transient Analysis of Full Scale and Experimental Downburst Flows. MESc. Dissertation, The University of Western Ontario.

Coniglio, M.C., Hwang, J.Y., Stensrud, D.J., 2010. Environmental Factors in the Upscale Growth and Longevity of MCSs Derived from Rapid Update Cycle Analyses. Monthly Weather Review, 138, 9, 3514-3539.

Coniglio, M.C., Stensrud, D.J., 2004. Interpreting the Climatology of Derechos. Weather and Forecasting, 19, 3, 595-605.

Coniglio, M.C., Stensrud, D.J., Richman, M.B., 2004. An Observational Study of Derecho-Producing Convective Systems. Weather and Forecasting 19, 2, 320-337.

Corfidi, S.F., Coniglio, M.C., Cohen, A.E., Mead, C.M., 2016. A Proposed Revision to the Definition of 'Derecho.' Bulletin of the American Meteorological Society 97, 6, 935-949.

Dodge, J., Arnold, J., Wilson, G., Evans, J., Fujita, T.T., 1986. The Cooperative Huntsville Meteorological Experiment (COHMEX). Bull. Amer. Meteor. Soc. 67, 417-419.

Doswell, C.A., 2001. Severe convective storms - An overview. Meteorological Monographs 28, 1-26.

Duranona, V., Sterling, M., and Baker, C. J., 2006. An analysis of extreme non-synoptic winds. J. Wind Eng. Indus. Aerodyn. 95, 1007-1027.

Fovell, R.G., Dailey, .P.S., 1995. The temporal behavior of numerically simulated multicell-type storms. Part I: Modes of behavior. J. Atmos. Sci. 52, 2073-2095.

Fujita, T.T., 1974. Jumbo Tornado Outbreak of 3 April 1974. Weatherwise 27, 116–126.

Fujita T.T., 1976. Spearhead echo and downburst near the approach end of a John F. Kennedy airport runway. New York City Department of Geophysical Sciences, University of Chicago, SMRP Research Report. Project Research Paper 137.

Fujita, T.T., Caracena, 1977.An Analysis of Three Weather-Related Aircraft Accidents. Bull. Amer. Meteor. Soc. 58, 11, 1164-1181.

Fujita T.T., 1978. Manual of downburst identification for project NIMROD. Satellite and Mesometeorology Research Paper No. 156, University of Chicago, Department of Geophysical Sciences, 104.

Fujita T.T., 1981. Five scales of airflow associated with a series of downbursts on 16 July 1980. Monthly Weather Review 109, 1438-1456.

Fujita T.T., Wakimoto R.M., 1981. Tornadoes and downbursts in the context of generalized planetary scales. Journal of the Atmospheric Sciences 38, 8, 1511-1534.

Fujita T.T., 1985. The downburst microburst and macroburst. The University of Chicago, Department of Geophysical Sciences 128.

Fujita, T.T., 1986. DFW downburst. The University of Chicago Press, Chicago, USA

Fujita, T., 1990. Downbursts: meteorological features and wind field characteristics. Journal of Wind Engineering and Industrial Aerodynamics, The Sixth U.S.National Conference on Wind Engineering 36, 75-86.

Geerts, B., 2001. Estimating downburst-related maximum surface wind speeds by means of proximity soundings in New South Wales, Australia. Weather Forecast. 16, 261-269.

Goff, R.G., 1976. Vertical structure of thunderstorm outflows.Mon.Weather Rev. 104, 1429-1440.

Hilgendorf, E.R., Johnson, R.H., 1998. A Study of the Evolution of Mesoscale Convective Systems Using WSR-88D Data," Weather and Forecasting 13, 2, 437-452.

Hinrichs, G., 1888: Tornadoes and derechos. Amer. Meteor. J., 5, 341-349.

Hjelmfelt, M. R., 1987. The Microbursts of 22 June 1982 in JAWS. J. Atmos. Sci., 44, 1646-1665.

Hjelmfelt M. R., 1988. Structure and life cycle of microburst outflows observed in Colorado. Journal of Applied Meteorology 27, 900-927.

Holmes, J.D., 2001. Wind loading of structures. Spon Press. 356.

Holmes, J.D., Oliver, SE., 2000. An empirical model of a downburst. Eng. Struct. 22, 9, 1167-1172.

Ivan, M., 1986. A ring-vortex downburst model for flight simulations. J. Aircraft 23, 232-236.

Jarvi, L., Punkka, A. J., Schultz, D. M., Petaja, T., Hohti, H., Rinne, J., et al., 2007. Micrometeorological observations of a microburst in southern Finland. Bound. Lay Meteorol. 125, 343-359.

Jesson, M., and Sterling, M. (2018). A simple vortex model of a thunderstorm downburst - a parametric evaluation. J. Wind Eng. Indus. Aerodyn. 174, 1-9.

Johns, R.H., 1993. Meteorological Conditions Associated with Bow Echo Development in Convective Storms. Weather and Forecasting, 8, 294-299.

Johns, R.H., Doswell, C.A., 1992. Severe Local Storms Forecasting. Weather and Forecasting, 7, 4, 588-612.

Johns, R. H., Hirt, W.D.,1987. Derechos: Widespread Convectively Induced Windstorms. Wea. Forecasting 2, 32-49.

Karner, H., Lugschitz, S., Tschannett, M., et al., 2012. Effects from downbursts on overhead lines Meteorological thunderstorm study—climatological, meteorological and CFD analysis. Elektrotech. Inftech.

Kim, J., Hangan, H., 2007. Numerical simulations of impinging jets with application to thunderstorm downbursts. Journal of Wind Engineering and Industrial Aerodynamics 95, 279-298.

Landreth, C. C., and Adrian, R. J., 1990. Impingement of a low Reynolds number turbulent circular jet onto a flat plate at normal incidence. Exp. Fluids. 9, 74-84.

Letchford, C. W., and Chay, M. T., 2002. Pressure distributions on a cube in a simulated thunderstorm downburst. Part B: moving downburst observations. J. Wind Eng. Indus. Aerodyn. 90, 733-753.

Lin, W. E., and Savory, E., 2006. Large-scale quasi-steady modelling of a downburst outflow using a slot jet. Wind Struct. 9, 419-440.

Lin, W. E., Orf, L. G., Savory, E., and Novacco, C., 2007. Proposed large-scale modelling of the transient features of a downburst outflow. Wind Struct. 10, 315-346.

Lin, W.E., Savory, E., 2010. Physical modelling of a downdraft outflow with a slot jet. Wind and Structures 13, 385-412.

Lombardo, K.A., Colle, B.A., 2012. Ambient Conditions Associated with the Maintenance and Decay of Quasi-Linear Convective Systems Crossing the Northeastern U.S. Coast. Monthly Weather Review, 140, 12, 3805-3819.

Lombardo, F. T., Smith, D. A., Schroeder, J. L., and Mehta, K. C., 2014.Thunderstorm Indus. Aerodyn. 125, 121-132.

Lundgren, T.S., Yao, J., Mansour, N.N., 1992. Microburst modelling and scaling. Journal of Fluids Mechanics 239, 461-488.

Maddox, M.A., 1980. Mesoscale Convective Complexes. Bul. of the Amer. Meteor. Soc. 61, 11, 1374-1387.

Mason, M., Letchford, C., James, D., 2005. Pulsed wall jet simulation of a stationary

thunderstorm downburst: Part a: physical structure and flow field characterization. Journal of Wind Engineering and Industrial Aerodynamics 93, 557-580.

Mason, M., Wood, G., Fletcher, D., 2009. Numerical simulation of downburst winds. Journal of Wind Engineering and Industrial Aerodynamics 97, 523-539.

Markowski, P., Richardson, Y.,2010. Mesoscale Meteorology in Midlatitudes. John Wiley and Sons Ltd., 407.

McCarthy, J., Wilson, J., Fujita, T.T., 1982. The joint airport weather studies project. Bulletin of the American Meteorological Society. 63, 15-22.

McCarthy, M. Melsness, 1996. Severe weather elements associated with September 5, 1996, hydro tower failures near Grosse Isle, Manitoba, Canada. Manitoba Environmental Service Centre, Environment Canada, 21.

McCarthy, J., Wilson, J., 1986. Classify, locate and avoid wind shear (CLAWS) project at Denver's international airport: operational testing of terminal weather hazard warnings with emphasis on microburst wind shear, American Institute of Aeronautics and Astronautics Monographs 32, 17-26.

McConville, A. C., Sterling, M., and Baker, C. J., 2009. The physical simulation of thunderstorm downbursts using an impinging jet.Wind Struct. 12, 133-149.

Metz, N. D., and L. F. Bosart, 2010: Derecho and MCS Development, Evolution, and Multiscale Interactions during 3–5 July 2003. Mon. Wea. Rev. 138, 3048-3070.

Oreskovic, C., 2016. Numerical Investigation Of Full-Scale Thunderstorm Downbursts: A Parametric Study And Comparison To Meteorological Model. MESc. Dissertation, The University of Western Ontario.

Orf, L.G., Anderson, J.R., Straka, J.M., 1996. A three-dimensional numerical analysis of colliding microburst outflow dynamics. Journal of the Atmospheric Sciences 53, 2490-2511.

Orf, L.G., Anderson, J.R., 1999. A numerical study of travelling microbursts. Monthly Weather Review 127, 1244-1258.

Orf, L. G., Kantor, E., Savory, E., 2012. Simulation of a downburst-producing thunderstorm using very high-resolution three-dimensional cloud model. J. Wind Eng. Ind. Aerodyn. 104-106, 547-557

Orf, L. G., Oreskovic, C., Kantor, E., Savory, E., 2014. Circumferential analysis of a

simulated three-dimensional downburst-producing thunderstorm outflow. J. Wind Eng. Ind. Aerodyn. 135, 182-190.

Proctor, F.H., 1988. Numerical simulations of an isolated microburst. Part I: dynamics and structure. J. Atmos. Sci. 45, 3137-3160.

Romanic, D., LoTufo, J., and Hangan, H., 2019. Transient behaviour in impinging jets in crossflow with application to downburst flows. J. Wind Eng. Indus. Aerodyn. 184, 209-227.

Romanic, D., Nicolini, E., Hangan, H., Burlando, M., Solari, G., 2020. A novel approach to scaling experimentally produced downburst-like impinging jet outflows. Journal of Wind Engineering and Industrial Aerodynamics 196, 104025.

Savory, E., Parke, G.A.R, Zeinoddini, M., Toy., N., Disney, P., 2001. Modelling of tornado and microburst-induced wind loading and failure of a lattice transmission tower. Eng. Struc. 23, 4, 365-375.

Shehata, A.Y., El Damatty, A.A., Savory, E., 2005. Finite element modeling of transmission line under downburst wind loading. Finite Elements in Analysis and Design. 42, 71-89.

Sengupta, A., Sarkar, P.P., 2008. Experimental measurement and numerical simulation of an impinging jet with application to thunderstorm microburst winds. Journal of Wind Engineering and Industrial Aerodynamics 96, 345-365.

Solari, G., De Gaetano, P., and Repetto, M. P. (2015). Thunderstorm response spectrum: fundamentals and case study. J. Wind Eng. Indus. Aerodyn. 143, 62-77.

Schultz, T.A., 1990. Multiple vortex ring model of the DFW microburst. Journal of Aircraft 27, 163-168.

Taszarek, M., and Coauthors, 2019: Derecho Evolving from a Mesocyclone - A Study of 11 August 2017 Severe Weather Outbreak in Poland: Event Analysis and High-Resolution Simulation. Mon. Wea. Rev. 147, 2283-2306.

Vermeire, B. C., Orf, L. G., Savory, E., 2011a. Improved modelling of downburst outflows For wind engineering applications using a cooling source approach. J Wind Eng. Ind. Aerodyn. 99, 801-814.

Vermeire, B. C., Orf, L. G., Savory, E., 2011b. A parametric study of downburst line near surface outflows. J. Wind Eng. Ind. Aerodyn. 99, 226-238.

Vermeire, B.C., 2010. Numerical Modeling of Thunderstorm Downbursts and Downburst Lines. MESc. Dissertation, The University of Western Ontario.

Wakimoto, R.M., 1985. Forecasting Dry Microburst Activity over the High Plains. Mon. Wea. Rev. 113, 1131-1143.

Wakimoto R.W., 2001. Severe convective storms, Chapter 7: Convectively driven high wind events. AMS Meteorological Monographs 28, 50 255-298.

Whiteway, K. (2005). Newfoundland power 2007 capital budget documentation: transmission line rebuild strategy. Retrieved 03/10, 2013, from http://www.pub.nf.ca/np2007cap/appdivided.htm. Accessed Dec. 20, 2019.

Wilson, J.W., Wakimoto, R.W., 2001. The Discovery of the Downburst: T. T. Fujita's Contribution, Bull. of the Amer. Meteor. Soc. 82, 1, 49-62.

Wilson J.W., Roberts R.D., Kessinger C., McCarthy J., 1984. Microburst wind structure and evaluation of Doppler radar for wind shear detection. Journal of Climate and Applied Meteorology 23, 898-915.

Wolfson, M. M., 1988. Characteristics of microbursts in the continental United States. Mass. Inst. Tech. Lincoln Lab. J. 1, 49-74.

Wood, G.S, Kwok, K. C.S., Motteram, N.A., Fletcher, D.F., 2001. Physical and numerical modelling of thunderstorm downbursts. Journal of Wind Engineering and Industrial Aerodynamics 89, 535-552.

Xu, Z., Hangan, H., 2008. Scale, boundary and inlet condition effects on impinging jets. Journal of Wind Engineering and Industrial Aerodynamics 96, 2383-2402.

Yao, J., Lundgren, T.S., 1996. Experimental investigations of microbursts. Experiments in Fluids. 21, 17-25.

Zhang, Y., Hu, H., Sarkar, P.P., 2013. Modelling of microburst outflows using impinging jet and cooling source approaches and their comparison. Eng. Struct. 56, 779-793.

Zipser, E.J., 1982. Use of a conceptual model of the life cycle of mesoscale convective systems to improve very short-range forecasts. Nowcasting, K. A. Browning, Ed., Academic Press, 191-204.

Chapter 2

2   Experimental Setup

This chapter provides a detailed review of the experimental facility, equipment used, and the experimental technique employed. The hydraulic flume, release system, and experiment design are discussed with relevant dimensions along with the limitations and sources of error. The selection of PIV seed particles and the procedure executed for the single and double downburst vertical and horizontal release experiments are described in detail. The chapter concludes with error analysis and final estimation of the uncertainty values applicable to all reported velocities in this study.

2.1   Experimental Facility

The experimental simulations of the downbursts using the two-fluid model were completed in a facility purposely created to investigate the effects of multiple downbursts with the ability to add translation and ambient flow (Roberto et al., 2014; Babaei, 2018). The facility (Figure 2-1) comprised of: a hydraulic flume with a glass test section, a computer running TSI INSIGHT 4G software, a New Wave Research Gemini PIV laser, a TSI Synchronizer, a TSI 8 Megapixel Charged Capture Device (CCD), and a novel dense fluid release system operated through a custom LabView based control system.

A – In-ground Ambient Fluid Tank

B – Pump

C – Inlet with Flow straightener

D – Tempered Glass Test Section

E – Weir Gate

F – Outlet and return duct
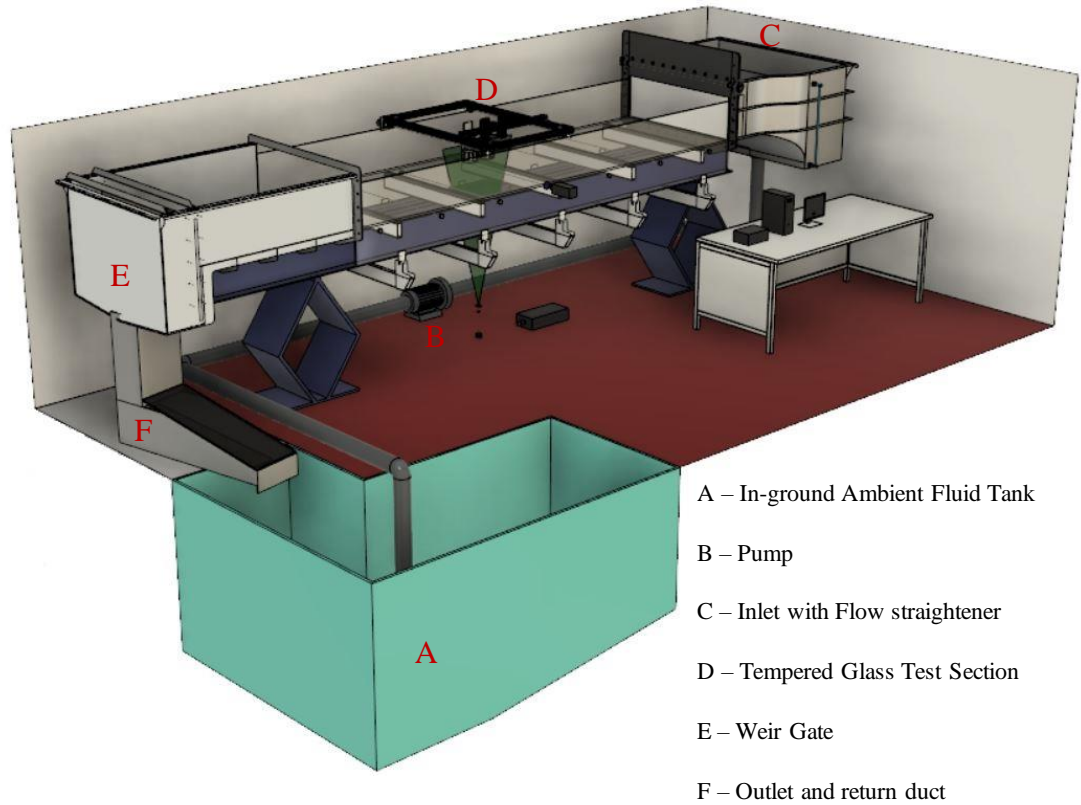
Figure 2-1 – Diagrammatic overview of the Flume Facility

The hydraulic flume was designed to contain an open water channel with a maximum depth of 30 cm. A 1.8 cm thick regular tempered glass test section, 1.06 m wide and 4.9 m long (Figure 2-2), occupied the effective length of the flume, where the effective length is the region that observation equipment can be used. A weir-gate at the outlet enabled the control of the fluid level within the test section. Figure 2-2 provides an overview of the entire system.
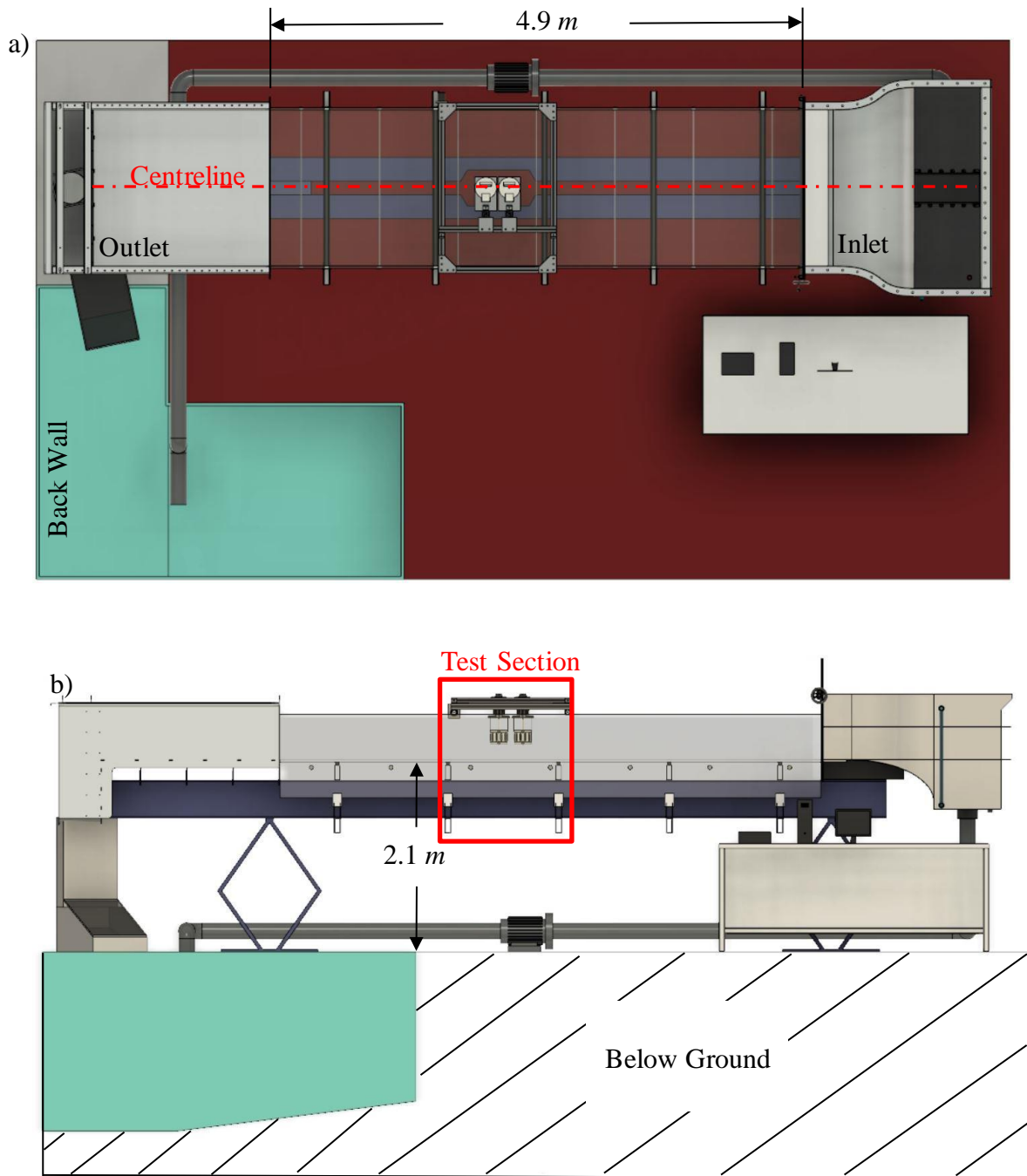
Figure 2-2- (a) Top view of the hydraulic flume, (b) front view of the hydraulic flume

An inground 3 m^3 reservoir (A in Figure 2-1) contained the ambient glycerol water solution. Three of the reservoir walls were made of reinforced concrete, and the back wall was made of marine grade corrugated steel piling sealed and bolted to the building foundation. Removable galvanized steel planking topped the reservoir. The planking, in combination with the inground location, was designed to reduce the amount of light pollution and

temperature fluctuations the glycerol solution was exposed too; this reduced algae growth and changes in the refractive index of the ambient fluid (Waxler et al., 1962; Bate et al., 1978; Kurtz et al., 1950).

A 3-phase 1.5 *hp* (1.125 *kW*) Armstrong vertical inline 4380 series pump (B in Figure 2-1) moved and mixed the glycerol solution through the flume. Standard 4 *in* (101 *mm*) diameter schedule 40 PVC piping carried the glycerol solution from the reservoir to the flume.

The release cylinders were positioned in the flume using a custom-built 40 *mm* square solid aluminum extrusion frame (Figure 2-3). The use of aluminum extrusions enabled flexibility and modularity. The structure could be extended or modified to accommodate a wide range of experimental equipment and cylinder configurations. The frame rode on 25 *mm* acetal wheels along the glass walls' top edge and was moved by a 12-volt 3-amp DC motor. The DC motor had a planetary gear reduction of 3.8:1 to move the assembly along through a range of 89 to 161 *rpm* to cover the flume freestream flow bulk velocity range from 3.08 *cm/s* to 7.49 *cm/s*. This speed range was selected to match translating downbursts to a scaled environmental flow range of 3.88-9.41 *m/s* as reported in JAWS (Hjelmfelt, 1987) and, more recently, in Burlando et al. (2017). Position feedback was provided by a linear encoder running through a Texas Instruments SCB-68 16-bit DAQ. The locational resolution was to the nearest 10 *μm*. Control was provided through a LabView VI (appendix) that operated the motor speed through pulse-width-modulation in a range of 55% duty cycle to 90% duty cycle. The system was designed to traverse the release cylinders at the flume's bulk flow speed to model downbursts as they travel with the parent storm as observed in environmental flows (Hjelmfelt, 1987; Orf and Anderson, 1998; Holmes and Oliver, 2000). Figure 2-3 lays out the frame configuration used for the multi-cylinder releases of this work:

Cylinder

Support Yoke

1.18 *m*

0.62 *m*
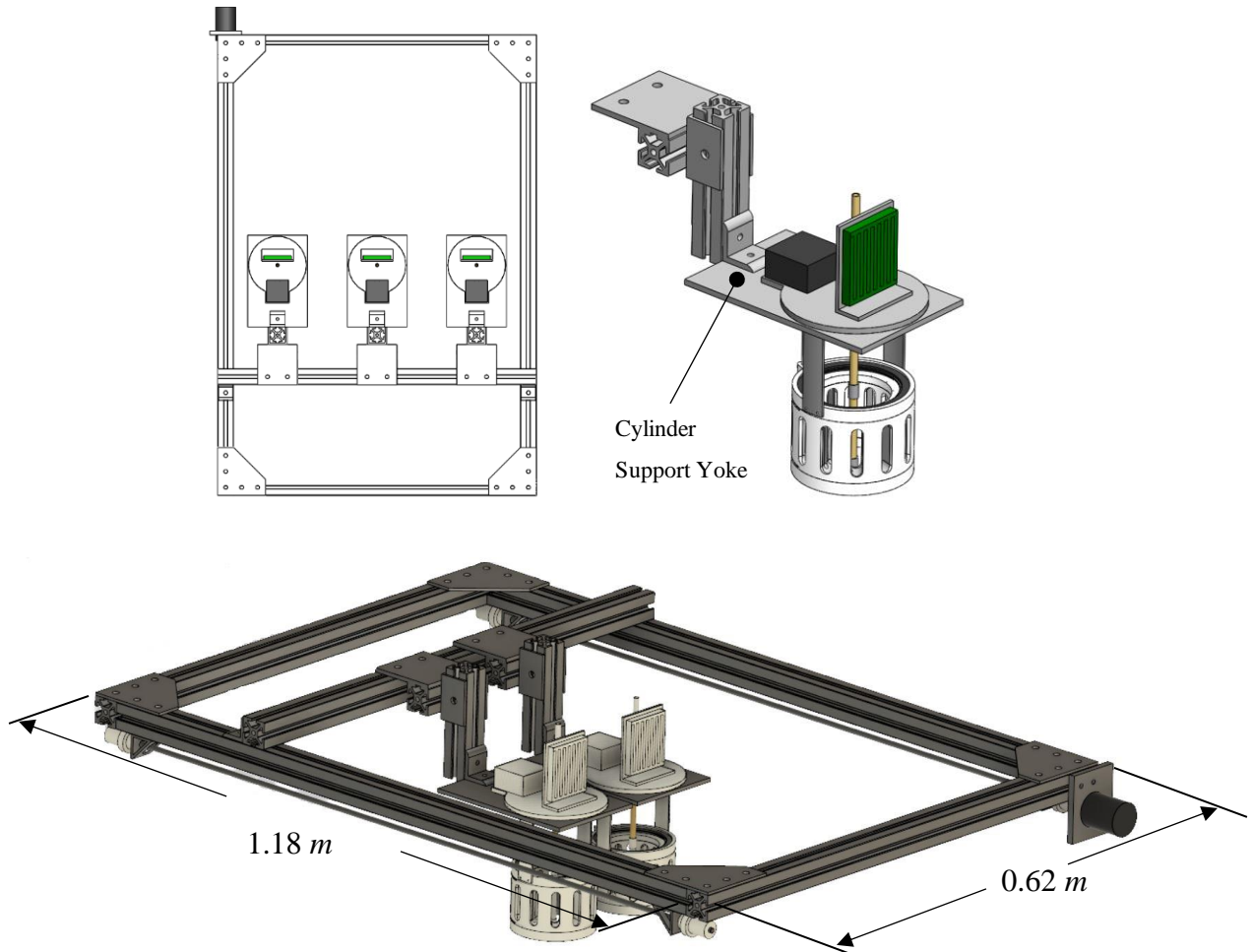
Figure 2-3- Flume traverse frame with release system shown. Three release systems are arranged for perspective on the range of positions possible for multiple releases, cylinder support yoke

The frame used had dimensions of 1.18 *m* wide and 0.62 *m* long, which gave a cylinder placement area of 0.73 *m²*. In terms of the cylinder outside diameter (Characteristic Diameter, D_C): $9D_c$ by $5D_c$. This allowed for a maximum separation distance of $3D_c$ or 225 *mm*. Appling the approximate flume scale to full scale meant that the maximum separation distance of 7 *km*. Following Hjelmfelt (1987), Orf and Anderson (1996) and Vermeire (2011), this allowed for the discrete range of downburst line events to be achieved at the laboratory scale.

2.2   Release Apparatus

A new release system was designed to model the outflow of a downburst better and enable multiple downbursts releases with spatial and temporal variations (Babaei, 2018). The method, Figure 2-4, comprises a release cylinder (A), stepper motor (B), motor controller (C), cylinder support mount (D), and a central rod that both fills the internal cylinder volume and seats the apertures (E).
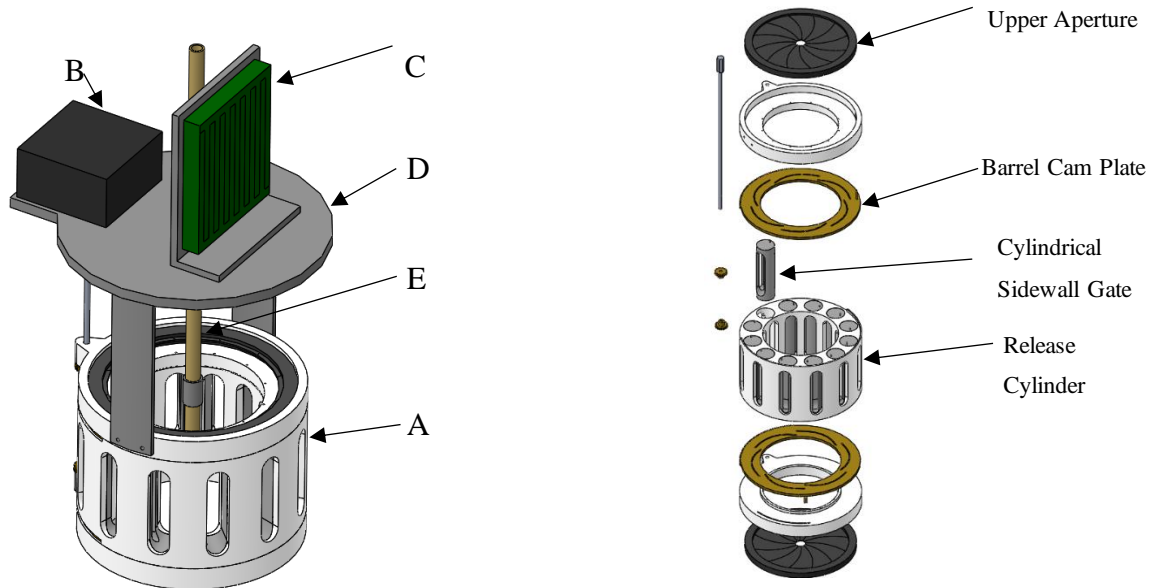
Figure 2-4- Release System is shown in the open configuration and an exploded view detailing the major features of the design (adapted from Babaei, 2018)

The release cylinder features a new design to overcome the influence of wall friction on the development of the vortex ring and reduce the effect of suction from the limited top cap porosity that existed in the cylinder design of Lundgren et al. (1992), Yao (1994), Alahyari and Longmire (1994), Alahyari (1995), and Yao and Lundgren (1996) (the difference is discussed in detail on chapter 4). All these studies used a closed walled aluminum cylinder with a porous top plate (Figure 2-6) and an elastomer membrane along the bottom to hold the dense dihydrogen phosphate solution in the cylinder. The fluid was released by a needle that priced the membrane when a release was to be performed.

The use of the elastomer membrane and solid cylinder leads to two direct interferences in the flow field of the downburst, which in turn affected the formation of the downburst

outflow. The solid cylinder walls introduced a noticeable wall effect and flow separation (Babaei, 2018). The drag and flow separation at the cylinder exit caused a recirculation to form annularly around the inside diameter at the cylinder exit. The drag resulted in the immediate formation of a vortex at the cylinder exit, meaning that the wall effect had more influence than baroclinic vorticity generation, which should have been forced by circulation forming because of the ambient-dense fluid shear interface. As the vortex ring is forced to develop rapidly near the cylinder, the outflow's leading edge is then stretched into an arrowhead shape (Alahyari, 1995). Additional stretching influence from the limited upper plate porosity would have added a suction force aiding in the vertical stretch of the downburst head (the effect is discussed in chapter 4).

The release of the dense fluid in the studies mentioned above was facilitated by an elastomer membrane that was pierced by a needle causing the membrane to separate. This separation is uncontrolled and could have caused flow disturbances near the cylinder exit. The early fill methods used by Lundgren et al. (1992) and Yao (1994) had the dense fluid added by means of injection after the release cylinder was submerged into the ambient solution. The dense fluid is needed to displace the ambient fluid within the cylinder in this approach. This meant that mixing and diffusion of the dense solution and ambient solution were possible. Wall porosity (here defined as the void wall area divided by the total wall area) was added to the cylinder design by the use of 12 rotating hollow gates assembled into the release systems walls shown in Figure 2-5 to reduce this wall effect. A completely openable top was also added.
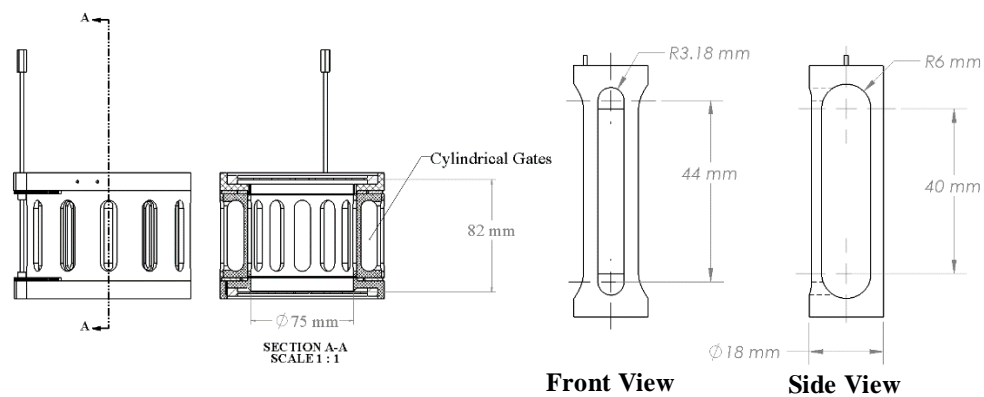
Figure 2-5- Release cylinder cross-section showing the location of cylindrical gates in the release cylinder wall, cylindrical gates (adapted from Babaei (2018))

These gates are driven by an upper and lower cam plate, Figure 2-4, which synchronized each gate opening so that all gates open simultaneously. A slot was incorporated into the gates' exterior face to enable ambient fluid to fill the internal void to prevent air bubbles from inducing mixing when opened. The system had a porosity of 28% (Babaei, 2018), corresponding to a wall area reduction of 1722 mm^2. The shape of the openings provided by the cylindrical sidewall gates was selected based on three criteria: maximizing the wall porosity, annularly uniform distribution of the porosity, maximizing the discharge coefficient to minimize momentum loss as the ambient fluid replaces the falling dense fluid.
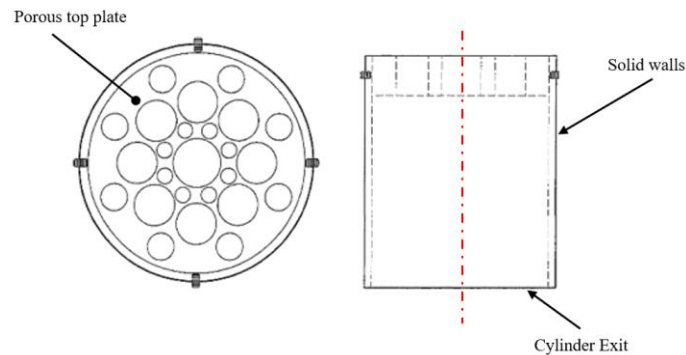
Figure 2-6- Porous top plate and side view (with hidden lines) of release cylinder used in Alahyari's release experiments (adapted from Alahyari 1995)

Holding the fluid before release necessitates some means of blocking the dense fluid and, therefore, will always lead to some method that disturbs the fluid interface during a release. Improvement in repeatability was achieved by replacing the membrane with aperture gates (Figure 2-4). Two aperture gates were used: one to replace the membrane puncture approach and cover the top of the cylinder to reduce suction after opening and prevent mixing and diffusion during cylinder placement. The aperture gates opened progressively via rotation of a cam plate that intern moves stainless steel leaves from covering the opening to resting inside the aperture's annular ring.

The opening of the aperture gates was synchronized with the opening of the cylindrical sidewall gates. Only 60 degrees of rotation was needed to open and close the apertures used in the current release system design. A hollow cylindrical pin (Figure 2-4) was added

through the release system's centre to seal to the aperture gates in their fully closed position. The hollow pin also served as the means to fill the release cylinder's internal volume prior to each release experiment.

The main cylinder body with its corresponding dimensions is shown in Figure 2-5 and correspond to those used in the studies by Lundgren et al. (1992) and Alahyari (1995). The total internal volume held 362 *mm* of the dense potassium dihydrogen phosphate water solution. The body was machined from Acetal, a change from the original selective laser sintering (SLS) 3D additive manufacturing using nylon in Babaei (2018). Machining from Acetal enabled control over the final interior surface finish and tolerances of the final assembled parts. A smooth finish was specified to reduce the wall effect, and higher tolerances helped minimize fluid leakage.

A stepper motor system (Oriental Motor CSK266-AT) provided torque required to open and close the aperture and cylindrical side wall gates (from completely closed to open in 0.5 *s*). A shaft with brass spur gears transferred the stepper motor's torque to the cam plates, which in-tern simultaneously opened/closed the cylindrical sidewall and upper and lower apertures gates.

A top SLS manufactured structure (D in Figure 2-5) assembles the release cylinder to the stepper motor and stepper motor driver. The structure served to hold and position the release system in the flume. A yoke plate (Figure 2-3) attached to an aluminum extrusion was used to vary the release height and secure the release system at the desired position in the flume.

Each release was performed by first closing the aperture and sidewall gates through the LabView control program (appendix). The dense fluid was filled through a funnel into the cylinder's interior volume via the fill pin. The release cylinder was lowered slowly into the ambient fluid of the flume during filling. This enabled the air inside the cylinder to escape through the top aperture gate and prevent the ambient solution from leaking into the cylinder before the dense solution occupied the entire interior volume. Each filling took over a minute on average. The control program would then be initiated to open the sidewall and aperture gates to release the dense fluid.

2.3   Scaling and Release Fluid Parameters

The scaled values for velocity (V_0), length (R_0), time (T_0), and Reynold's number (Re) are presented in **Error! Reference source not found.**. All values are computed according to Lundgren et al. (1992) scaling parameters, as discussed in chapter 2, section 2.5, using equations 2.4 to 2.7. The density properties are also presented in **Error! Reference source not found.**, along with the release height.

Table 2-1- Scaled Parameters for all release experiments

Parameter	*Value for All Releases*
$W_{ambient}$ *(mass %)*	7
W_{dense} *(mass %)*	7
Δρ/ρ$_{ambient}$ (%)	3.37
R_0 *(m)*	0.044
T_0 *(s)*	0.37
V_0 *(m/s)*	0.121
H (Release height, [*m*])	0.136
H/R$_0$	3.09
Re	4565

2.4   Particle Image Velocimetry (PIV) Experimental Setup

Particle Image Velocimetry (PIV) was utilized for the characterization of the vector field for single and downburst line events. TSI imaging equipment and software were used to capture the PIV images of both the single downburst event and downburst line events. The laser pulses were generated by a New Wave Research Gemini PIV double-pulse Nd: YAG laser system. The PIV particles' scattered light was collected by a Charged Coupled Device

(CCD) TSI 8-megapixel digital camera positioned at 90° to the imaging plane controlled by INSIGHT 4G software. The PIV technique uses captured image pairs, frame A and frame B, separated by a specified time interval, from the CCD camera to capture light reflected from particles suspended in a fluid's flow field (Adrian, 1991; Stamhuis, 2006). The time difference between the image pairs was 750 μs. The time difference was selected based on keeping the average seed particle displacement within 3 pixels between frame A and frame B at a flow speed of $V/V_0 = 3$, $V/V_0 = 0.5$ above the maximum flow speed expected. The image pairs were spatially calibrated and processed in PIVLab (Thielicke and Stamhuis, 2014) using a multi-pass Fast Fourie Transformation deformation widow algorithm, with a 50% overlap. The multi-pass FFT deformation window operated by finding the peaks of light intensity in a grid with a final interpolation region of 30 pixels x 30 pixels (2.85 *mm* x 2.85 *mm*) and 16 pixels x 16 pixels (1.52 *mm* x 1.52 *mm*). The algorithm positioned frame B over-frame A for the best matching of the peak intensity. The relative difference in the centre location of the grid space in frame B to the centre of frame A indicated the displacement and direction of the particles (Stamhuis, 2006). Paired with the time difference between frames A and B, the velocity of the particles was resolved. Erroneous vectors are removed by setting a velocity limit filter to exclude speeds over 1 m/s and out of the mean of 7 standard deviations.

Seed particle size was selected based on three criteria: time response of the particles suspended in water at the expected flow speed or the Stokes number, S_t (Eq. 2-1) (Dring, 1982), neutral buoyancy so that the particles remain suspended in the fluid, and their ability to reflect light for a high contrast above the ambient environment or a high signal-to-noise ratio (SNR) typically measured as the scattering cross-section. (Melling, 1997; Mangel and Morck, 1993; Adrian and Yao, 1985).

$$S_t = \frac{\rho U_c D_p^2}{18 \mu l_c} \tag{2-1}$$

The scattering cross-section was not calculated; instead, the different particles were tested for their ability to produce low SNR values between the primary and secondary peaks in the cross-correlation function under the release conditions.

The Stokes number, S_t (Equation 2-1, Dring, 1982) is the ratio of the time response of a particle to the characteristic time of the flow where ρ is the particle density, U_c the fluid velocity, D_p the particle diameter, μ the dynamic fluid viscosity, and l_c the characteristic length dimension. A Stokes number smaller than unity means that the fluid's time response is much higher than the particle and that the particles will follow the flow. A Stokes number greater than unity means that the particles' inertia will dominate its motion over moving with the fluid. **Error! Reference source not found.** contains the Stokes numbers computed for the selected particles.

Table 2-2– Seed particle properties used for selection in PIV experiments

Seed Particle	Density [g/cm^3]	Mean Diameter [µm]	Free Settling Velocity [m/s]	Stokes Number
Silicon Carbide	3.2	2	4.12E-06	2.04817E-10
Titanium Dioxide	3.5	3	1.05E-05	5.04042E-10
HGS	1.1	10	4.02E-06	1.76015E-09
PSP	1.03	50	1.81E-05	4.12035E-08

Silicon Carbide at a mean particle size of 3 *µm* was selected. Its Stokes number was much less than unity such that the inertia effects were limited so that the particles would be entrained in and move with the downburst dense fluid (Stamhuis, 2006; Adrian, 1991; Dring, 1982). The flume's ambient fluid was not seeded; however, dissolved mineral salts were present (from the lab water supply). A 5 *µm* sediment filter helped control the size of these particles. The combination was tested and found suitable for collecting quality PIV images. Control of seeding is necessary as particles' density per pixel is essential to produce the best quality PIV captures. However, eliminating particle contaminates in 3 *m³* of water glycerol solution proved impossible without a dedicated filtration system. The use of flocculants and refined particle filters in the water before adding glycerol may have effectively controlled particle density in the ambient fluid.

2.4.1   PIV Experiment Description

All the PIV releases completed are categorized into three sets of experiments: 1) Vertical release of a single stationary downburst in a quiescent environment, 2) Horizontal plane PIV capture of a single stationary downburst release in a quiescent environment, 3) Vertical plane PIV capture of two simultaneous downburst releases varied, both temporally and spatially, forming a downburst line:

1. The vertical plane PIV captures of a single stationary downburst release in a quiescent ambient flume environment were completed to continue the work presented by Babaei (2018). Eight releases were performed using the properties shown in **Error! Reference source not found.**, with only two releases containing a high-quality vector field for analysis: Single DB A and B. Each release was centred in the field of view to capture the release event symmetry. There were two primary purposes for these releases. The first was to use the velocity data computed from the PIV captures that were used to compare the outflow velocity field from the release event produced by the new system to past experiments based on the two-fluid model. The second was to use the vector data to show and map the horizontal roll vortex trajectory.

2. The horizontal plane PIV captures of a single stationary downburst release event in a quiescent flume environment were completed to understand the 3-D nature of the flow field produced by the new release system. The intention was to capture the radial outflow's horizontal plane at the height of the maximum radial velocity at $Z = 0.05R_0$. However, physical limitations made the lowest possible height $Z = 0.07R_0$ (the reasoning for this is detailed in section 3.4.2). Therefore, the horizontal releases were used for investigating the circumferential variation in the radial velocity along the radius from the downburst centre during the event. The best quality vector field of three releases was used for analysis.

3. Vertical plane PIV captures of two event-based stationary downburst lines release in a quiescent ambient flume environment were completed to create the first experimental data set. The vertical plane through the length of the outflow through the interaction region was performed to investigate how spatial and temporal

variation between events impacted the location of the maximum radial velocity. These same releases were also used for mapping the trajectory of the horizontal roll vortex structure. Two separation distances, $X = 3.69R_0$ and $X = 6.23R_0$ between event centres, both performed at three-time differences (**Error! Reference source not found.**). A total of 27 releases were performed with the best of each time difference and separation distance being used for data analysis. A set of captures in the vertical width of the interaction region was attempted. However, cross-plane motion limited the captures to only the close separation case with no time delay between events. Horizontal captures focusing on the width outflow of the interaction regions were performed at the height of the maximum to map the regions of high velocity.

2.4.2   Vertical and Horizontal Vector field Experiments Details

The vertical and horizontal vector fields for both a single and downburst line event release were performed through the test section's centreline in the flume shown in Figure 2-2 (a). A field of view of 3312 pixels in the x-direction by 1050 in the y-direction at an image pair capture frequency of 10 *Hz* was used for all PIV captures. This gave a spatial resolution of 94.27 *μm* per pixel ($0.002R_0$) for a field of view 312.22 *mm* by 98.98 *mm* (Figure 2-7) and a temporal resolution of 0.1 *sec*. Higher capture frequencies could be achieved with the CCD frame grabber combination used. However, the system's bit rate capacity limited the effective CCD sensor area to 3312 pixels by 1050 pixels at 10 Hz. Higher frequencies would have reduced the effective area of the CCD sensor and, in turn, the field of view. A frequency of 10 Hz was selected as a compromise between having an acceptable field of view and temporal resolution to capture the major flow field features.
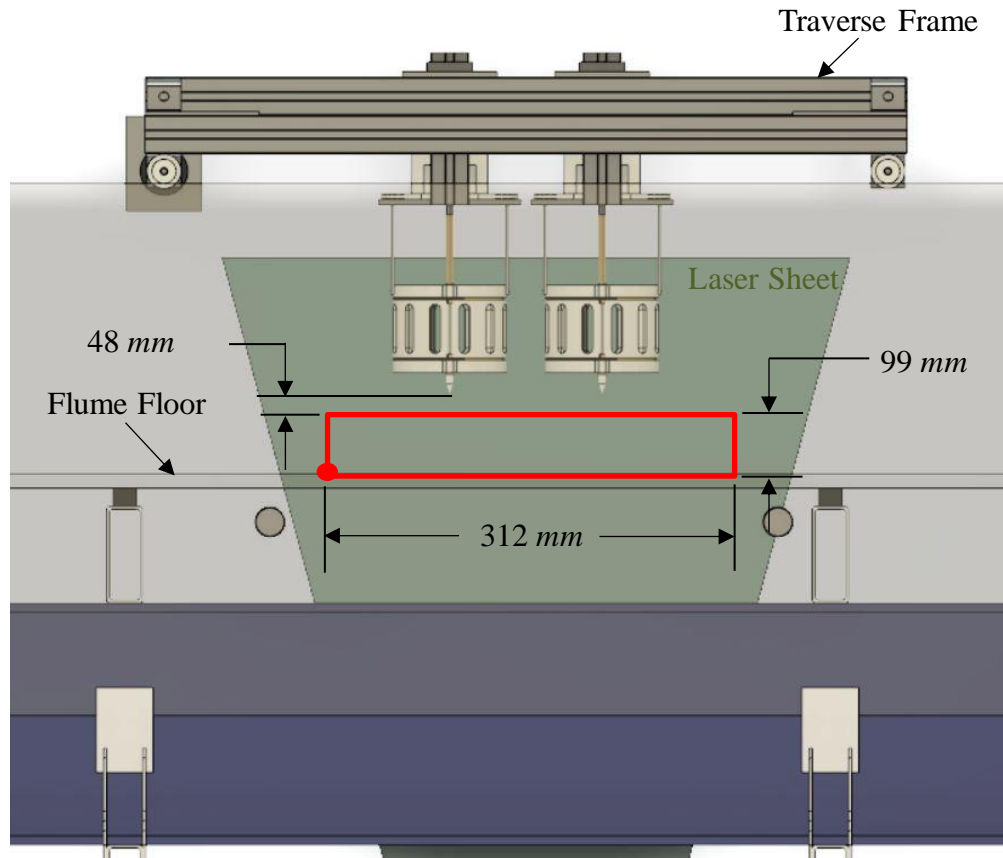
Figure 2-7 - Field of view for all vertical PIV captures, highlighted by the red square, 99 mm in Z (Z/R$_0$ = 2.25) x 312 mm in X (X/R$_0$ = 7.10) with the origin defined by the red dot

The laser sheet was the limiting factor in the selection of the field of view due to two constraints: the actual laser beam diameter and the available distance between the laser sheet producing lenses and the bottom glass of the flume test section. Only 2.1 *m* existed between the laser sheet lens assembly (Figure 2-7, b-a) and the flume test section's bottom glass. The lens assembly used a combination of -25 *mm* focal length cylindrical lens and a 1000 *mm* focal length spherical lens to produce a laser sheet with a diverging angle of 11°, a thickness of 2.69 *mm*, and a Raleigh length of 21.3 *m* calculated from Crimaldi (2008). This gave a laser sheet with a length of 360 *mm* through the test section. A smaller focal length lens (-3.9 *mm*) was considered to produce a laser sheet with a diverging angle of 73° to provide a laser sheet length of 760 *mm* through the test section. However, mirror damage to the laser's exiting dichromatic mirror led to a beam size of approximately 10 *mm* in

diameter, 5 *mm* more than the specified size. This made use of the -3.9 *mm* focal length cylindrical lens impossible without laser sheet contamination.
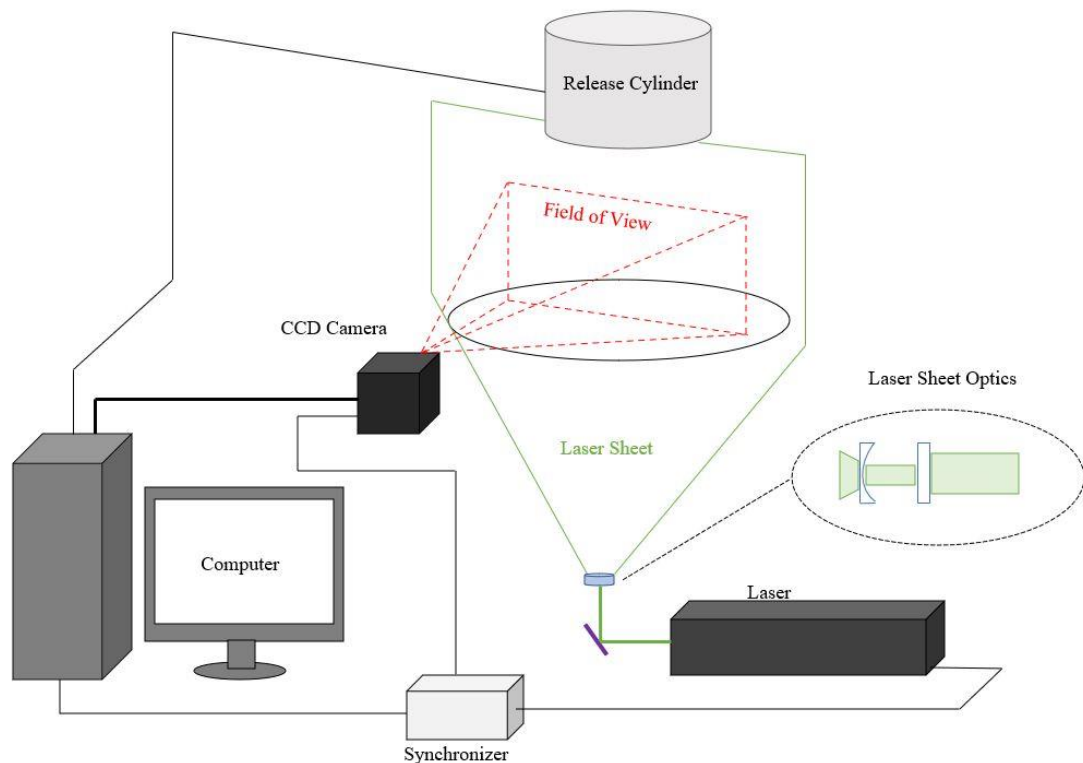
Figure 2-8– Vertical Release system overview for both single and multiple releases

Figure 2-8 is a schematic overview of the vertical plane experiment system setup for the double release configuration. The release cylinder was centred 15 mm above the top of the field of view (Figure 2-7). One hundred twenty image pairs of each release were captured and post-processed for all experiments.

The filed data from JAWS (Hjelmfelt 1987) and the numerical modelling work of Orf and Anderson (1996) and Vermeire (2011b) were used to decide the extent of the PIV measurement for the two-fluid release cylinder experiments for downburst lines. As discussed above, the maximum extent of the laser sheet, in combination with the geometric constraints of the cylinders' dimensions, limited the scope of possible scenarios that could be modelled relative to the range of downburst lines shown by JAWS and later redefined by Orf and Anderson (1996). With the focus on two event-based downburst lines, the

intent was to capture the full spectrum from homogeneous to discrete events as defined by Hjelmfelt (1987) and, in particular, to support the numerical modelling findings of Vermeire (2011 a, b). The experiments needed to have a scaled centre-to-centre spacing (X_d) $X_d/R_0 = 0.73$ (1 *km*) to $Xd/R0 = 2.18$ (3 *km*), and a temporal variation of 38 to 120 seconds. The minimum temporal variation of 0.235 s, scaled to 38 s, was the shortest time delay possible as this was the time required to open each cylinder fully. The aperture gates take 0.235 s to open fully, and the scaled time variations are shown in **Error! Reference source not found.**. ΔT_V represents the full-scale time used in Vermeire et al. (2011 b), T_{0v} the characteristic time scale of the CS simulations, and T_0 the characteristic time of this study.

Table 2-3- Scaled Temporal Variations

ΔT_V (Vermeire, 2011b) [s]	$\Delta T = T_0(\Delta T_V/T_{0v})$ [s]
30, closest 38	0.185 , closest 0.235
60	0.371
120	0.741

However, the experiments were physically limited in the possible range of centre to centre separation distances. Each release cylinder had an outside diameter of 120 *mm* or $2.71R_0$. This sizeable outer diameter was the consequence of adding the cylindrical gates to the release cylinder's sidewalls. Thicker sidewalls were needed to house the gates. The result was the minimum separation of 96.58 *mm* or $2.18R_0$. The support assembly and release system's clearance made the minimum possible separation distance $3.64R_0$ (160 *mm*). Discrete downburst lines with Soliton-like vortex interaction regions form with a constituent event separation of 4 *km* or more (Hjelmfelt, 1987; Orf and Anderson, 1996). The maximum separation was $6.23R_0$ and was chosen to be greater than 4 *km* (scaled) and

as a compromise between resolution and the field of view. The height above the flume floor was determined as $H/R_0 = 3.09$ to provide at least 20 *mm* of water above the top aperture gate. The average downburst cloud-based from JAWS was 3 *Km* (Hjelmfelt, 1987), which, based on the approximate lab to a full scale of 16000:1, provides an $H/R_0 = 4.29$. Babaei (2018) showed that the outflow of a release event was independent of release heights possible in the flume's available depth and that height larger than $H/R_0 = 2$ enabled enough room to capture the significant flow field characteristics.

The same spatial and temporal details were maintained in the horizontal plane experiments. The laser and camera were re-positioned to provide PIV fields near the maximum radial velocity in the horizontal plane to provide more information on the 3-D characteristics of the outflow vortex ring interaction region. Figure 2-9 provides a modelled overview of the horizontal plain system setup.
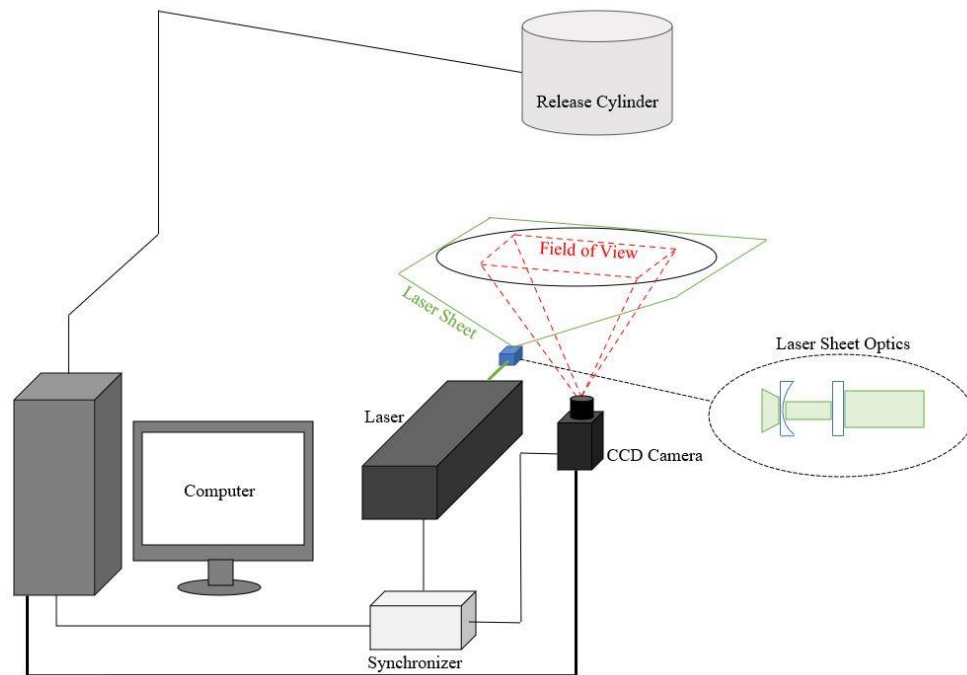
Figure 2-9 – Horizontal plane setup system overview, flume floor marked by the black ellipsoid

The laser sheet was placed 7 *mm* above the glass floor of the flume. Field studies observed the maximum radial wind speed of the downburst outflow occurs at approximately 50 *m*

(approx. $0.07R_0$) above the ground (Fujita and Wakimoto, 1981; Wilson et al., 1984; Hjelmfelt, 1988). Experiments using the two-fluid model employed in this study of Yao and Lundgren (1996) and Alahyari (1995) found that the maximum radial velocity occurred at $0.05R_0$ with a noted decrease in radial velocity above or below $0.05R_0$. This puts the horizontal field of view within the location of the maximum radial velocity. Alahyari (1995) concluded that the maximum radial velocity occurs just below the vortex core, approximately $Z/R_0 = 0.2$, from the reported velocity vector fields' interpretation. This placed the approximate height of the maximum at 8 *mm* above the flume floor for this study. A laser sheet height of 7 *mm* was close to the maximum radial velocity. The data collected at 7 *mm* would enable a circumferential analysis of the variation of velocity about the event at different radial positions over the event time series. Figure 2-10 shows the field of view that was available to capture the outflow's horizontal velocity fields.
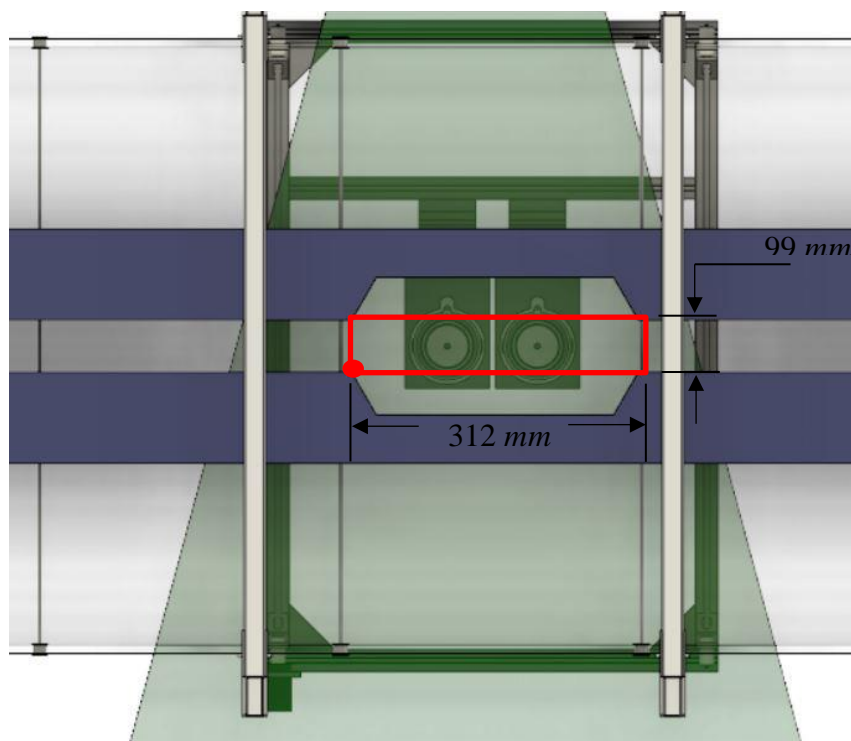
Figure 2-10 – Horizontal field of view looking upward from underneath the hydraulic flume, 99 mm in Z ($Z/R_0 = 2.25$) x 312 mm in X ($X/R_0 = 7.10$) with the origin defined by the red dot

The field of view maintained the pixel resolution of 3312 pixels in the x-direction by 1050 in the y-direction with the same image pair capture frequency of 10 *Hz*. This kept the spatial

resolution at 94.27 *μm* per pixel for a similar field of view 312.22 *mm* by 98.98 *mm*. The CCD was positioned to have the sides of the field of view within the flume support beams shown in blue in Figure 2-10.

2.5   Uncertainty

Two sources of uncertainty exist in the data presented in this study based on the system discussed in Sections 2.2 and 2.4: 1) the bias error or measured error as a result of the equipment, and 2) the random error based on the statistic variation in repeated measurements of the PIV vector fields (Raffel et al. 2007).

2.5.1   Uncertainty in The PIV Velocity Vector Fields

PIV techniques have progressed with improved capabilities into analyzing more complex flow regimes; though, no consensus of a widely accepted method for determining PIV uncertainty has emerged (Adrian, 2005, 2011; Raffel et al., 2007; Bhattacharya et al., 2018). Two methods have developed for quantifying PIV uncertainty: direct and indirect. Direct methods use measured quantities compared to the same quantities calculated from the PIV captures, analogous to calibration (Cower et al., 1997; Teminis et al., 2012; Thiekicke, 2014). Indirect methods estimate the uncertainty directly from the image plane, such as with the Image Matching method proposed by Sciacchitano et al. (2013) or the Correlation Statistics method by Wieneke (2015). Due to the age of the system and the uncertainty analysis discussed by Thielicke (2014), the direct method of uncertainty estimation was used in this study.

Direct PIV uncertainty methods consider multiple sources of error that contribute to the uncertainty in the measured displacements (Cower et al., 1997; Khadivi, 2012). These sources typically include the velocity gradient bias, the number of pixels occupied by the particle size, the amount of out-of-plane motion, peak locking, and interpolation error (Cower et al., 1997). The bias error is the primary source of uncertainty quantified (Adrian,

1988; Cower et al., 1997). The displacement measured in the PIV images is based on the correlation peak from the FFT deformation window method (Thieklicke, 2014), and because a gradient exists in the particle displacement, the second image sub-window does not contain all of the particles found in the first image sub-window. The result is a loss of the correlation in the plane of capture (Adrian 1988; Keane and Adrian 1991; Cower et al. 1997). The correlation peak is then biased to smaller displacements of the particles as they have a higher probability of remaining close to the region of the first sub-window such that they appear in the second image sub-window. Cower et al. (1997) called this "gradient Biasing" and is captured as the mean error in their figure 5(a to f) and Figure 2-11 (a) of Thielicke (2014). The random error is introduced from noise from system components in the location of the correlation peak was thought of as an RMS error presented in figure 5(a to f) in Cower et al. (1997) and 2-11 (b) in Thielicke (2014). It should be noted that the figures in both Cower et al. (1997) and Thieklicke (2014) are derived from turbulent flow in a channel.

The velocity gradient error was estimated based on Khadivi's (2012) analysis and Thielicke's (2014) review for the 16 by 16-pixel multi-pass interrogation regions. The particles in each image pair occupied 3 pixels on average and displaced a maximum of 3 pixels based on the highest flow cases. For the 16-by-16-pixel interrogation cases using the multi-pass method, the bias error was extrapolated from figure 2-11 (a) in Thielicke (2014) as 0.01 pixels and the RMS error from 2-11 (b) in Thielicke (2014) as 0.0375 pixels.

The out-of-plane and peak locking uncertainty were both deemed negatable. The Out-of-plane motion error was estimated based on the measured laser sheet thickness through the test section's region. The laser sheet was measured at 5mm thick due to the damaged mirror, as explained in Section 2.4.2. Based on the calibration of 9.5×10^{-5} *m/pixel*, this gave a laser sheet thickness equivalent to 56 pixels. The likely hood of capturing out-of-plan motion with such a thickness based on the average in-plane pixel displacement, which was around three across most of the captures, it was deemed small; therefore, the out-of-plane error due to the particles was negligible. The interpolation error was estimated to be 0.08 pixels for both cases based on Cower et al. (1997).

Using the root of the sum of the squares method (Wheeler and Gonji, 2009), the uncertainty for the measured velocity vector components u and v from the PIV system were tabulated. A summary of the uncertainty values is presented in **Error! Reference source not found.**. The bias error and random error were converted from pixels to *m/s* by using the calibration distance of 9.5×10^{-5} *m/pixel* and time between frames of 750×10^{-6} *s*.

Table 2-4 – The tabulated uncertainty values by the RSS method in m/s based on the estimated bias and random error in pixels

	Bias	Random	Unit
Gradient	0.005	0.038	Pixels
Interpolation	0.080		Pixels
RSS	0.080		Pixels
Uncertainty	0.010	0.005	m/s

From this analysis, it was concluded that the absolute uncertainty in the vector components u and v was ± 0.01 *m/s* ($\pm 0.09 V_0$) with a random error of ± 0.005 *m/s* ($\pm 0.04 V_0$).

2.6   References

Abbate, G., Bernini, U., Ragozzino, E., Somma, F., 1978. The temperature dependence of the refractive index of water. J. of Physics 11, 1167-1172.

Adrian, R.J., 1988. Statistical properties of particle image velocimetry measurements in turbulent flow. Laser Anemometry in Fluid Mech. 3, 115-129.

Adrian, R. J., 2005. Twenty years of particle image velocimetry. Exp. Fluids 39, 2, 159-169.

Adrian, R.J., Westerweel, J., 2011. Particle Image Velocimetry. Cambridge University Press. NY.

Adrian, R.J., 1991. Particle imaging techniques for experimental fluid mechanics. Ann. Rev. Fluid Mech. 23, 261- 304.

Adrian, R.J, Yao, C.S., 1985. Pulsed laser technique application to liquid and gaseous flows and the scattering power of seed materials. App. Opt. 24, 44-52.

Alahyari, A., Longmire, E.K., 1994. Particle image velocimetry in a variable density flow: application to a dynamically evolving downburst. Exp in Fluids 17, 434-440.

Alahyari, A., 1995. Dynamics of laboratory simulated microbursts. Ph.D. Dissertation, University of Minnesota USA.

Babaei, R., 2018. Experimental simulation of density-driven thunderstorm downbursts. MESc. Dissertation, The University of Western Ontario, Canada

Bhattacharya, S., Charonko, J.J., Vlachos, P.P, 2018. Particle image velocimetry (PIV) uncertainty quantification using moment of correlation (MC) plane. Meas. Sci. Technol., 29, 115301.

Burlando, M., Romanic, D., Solari, G., Hangan, H., Zhang, S., 2017. Field data analysis and weather scenario of a downburst event in Livorno, Italy, on 1 October 2012 Mon. Wea. Rev. 145, 3507-3527.

Cower, E., A., Monismith, S. G., 1997. A hybrid Digital Tracking Velocimetry Technique. Exp. Fluids 22, 199-211.

Crimaldi, J.P., 2008. Planar laser induced fluorescence in aqueous flows. Exp. Fluids 44, 851-863.

Dring, R.P., 1982. Sizing Criteria for Laser anemometry particles. ASME Fluids Eng., 104, 15-17.

Fujita T.T., Wakimoto R.M., 1981. Tornadoes and downbursts in the context of generalized planetary scales. J. Atmos. Sci. 38, 8, 1511-1534.

Hjelmfelt, M. R., 1987. The Microbursts of 22 June 1982 in JAWS. J. Atmos. Sci. 44, 1646-1665.

Hjelmfelt M. R., 1988. Structure and life cycle of microburst outflows observed in Colorado. J. of App. Meteo. 27, 900-927.

Holmes, J.D., Oliver, SE., 2000. An empirical model of a downburst. Eng. Struct. 22(9), 1167-1172.

Keane, R.D., Adrian, R.J., 1992. Theory of cross-correlation analysis of PIV images. App. Sci. Res. 49, 191-215.

Khadivi, T., 2012. Experimental and numerical study of flow structures associated with low aspect ratio elliptical cavities. Ph.D. Dissertation, The University of Western Ontario Canada.

Kurtz, S.S., Amon, S., Sankin, A., 1950. Effect of temperature on density and refractive index. Ind. & Eng. Chem. 42, 1, 174-176.

Lundgren, T.S., Yao, J., Mansour, N.N., 1992. Microburst modelling and scaling. J. of Fluid Mech. 239, 461-488.

Melling, A., 1997. Tracer particles and seeding for particle image velocimetry. Meas. Sci. Technol. 8, 1406-1416.

Mengel, F., Marck, T., 1993. Prediction of PIV recording performance. Proc. SPIE 2052, Fifth Int. Conf. Laser Anemometry: Advances and Applications, 6 August.

Orf, L.G., Anderson, J.R., Straka, J.M., 1996. A three-dimensional numerical analysis of colliding microburst outflow dynamics. J. of the Atmos. Sci. 53, 2490-2511.

Raffel, M., Christian, E., Wereley, S., Kompenhas, J., 2007. Particle Image Velocimetry: A Practical Guide. Springer, Berlin.

Roberto, M., Savory, E., Porto, J., 2014. Experimental and numerical simulation of density-driven thunderstorm downbursts. 25th Canadian Congress of Applied Mechanics,

London, Canada, 4 June.

Sciacchitano, A., Wieneke, B., Scarano, F., 2013. PIV uncertainty quantification by image matching. Meas. Sci. Technol. 24, 4, 045302.

Singh, S., Potopowicz, J.P., Van Uitert, L.G., Wemple, S.H., 1971. Nonlinear optical properties of hexagonal silicon carbide," Appl. Phys. Lett. 19, 53.

Stamhuis, E.J., 2006. Basics and principles of particle image velocimetry (PIV) for mapping biogenic and biologically relevant flows. Aquat. Ecol. 40, 463-479.

Thielicke, W., 2014. The Flapping Flight of Birds - Analysis and Application. PhD Dissertation, Rijksuniversiteit Groningen, Netherlands.

Timmins, B.H., Wilson, B.W., Smith, B.L. et al., 2012. A method for automatic estimation of instantaneous local uncertainty in particle image velocimetry measurements. Exp. Fluids 53, 1133-1147.

Vermeire, B.C., Orf, L.G., Savory, E., 2011a. Improved modelling of downburst outflows for wind engineering applications using a cooling source approach. J. Wind. Eng. Ind. Aerodyn. 99, 801-814.

Vermeire B.C., Orf, L.G., Savory, E. 2011b. A parametric study of downburst line near-surface outflows. J. Wind. Eng. Ind Aerodyn., 99, 226-238.

Waxler, R.M., and Weir, C.E., 1962. Effect of pressure and temperature on the refractive indices of benzene, carbon tetrachloride, and water. J of Res. of Nat. Bureau of Stand. Physi. and Chem., 67, 2, 163-171.

Wheeler, A., Ganji, A., 2009. Introduction to Engineering Experimentation, 3rd Edition, Prentice Hall Inc., NJ.

Wieneke, B., 2015. PIV uncertainty quantification from correlation statistics. Meas. Sci. Technol., 26, 7, 074002.

Wilson J.W., Roberts R.D., Kessinger C., McCarthy J., 1984. Microburst wind structure and evaluation of Doppler radar for wind shear detection. J. of Clim. and App. Meteo. 23, 898-915.

Yao, J., 1994. Experiments on microbursts. Ph.D. Dissertation, University of Minnesota USA.

Yao, J., Lundgren, T.S., 1996. Experimental investigations of microbursts. Experiments in Fluids. 21, 17-25.

Chapter 3

3   Velocity Vector Fields of Stationary Single Downburst Events in a Quiescent Ambient Environment

This chapter evaluates the PIV velocity vector fields for single stationary release experiments in a quiescent ambient environment using the new dense fluid release system in a vertical and horizontal orientation plane. The evaluation was initiated with an analysis of the release cylinders outflow symmetry about the event centreline by comparing the instantaneous maximum radial velocity's vertical and radial location. The evaluation continues with a preliminary observation of porosity's addition to the release cylinder sidewalls. Vortex core trajectory tracking in space and time, as a scaling method, by using the Lambda 2 (λ_2) criterion for vortex identification continued the evaluation. The chapter concludes by showing how the RMS velocity variation and average velocity about the circumference at the peak radial velocity location can be combined with a scaling factor to estimate the peak radial velocity.

3.1   Characterization of The Vertical Velocity Vector Fields

PIV-derived velocity vector fields taken in the vertical orientation plane were used to characterize the new system's outflow and establish a base-line event that could be used for evaluating downburst lines. An understanding of the outflow velocity structure over a series of similar releases was needed to quantify variance. Eight release events were performed at the same release height, density difference and field of view, as specified in section 2.4. Of the eight releases performed, only two were found suitable for analysis called here throughout as Single DB A and Single DB B. Laser sheet inconsistencies and issues with the laser system performance caused highly interpolated vector fields in the remaining six releases. These releases are excluded from the study, which imposes a limitation on the exact degree of repeatability and variance produced by the system based on the PIV velocity vector fields and must be considered when interoperating the data. Both variance and repeatability will be evaluated by looking at the events centreline's

symmetry between both available data sets. Babaei (2018) was able to show that the release system outflow was repeatable and symmetric over a series of 5 releases. The stationary PILF experiments detailed by Babaei (2018) were able to show symmetry in the release events in a quiescent ambient environment with the release system used in this study. A series of points symmetrically located on either side of the downburst release was used to plot the pixel intensity time series. Comparing the intensity variations between the pixels at the same locations, either side of the downburst between 3 separate release events lead to an average pixel intensity standard deviation of 260 over an intensity range of 0 - 4010 and a coefficient of variability of 0.19 (Babaei, 2018). Therefore, it was concluded that the time series of pixel intensities on the left side of the event centre show agreeance with those on the right side, which indicated symmetry

The highest near-ground velocities in the outflow of a downburst are found in an annular region typically around $X/R_0 = 1$, just after the initial impact (Fujita, 1985, Hjelmfelt, 1987), with a significant proportion of the velocity being horizontal. Both the velocity (V) and the horizontal velocity (u), referred to as the radial velocity, are used to evaluate the outflow symmetry and variation between release events. Figure 3-1 defines the convection used in this evaluation and provides a visual reference as to where the velocity profiles are located.
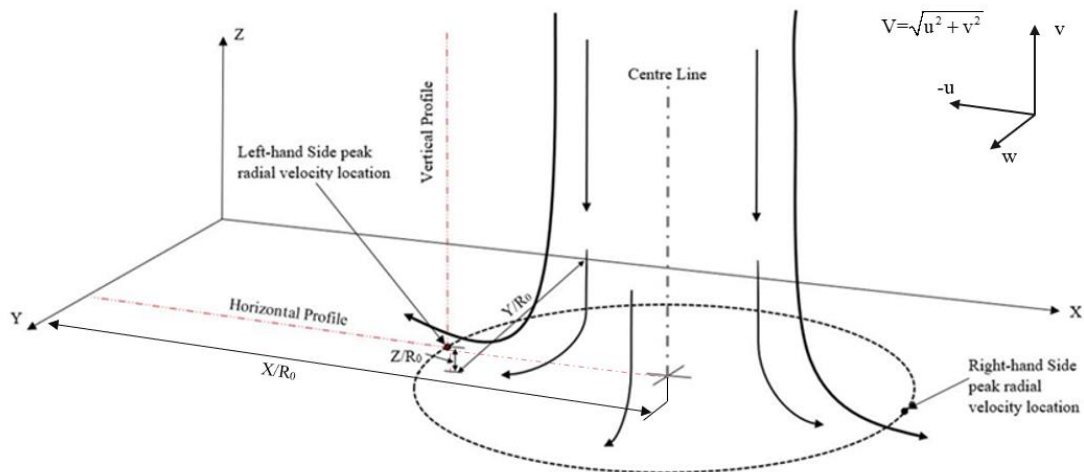
Figure 3-1 - Diagram of the locational variables used for the left-hand and right-hand side symmetry comparisons.

Release B (Single DB B) is the representative vertical release case for this study and used throughout this work as a visual reference and base release event for comparison. As discussed in section 2.4.2, the release cylinder is out of the plane of view. Figure 3-2 details the location of the release cylinder in relation to each of the shown vertical velocity vector fields.
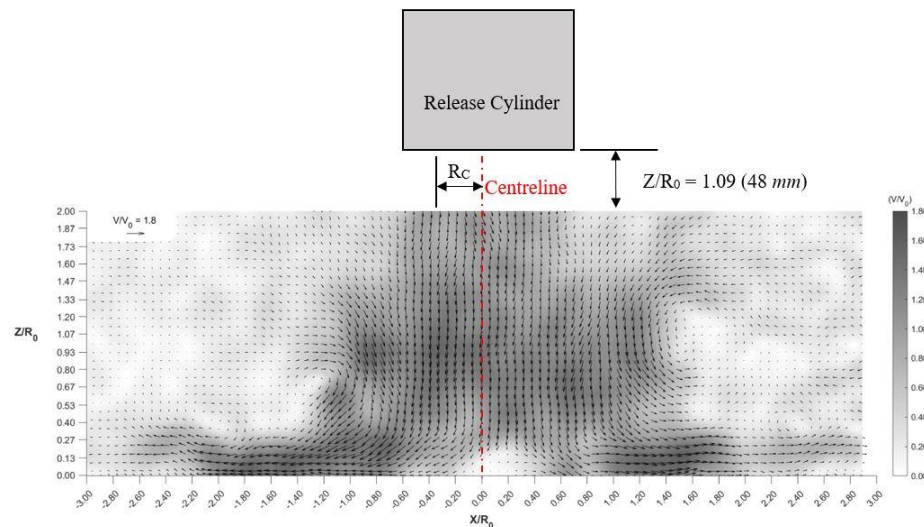
Figure 3-2 – Location of the release cylinder about the centreline (defined by $X/R_0 = 0$) for each vertical release, cylinder and dimensions not to scale.

Figure 3-3, through to Figure 3-6 (a), is the post-processed scaled velocity vector and contour fields of release A, and (b) of release B. The ensemble average was computed using release A and B starting at the initial release time $t/T_0 = 0$. The release conditions were as detailed in Section 2.4.2, with all releases being stationary and both in a quiescent ambient environment with a smooth wall as the ground plane. The time sequence of these images, scaled by $T_0 = 0.37s$ (Eq. 2.5) (based on the Lundgren et al. (1992) scaling parameters, section 1.2.2) are $t/T_0 = 2.70$, $t/T_0 = 4.60$, $t/T_0 = 5.14$, and $t/T_0 = 6.76$ for Single DB A and $t/T_0 = 3.51$, $t/T_0 = 5.16$, $t/T_0 = 5.95$, and $t/T_0 = 7.03$ for the ensemble average. The velocity vectors and contour fields are shown scaled by $V_0 = 0.11$ m/s. The ground plane is indicated as $Z/R_0 = 0$. The time series chosen for each represents the primary stages of downburst development, as Fujita (1985) detailed. The descending stage (Mid-air Microburst) is shown for both releases in Figure 3-3 (a) for Single DB A and (b) for Single DB B, the impingement stage (Touchdown) in Figure 3-4 (a) and (b), and the vortex

dissipation stage (Surface Microburst) in Figure 3-5 (a) and (b). The diagram of Figure 3-2 (a) shows the cylinder location relative to the vector maps presented in Figure 3-3 through to Figure 3-5. At $t/T_0 = 0$, the aperture gates are fully opened, and the dense fluid is free to descend by the action of gravity. As the dense fluid falls through the ambient fluid, baroclinic vorticity generation forces the leading edge to roll up into vortical structures. These structures are visible between $t/T_0 = 0.27$ to $t/T_0 = 3.24$ for Single DB A and $t/T_0 = 0.27$ to $t/T_0 = 2.97$ for Single DB B. The vortex ring entrains the ambient fluid with outer fringes of dense fluid.

This vorticity forces the centre fluid to be further accelerated downward, generating a leading head through the event centerline. This is better seen in Figure 3-21 at $t/T_0 = 3.51$ and $t/T_0 = 3.78$ using the lambda 2 (λ_2) criterion (section 3.3) for vortex core identification. The centre fluid leads the vortex ring by $Z/R_0 = 1.2$, measurable along each event's centreline. The definition of the vortex ring on the right side of the origin (in the positive X/R_0 direction, by convention) is diminished in both releases shown. A second vortex structure can be seen above the primary only on all release events' right-hand side. This secondary vortex eventually falls on top of the primary vortex in the outflow, which increased the outflow's depth and strength on the right-hand side.

The highest vertical velocities (v) occur before the leading edge impacts the ground at an approximate height $Z/R_0 = 0.85$ between Single DB A and B. Vertical velocities of approximately $v/V_0 = 1.6$ occurred between $t/T_0 = 6.26$ and $t/T_0 = 6.49$. Small radial velocities are observed along the ground plane just below the descending column and are induced by the ambient fluid being pushed away by the approaching dense fluid. The leading edge reaches the ground within 15-time steps from $t/T_0 = 0$ (at 10 Hz) and is shortly followed by the vortex ring. A few time steps after the initial impact, the highest near-ground velocities (V) are found at $t/T_0 = 4.87$, $X/R_0 = 0.87$ (DBA) and $t/T_0 = 4.60$, $X/R_0 = 0.65$ (DB B) ranging from $V/V_0 = 1.6$ to $V/V_0 = 1.9$ .At $t/T_0 = 5.94$, the vortex ring then begins to travel along the ground with the outflow, both being fed by the remaining sinking dense fluid. At approximately $t/T_0 = 6.76$, just after the vortex ring has started its propagation outward, the maximum radial velocity (u) is observed around $X/R_0 = 1.89$ to $X/R_0 = 1.93$.
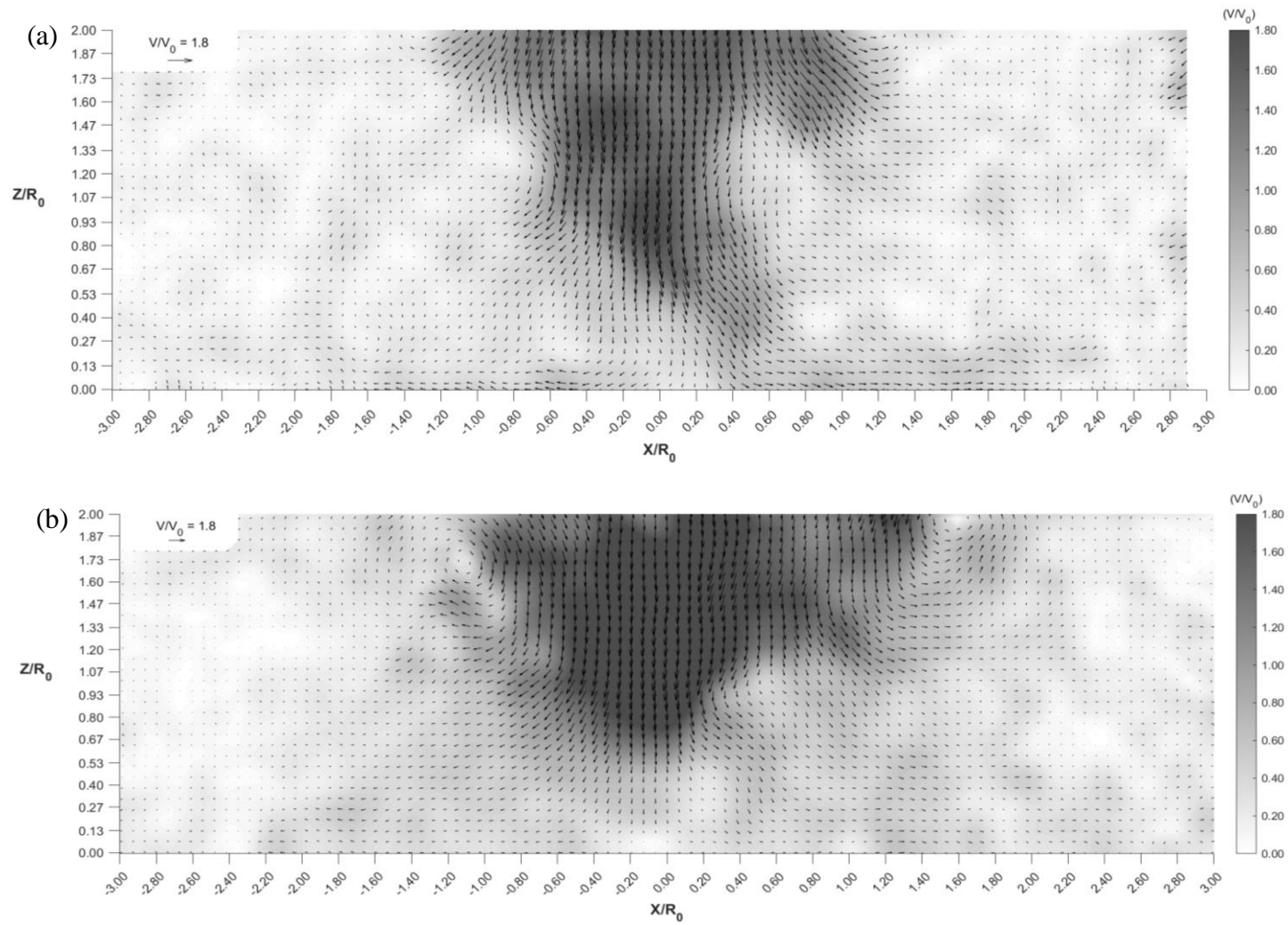
Figure 3-3 – (a) Scaled velocity vectors and contour fields (V/V₀) for Single DB A at t/T₀ = 2.70, (b) for Single DB B at t/T₀ = 3.51
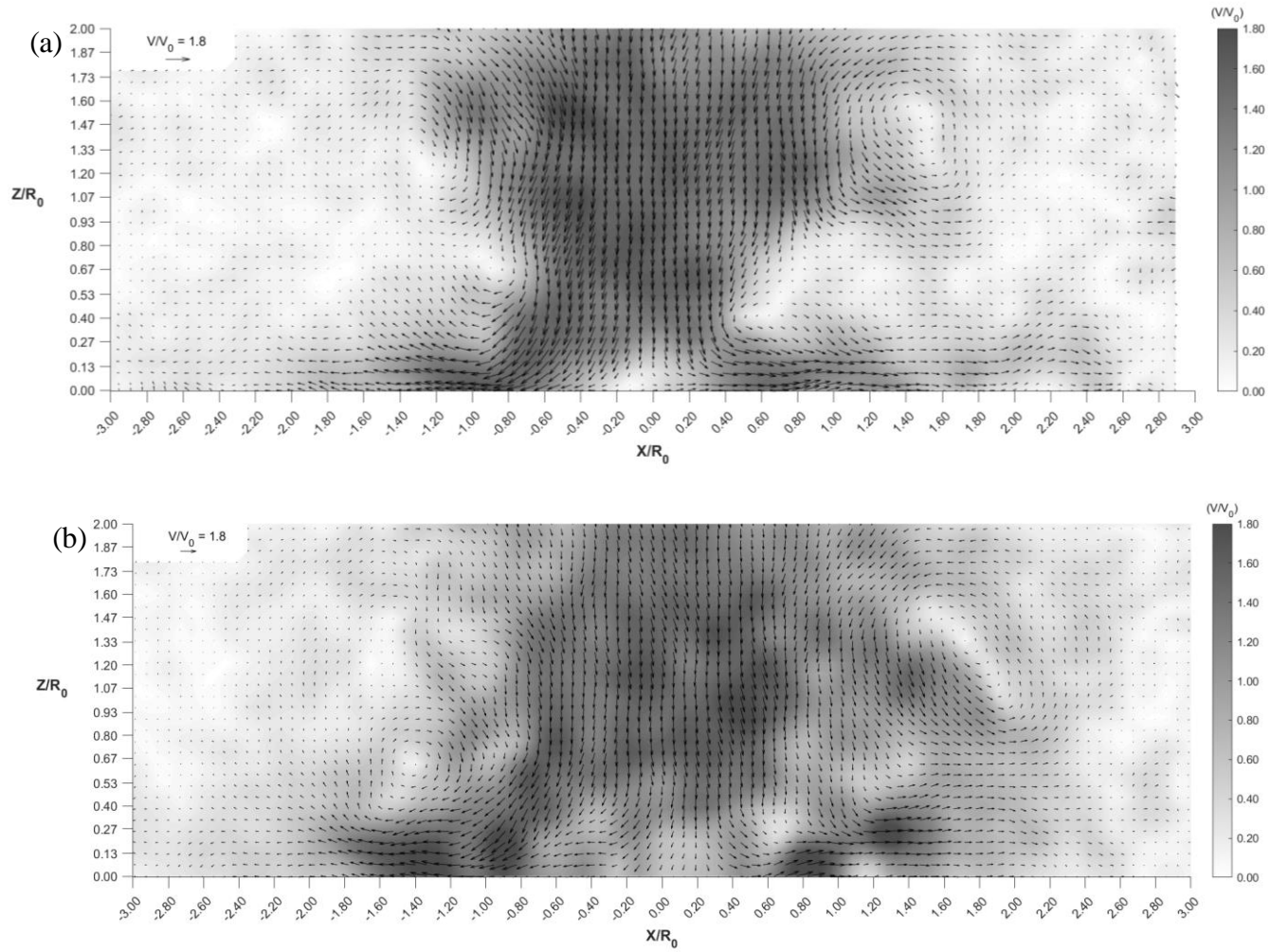
Figure 3-4 – (a) Scaled velocity vectors and contour fields (V/V₀) for Single DB A at t/T₀ = 4.60, (b) for Single DB B at t/T₀ = 5.16
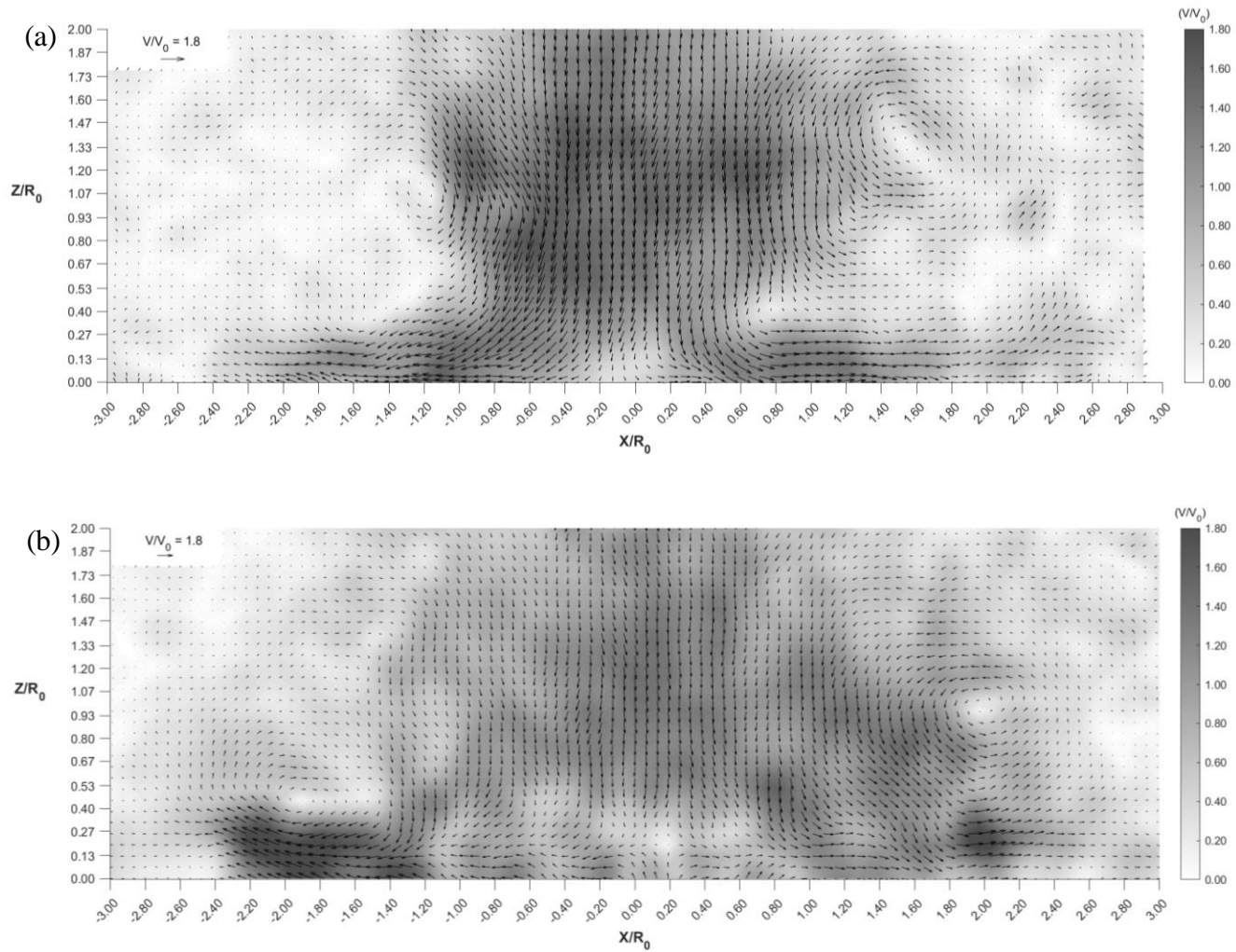
Figure 3-5 – (a) Scaled velocity vectors and contour fields (V/V₀) for Single DB A at t/T₀ = 5.14, (b) for Single DB B at t/T₀ = 5.95
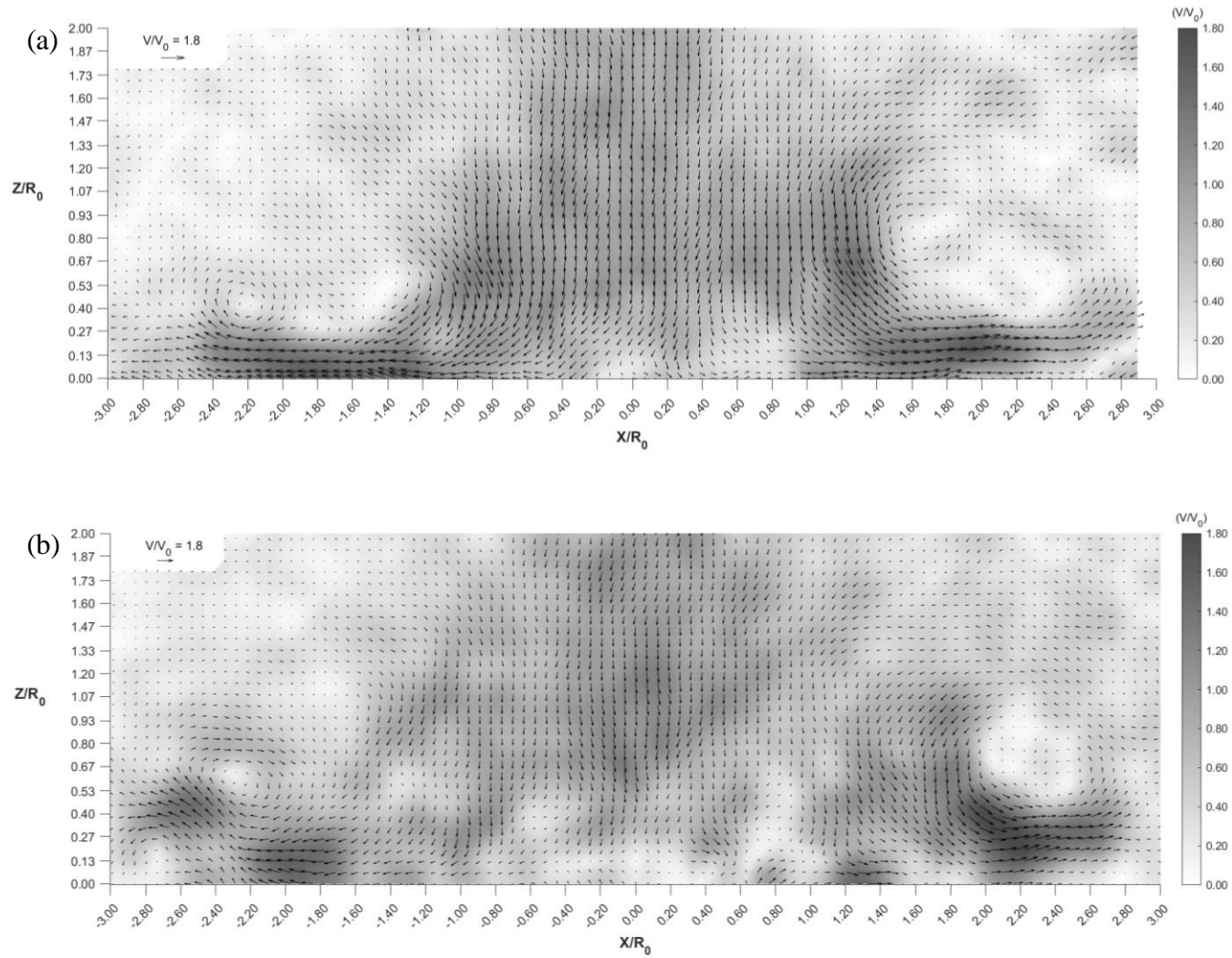
Figure 3-6 - (a) Scaled velocity vectors and contour fields (V/V₀) for Single DB A at t/T₀ = 6.76, (b) for Single DB B at t/T₀ = 7.03

Figure 3-3 to Figure 3-6 shows that the outflow about the centreline of all events shown is not entirely symmetrical. As discussed above, the right-hand side of both the single release A and B show a secondary falling vortical structure (Figure 3-5) that legs behind the initial vortical structure, starting at $t/T_0 = 4.6$ to $t/T_0 = 5.0$. This secondary structure falls on top of outflow in the right-hand side around $t/T_0 = 5.90$. As a result, the outflow on the right-hand side forms to have a higher outflow depth of $Z/R_0 = 0.40$ after $t/T_0 = 6.0$. This outflow behaviour is not observed in the experiments by Alahyari and Longmire (1994) or Yao and Lundgren (1996). The right-hand and left-hand time and location of the initial maximum radial velocity (u) are tabulated in Table 3-1. A simple percent difference (3.1) is used to quantify how similar the maximum radial velocity location is between the left and right-hand sides of the event centre.

$$\% \text{ Difference} = \left| \frac{A - B}{\left(\frac{A + B}{2}\right)} \right| 100 \qquad \textbf{3-1}$$

Table 3-1- summary of the maximum radial and horizontal velocity with reported values from past dense release experiments

	Symmetry Based on % Difference in the Vertical Velocity Vector Fields						DB A % Diff.	DB B % Diff.	DB B % Diff.
	Single DB A		Single DB B		Ensemble Ave.				
	LH	RH	LH	RH	LH	RH			
u_{max}/V_0	1.59	1.64	2.05	2.19	1.68	1.82	3.39	6.60	8.27
Z/R_0 loc	0.14	0.21	0.14	0.24	0.14	0.24	38.80	52.57	54.25
X/R_0 loc	1.88	1.85	1.90	1.90	1.61	1.66	1.83	0.00	3.09
t/T_0	6.76	6.76	5.94	5.94	5.41	5.41	0.00	0.00	0.00

Release Single DB A had lower maximum radial velocities by $u/V_0 = 0.5$ than release B, making it weaker overall. Both events' left-hand sides had reduced radial velocities due to the secondary falling vortex structure, adding outflow strength to the right-hand side. The

secondary vortex effect accounted for a 3% to 6% difference in radial velocity magnitude between the sides (about each event centre). The difference in magnitude was also reflected in the difference in the maximum radial velocity's vertical location. A 50% difference in the height above the ground plane in the maximum radial velocity location was recorded in release B and ensemble average. However, the radial region in which the maximum radial velocity was recorded between both events was consistent between the sides, with only release A having a 2% difference about the event centre.

Therefore, a consistent percentage difference in the height and magnitude in the maximum radial velocity between release A and B right hand and left-hand sides. Figure 3-7 illustrates the constant Z/R_0 difference in the location of the maximum radial velocity between the left-hand and right-hand sides of the release events from the new cylinder design. The vertical profiles of radial velocity for release B and the ensemble average are shown normalized by V_0 and R_0 at the maximum radial velocity location and time.
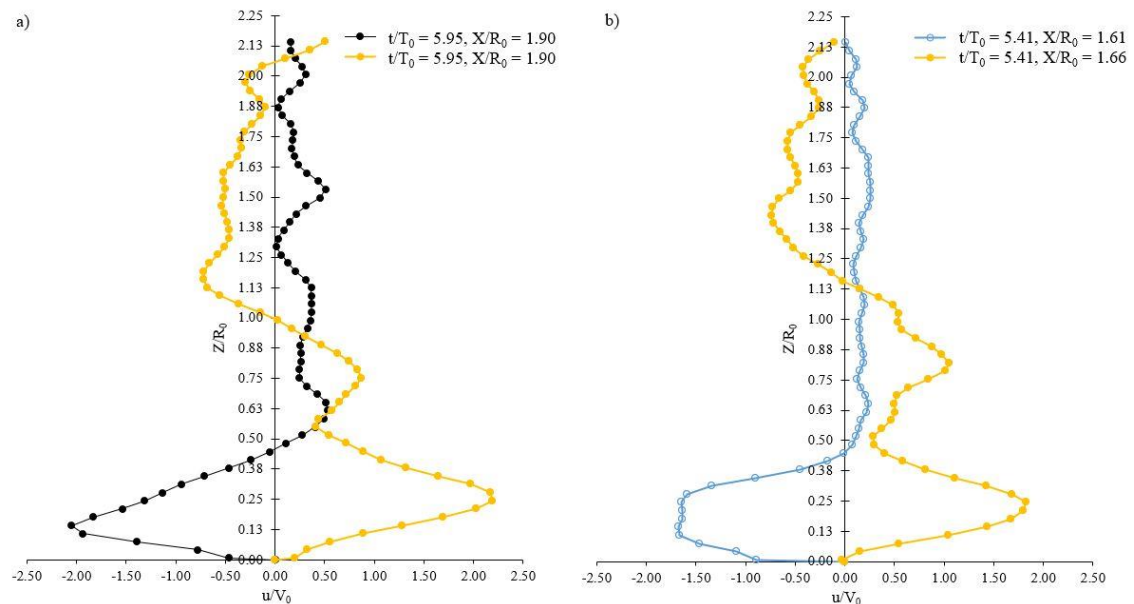
Figure 3-7 – Vertical radial (u) velocity profiles for (a) release B and (b) the ensemble average of release A and B at the time and radial location of the maximum radial velocity

In Figure 3-7 (a) and (b), the maximum left-hand radial velocity in release b and the ensemble average is 50% lower in vertical height above the ground plane than on the right-hand side. The velocity profile along the ground wall shows an expected smooth wall profile with the right-hand side of both (a) and (b) showing a higher, more pronounced height than the left-hand side. Each radial velocity profile above the maximum value quickly reduces to a fractional value fluctuating about zero, which indicates that the velocity above the outflow is predominately vertical. The reason for this is discussed further in the chapter (section 3.2).

Considering the radial velocity's horizontal profiles at the height if the maximum for both release B and the ensemble average for each side (left-hand and right-hand) results in Figure 3-8.
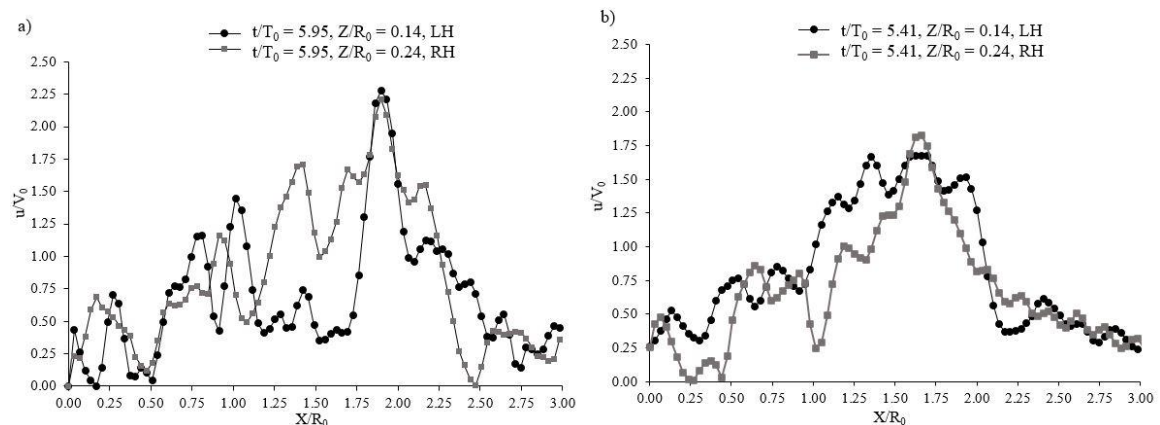
Figure 3-8 – Radial (X/R_0) horizontal profiles of normalized radial velocity (u/V_0) for the left-hand and right-hand sides about the event centreline for (a) single DB B and (b) the ensemble average of A and B

The radial location of the maximum radial velocity is nearly identical between the left-hand and right-hand sides of both release b and the ensemble average. In release B, the maximum radial velocity occurred at $X/R_0 = 1.9$ and when averaged with release A, around $X/R_0 = 1.6$. The profiles on either side of the maximum about the event centre are inconsistently variable. This inconsistency reflects the turbulence's highly transient nature

in the outflow of these release events and the fact that these profiles are of instantaneous velocity.

The difference in the height of the maximum radial velocity is apparent at the time of the maximum and throughout time about the maximum after impingement and during the outflow. Vertical profiles of the scaled time history (t/T_0) of the scaled radial velocity (u/V_0) for the left-hand and right-hand sides of release B are shown in Figure 3-9.
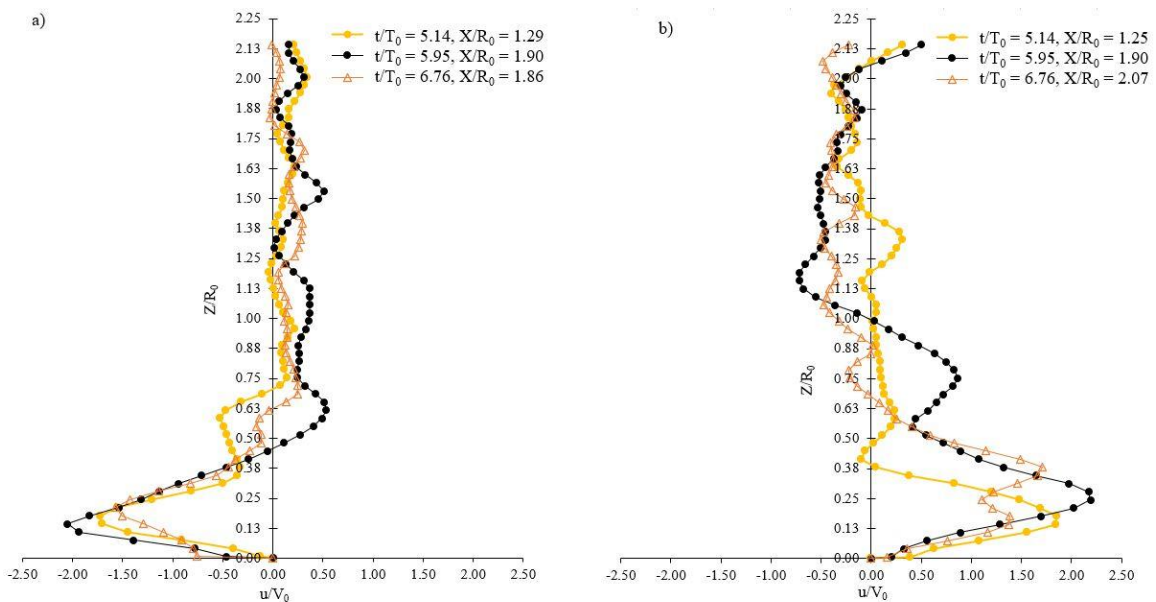
Figure 3-9 – Vertical scaled radial velocity (u/V_0) profiles at the radial location of the maximum for times before and after the maximum radial velocity for (a) the left-hand side of Single DB B and (b) the right-hand side of Single DB B

At $t/T_0 = 5.14$ and $t/T_0 = 5.95$ between the vertical profiles of u/V_0, the maximum height is approximately 50% lower on the left-hand side for release B. For times beyond the maximum radial velocity ($t/T_0 = 5.95$), the secondary vortex's effect in the right-hand outflow forces non-uniform profiles to form as the vortex introduces lift and counter vorticity along the leading edge.

This consistency in the difference of the maximum radial height location indicates that there is little variation between events and supports the findings of Babaei (2018). As the right-hand side of each release has a higher outflow velocity and height, it is possible to conclude that some aspects of the experimental setup influenced the outflow. Further investigation into the cause is needed to understand precisely why this happens.

Beyond the physical influences of the setup, there are a few other limitations that should be noted. In particular, how the spatial and temporal resolution impacts this analysis. The location of the maximum velocity (both velocity and its radial component) is based on the vector field as defined by the centre location of each interrogation region as decided by the window size (expressed in pixels). In this case, 16-pixel-by-16-pixel areas were used, which gave a spatial resolution of 9.5×10^{-5} m. It is possible to shift the maximum location by 1) changing the interrogation window size, 2) changing the location of the event centre $(X/R_0 = 0)$.

The outflow is turbulent, which means that the vortical structures have fine time scales. The PIV system could only be operated at 10 Hz to maintain the field of view. One-tenth of a second capture between frame sets could vary, possibly place the maximum velocity and maximum radial velocity outside the capture set presented here; the maximum could have been missed. Not to mention, as the flow is turbulent three-dimensional flow, the maximum velocity and radial velocity could have existed outside the capture plane.

From this first phase of this study, it is possible to conclude that the outflow velocity vector fields' variation between release events is negligible. Though there is an asymmetry in the outflow, the asymmetry is consistent. The left-hand side of all releases had a well-formed vortical structure in the outflow. In contrast, the right-hand side had developed a partial outflow with a secondary falling vortex that impacted the outflow development. As a result, the left-hand side outflow velocity vector fields are used for the remainder of this study.

Prior to comparing the release events to other simulated downbursts and full-scale field data, the added wall porosity's effect was evaluated.

3.1.1   Effect of The Wall Gates & Increased Wall Porosity

As described in section 2.2, cylindrical wall gates were added to the release cylinder to reduce the wall effect on the dense dropping fluid. The wall effect on dense fluid release experiments using a release cylinder was evaluated in URANS numerical simulations by Porto (2015). Two-dimensional axis-symmetric simulations were performed with and without a cylinder wall at a release height of $H/R_0 = 3.81$ and scaled parameters of $T_0 = 0.33$, $V_0 = 0.13$, and $R_0 = 0.043$. The cylinder dimensions used in the simulations are the same used in the physical cylinder of this study. Figure 3-10 details the model domain for evaluation of the effect of the wall.
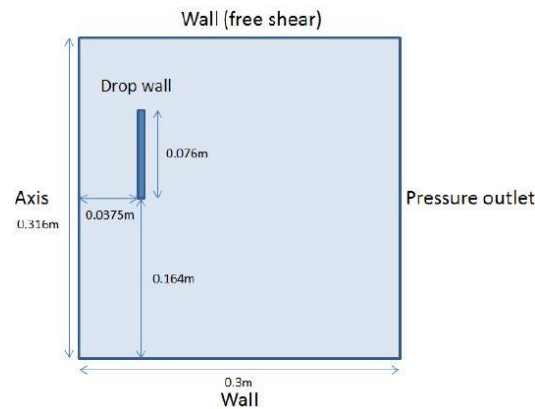
Figure 3-10 – URANS simulation domain for the 2-D axis-symmetric dense fluid release simulations based on a 4% density difference (adapted from Porto (2015))

The scaled time history (t/T_0) of the scaled maximum velocity (V/V_0) and scaled radial velocity (u/V_0) revealed that the wall does impact the outflow. Figure 3-11 (a) shows that the total velocity magnitude (V) in the domain from the initial release time at $t/T_0 = 0$ to the peak at $t/T_0 = 2$ is affected by the wall. The initial peak in total velocity represents the terminal velocity of the dense fluid before touching the ground. The peak signifies that the release height allows for the circulation in the release outflow to fully develop before reaching the ground (Yao and Lundgren, 1996; Alahyari, 1995). The wall induced drag on simulated dense fluid during the vertical descent removing potential energy from the flow. Without the wall, higher terminal velocity is present (Figure 3-11 (a)). Without the wall

drag, the peak total velocity occurs sooner, along with the associated radial velocity (Figure 3-10 (b)).
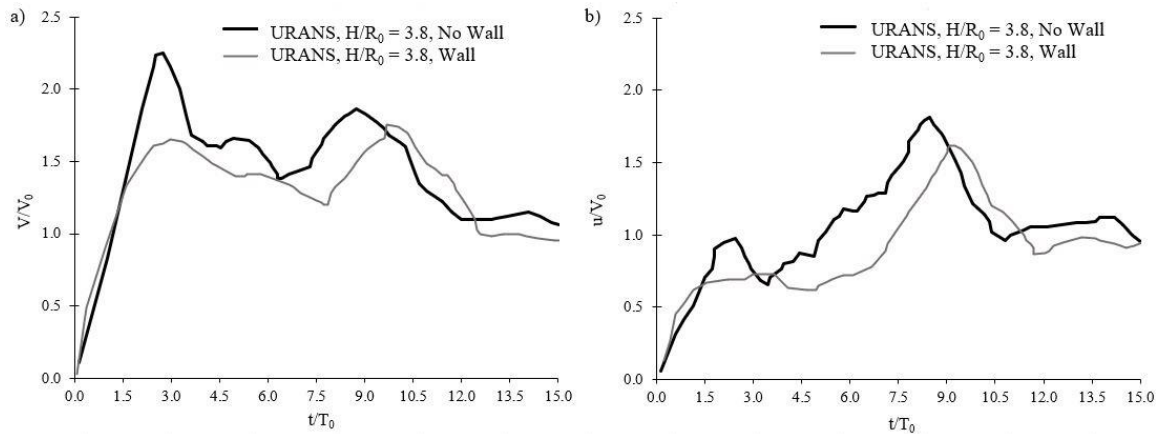
Figure 3-11 – (a) total domain maximum velocity scaled by V_0 for URANS dense release simulations with and without a wall, (b) the total domain maximum radial velocity for the same URANS simulations as in (a) (adapted from Porto (2015))

Upon impacting ground impact, the second peak (the maximum near-surface velocity) is staggered between the simulation with and without the wall. The same result can also be observed in Figure 3-11 (b), in the maximum radial velocity. The maximum radial velocity is reduced $u/V_0 = 0.5$ and occurs $t/T_0 = 2.05$ after the simulation's maximum without the wall. The wall reduced the maximum overall and radial velocity, which implies that added wall porosity may reduce the wall's influence and lead to higher near-ground velocities.

There are, however, two limitations that need to be considered from the data of URANS simulations. First, the simulations were completed at the height of $H/R_0 = 3.81$ (164 *mm*), $Z/R_0 = 0.72$ higher than the height used in this experiment. Second, the simulations were two-dimensional and axis-symmetric, where the experimental release is a complex turbulent three-dimensional flow with a consistent know asymmetry. Figure 3-12 (a) and (b) are URANS simulations also performed by Porto (2015) that capture the time history on the effect that release height has on the total domain velocity and the maximum domain radial velocity.
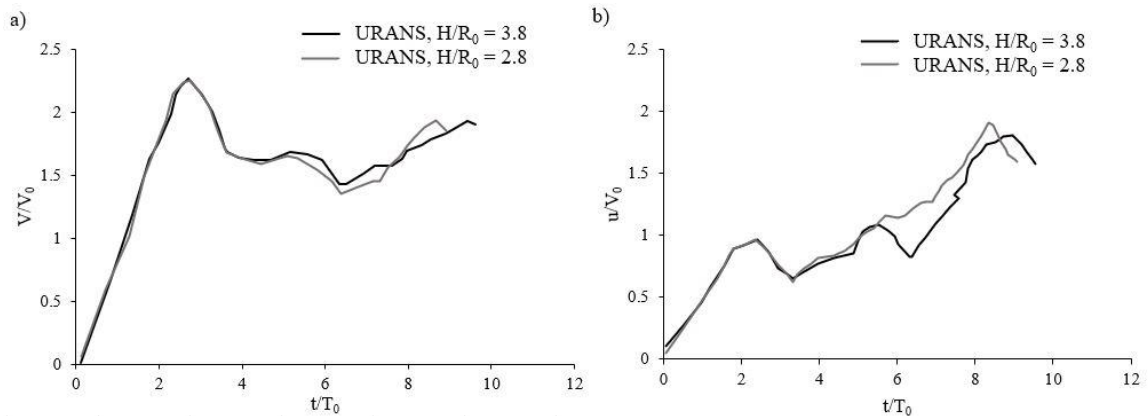
Figure 3-12 - (a) total domain maximum velocity scaled by V_0 for URANS dense release simulations with and without a wall, (b) the total domain maximum radial velocity for the same URANS simulations as in (a) (adapted from Porto (2015))

The lower release height ($H/R_0 = 2.8$) caused the near-surface total domain velocity and radial velocity to peak earlier ($t/T_0 = 9$ before the $Z/R_0 = 3.8$ release height) and with a higher magnitude by $V/V_0 = 0.1$.

In totality, the reduced wall influence from the added wall porosity and the lower release height used in this experimental study should result in higher radial and total domain velocities after impingement. These higher velocities should be not only the case against the URANS simulations but also when considered against past dense releases experiments by Alahyari and Longmire (1994), Alahyari (1995) and Yao and Lundgren (1996), where the release heights were all $Z/R_0 = 3.8$ and the release cylinder had solid walls.
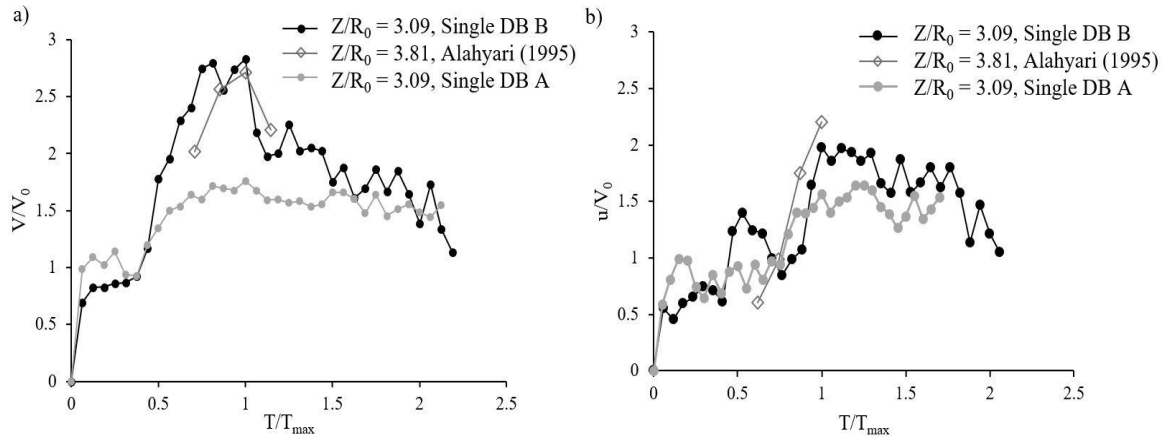
Figure 3-13 – Scaled maximum domain velocity and radial velocity over the entire time series for Single DB A and B normalized by the time of the maximum compared to Alahyari (1995)

The time history of the maximum total and radial velocity in the capture plane for the Single DB A and B release relative to release data from Alahyari (1995) is shown in Figure 3-13 (a) and (B). The time history of both maximum total and maximum radial velocity normalized by the time their respective maximum (T_{max}) to remove the influence that release height has on the maximum's timing. Though, this does not remove the limitation of the release height on this analysis. Alahyari (1995) used a release height $Z/R_0 = 0.72$ higher than both Single DB A and B, and this difference will account for the variation in velocity between the experiments. Single DB A had lower outflow velocities than Single DB B, and Alahyari's (1995) releases data. The maximum total velocity in Single DB B (Figure 3-13 (a)) was higher at $V/V_0 = 2.83$ then Alahyari's (1995) at $V/V_0 = 2.71$ (a difference of $V/V_0 = 0.12$). The case was not the same for the maximum in-plane radial velocity, which for the Single DB B was lower at $u/V_0 = 2.19$ compared to Alahyari's (1995) at $u/V_0 = 2.5$. Having a height maximum total domain velocity and lower maximum radial velocity over that which was reported in Alahyari's (1995) release experiments does not provide enough conclusive data to make any significant claims about the release systems performance beyond having a weaker outflow. Though the proximity of the maximum total velocity and the reduced maximum radial velocity in comparison to Alaharyi's (1995) release data (at a higher height) does support Babaei's (2018) claim that the onset of initial mixing weakens the releases from the system. The lower release height paired with the reduction in the wall effect (from the added porosity) should have resulted

in higher values of both the total and maximum radial velocities. Besides, the fact that the peak maximum radial velocity may be outside the plane of view is still a limitation that impacts this analysis. The highest velocities could be outside the view plane and occur at times outside the capture frequency.

Despite no conclusive evidence of improved performance through the addition of wall gates, the mixing and resulting weakening outflow may have an unintended benefit. In Yao and Lundgren (1996), it was found that the maximum velocity in their simulated downbursts was higher than that which has been recorded in field studies using the solid wall cylinder. A weaker outflow and lower ground velocities produced by the new cylinder may better represent full-scale events. This benefit is expanded upon through comparison to other release events and available full-scale data.

3.2   Evaluation of the Outflow Velocity Vector Fields from the PIV captures Against Past Studies and Field Data

The dense fluid release technique's primary purpose using the new release cylinder design was to improve the modelling of downburst outflows. The added wall gates were found to cause reduced near-ground velocities compared to the past release experiments of Alahyari and Longmire (1994) and Alahyari (1995). Capturing the maximum peak velocity in any outflow has proven challenging as getting measurement equipment in the peak location is hard both experimentally and in full-scale field studies. Currently, the Andrews Air force Base downburst study by Fujita (1985) has been the best know case with velocity data collected in the region close to the near-surface peak maximum velocity (Orf et al. 2007).

A maximum velocity of 67 *m/s* was recorded at the 1983 AFB downburst outflow (Fujita, 1985). Top outflow speeds of between 30 *m/s* to 37 *m/s* were recorded during the JAWS (Hjelmfelt, 1988) and NIMROD (Fujita, 1978). Solari (2020) noted field wind speed measurements of two studies covering large areas. The first study was by Greets (2001), who reported maximum wind speeds of up to 42 *m/s* over 20 to 33 years of recording across ten stations in New South Wales, Australia. The second study by Orwig and Schroeder

(2007) reported wind speeds above 30 *m/s* across an array of seven towers covering a line 1.5 *km* long. Considering the diverse range of downburst types, the range of atmospheric conditions, and the possible effects of topography, all paired with the limitations (spatial and temporal resolution) of capturing the maximum velocity near the ground, the field data suggests the typical maximum wind speed is above 30 *m/s*.

Yao and Lundgren (1992) used the field data from the DL191 (Fujita, 1986) flight recoding to develop the scaling parameters used for dense fluid release experiments (Section 2.3). They established scaling parameters (section 1.2.2) to scale up to full-scale atmospheric events utilizing a least-square fit. The following parameters are used to scale up to full scale: $R_0 = 0.632$ *km*, $V_0 = 36$ *m/s*, $T_0 = 17.6$ *s*. These three scaling parameters will be used to scale the releases to compare the outflow to full-scale simulations and field data. Table 3-2 summarizes the highest near-surface velocity magnitude and radial velocity magnitude for both releases A and B with data from Alahyari (1995) and Yao and Lundgren (1996)

The radial (X/R_0) location of the maximum radial velocity (u) in release A differs from Alahyari (1995) and Yao and Lundgren (1996) by $X/R_0 = 0.4$ while release B has a better agreement. Peak values of $u/V_0 = 1.64$ to $u/V_0 = 2.19$ were observed for Single DB A and B, respectively. These values are less than $u/V_0 = 2.4$ recorded in Alahyari (1995), but close to $u/V_0 = 2.17$ of Yao and Lundgren (1996). Once the vortex ring had formed and started to dissipate, the outflow had a depth of $Z/R_0 = 0.32$ to $Z/R_0 = 0.38$, with the vortex core remaining around $Z/R_0 = 0.5$ to $Z/R_0 = 0.4$ on the left-hand side of each event, which supports the observations of Alahyari (1995). The lift of the primary vortex occurred after $X/R_0 = 2.5$. Overall, the release events vertical velocity fields provide the observed flow field characteristics described in other dense fluid release models (Lundgren et al., 1992; Alahyari, 1995; Yao and Lundgren, 1996). The evolution follows the natural progression of full-scale downbursts (Fujita, 1985), and the peak outflow velocities are similar to past dense fluid models. Though there is noticeable variation in the outflow strength about the event centres, and Single DB A is weaker than Single DB B.

Table 3-2– summary of the radial locations and height of the maximum velocity magnitude and radial velocity for release DB A and DB B compared with data from Alahyari (1995) and Yoa and Lundgren (1996)

	Maximum Horizontal Velocity					
	$H/R_0 = 3.09$				$H/R_0 = 3.18$	
	Single DB A		Single DB A		Alahyari (1995)	Yao and Lundgren (1996)
	LH	RH	LH	RH		
u_{max}/V_0	1.59	1.64	1.93	2.19	2.40	2.17
Z/R_0 loc	0.14	0.21	0.14	0.24	0.15	0.05
X/R_0 loc	1.88	1.85	1.29	1.25	1.20	1.19
T/T_0	6.76	6.76	5.14	5.14	6.06 - 7.16	6.75
	Maximum Vertical Velocity					
w_{max}/V_0	1.85		2.07		2.50	
Z/R_0 loc	1.24		1.06		0.70	
T/T_0	4.05		4.05		6.06	
	Maximum Velocity					
	$H/R_0 = 3.09$				$H/R_0 = 3.18$	
	Single DB A		Single DB A		Alahyari (1995)	
	LH	RH	LH	RH		
V/V_0	1.75	2.19	2.16	2.19	2.26	
Z/R_0 loc	0.14	0.24	0.14	0.24	na	
X/R_0 loc	1.29	1.29	1.32	1.25	na	
T/T_0	4.32	4.86	5.14	5.14	na	

In the case of Single DB B, the maximum radial velocity of $VV_0 = 2.19$, at a radial extent of $X/R_0 = 1.25$, at the height of $Z/R_0 = 0.24$, occurring at a time of $T/T_0 = 5.14$ translates to a maximum radial velocity of 78 *m/s*, 0.8 *km* from the event centre at the height of 15 *m* occurring 90 *s* after the event reaches the ground. The maximum radial velocity of 78 *m/s* compares to Yao and Lundgren's (1996) estimation of 78 *m/s* and close to the maximum reported in the AFB downburst (Fujita, 1985) of 67 *m/s*. In numerical simulations using the CM1 model performed by Vermeire (2011a) and Oreskovic (2016), peak radial velocities range from 30 *m/s* to 65 *m/s*, lower than the 80 *m/s* scaled here. Considering

Single DB A, the peak radial velocity would scale to 62 *m/s*, which compares similarly. However, the numerical simulations have a high dependency on selecting the correct initial parameters (which, for the CM1 based studies discussed here, are relative to a selected natural event). Oreskovic (2016) investigated the outflow velocity's dependence on the CS's initial height and shape. Oreskovic (2016) found that the CS height and shape impacted the location of the maximum velocity in the outflow as the cooling source size and growth are spatially and temporally dependent. An absolute comparison to full-scale events will be hard to perform as there is a strong dependency on the spatial resolution (location) of the measuring equipment to the downburst centre and due to the wide range of strength of environmental events. Noted in Alahyari and Longmire (1994), the DL191 downburst event's wind speed was recorded at $X/R_0 = 7$ from the event centre. In the AFB downburst, maximum velocities of 67 *m/s* at 4.9 *m* AGL close to the maximum region have been recorded. Maximum velocities closer to a full-scale event centre may be higher than what has been recorded. However, the diverse range of conditions limits any assumption that can be made on the absolute maximum that can occur in a full-scale event.
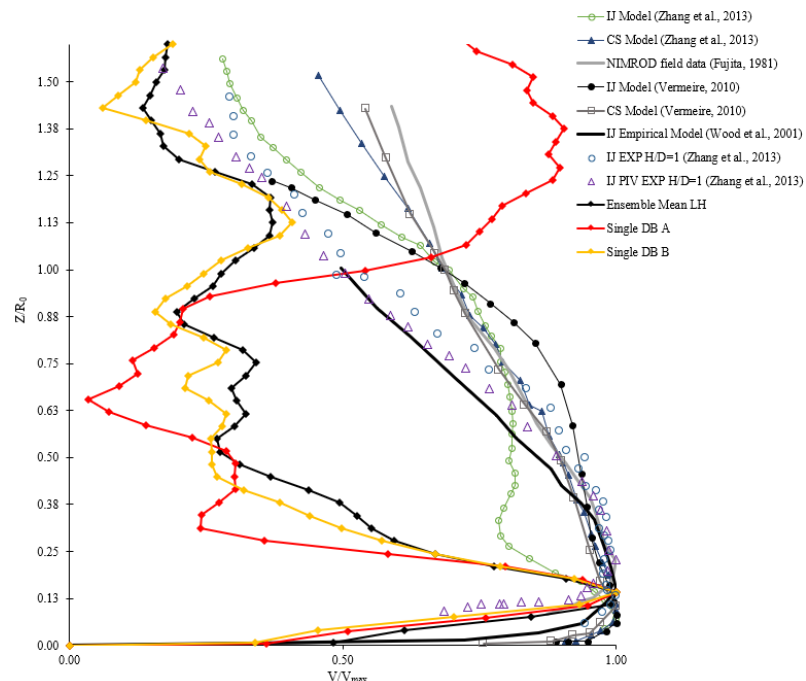
Figure 3-14 – vertical velocity profiles at the radial and horizontal location of the maximum near-surface velocity for the single releases compared to a selection of other modelling techniques

The new release's outflow velocity field can be better interpreted by considering the vertical and horizontal profiles at the time and radial and horizontal location of the maximum near-surface velocity. Field data combined with IJ numerical and experimental models and CS numerical models have been added to help evaluate the new cylinder's outflow to other modelling techniques. Figure 3-14 shows the vertical profiles of velocity normalized by the maximum (V_{max}) for Single DB A at $X/R_0 = 1.90$, $Z/R_0 = 0.21$, $t/T_0 = 6.76$, Single DB B at $X/R_0 = 1.25$, $Z/R_0 = 0.24$, $t/T_0 = 5.14$, and the ensemble average at $X/R_0 = 1.66$, $Z/R_0 = 0.24$, $t/T_0 = 5.41$. Figure 3-15 shows the radial profiles through the same points for all releases compared to past simulated methods and available field data.
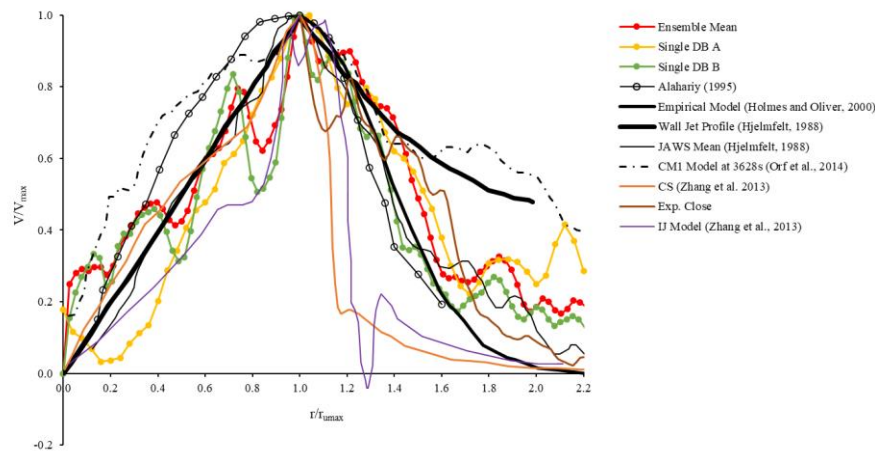
Figure 3-15 - horizontal normalized velocity profiles scaled about the radial location of the max near-ground velocity

Both plots, Figure 3-14 and Figure 3-15, are normalized by the maximum's location as it is the maximum value that is of interest to engineers. Each profile used was selected within the spatial and temporal vicinity of the maximum near-surface velocity for the same reason. This selection is essential as downburst events are highly transient. It should be noted that the maximum velocity reported in each case is dependent on when and where the data was extracted. Choosing to plot the vertical and horizontal velocity profiles at the maximum's time and location serves as the best means to compare simulated methods while limiting the effects of the transient nature of all techniques events. The field data presented

represent the average of NIMROD (Fujita, 1985) for Figure 3-14 and JAWS (Hjelmfelt, 1988) in Figure 3-15. Each data set was collected by doppler with a fixed time and spatial range, and so each can be viewed as a generalization of an entire full-scale event. The empirical function created by Holmes and Oliver (2000) captures this general shape for the horizontal profiles observed in NIMROD. Wood et al. (2001) 's empirical function captures the shape up to and after the maximum for simulated IJ downbursts.

In the vertical profile data of Figure 3-14, there is a considerable reduction (about 25% of the V_{max}) between $Z/R_0 = 0.88$ and $Z/R_0 = 0.38$ in all releases by the new cylinder design. This reduction is shown by the contraction that occurs as the outflow is forced outward before the vortex ring reaches the ground. Figure 3-16 highlights this contraction by a red ellipse with a yellow line showing the approximate location of the vertical profiles' radial site for the left side of the event centre.
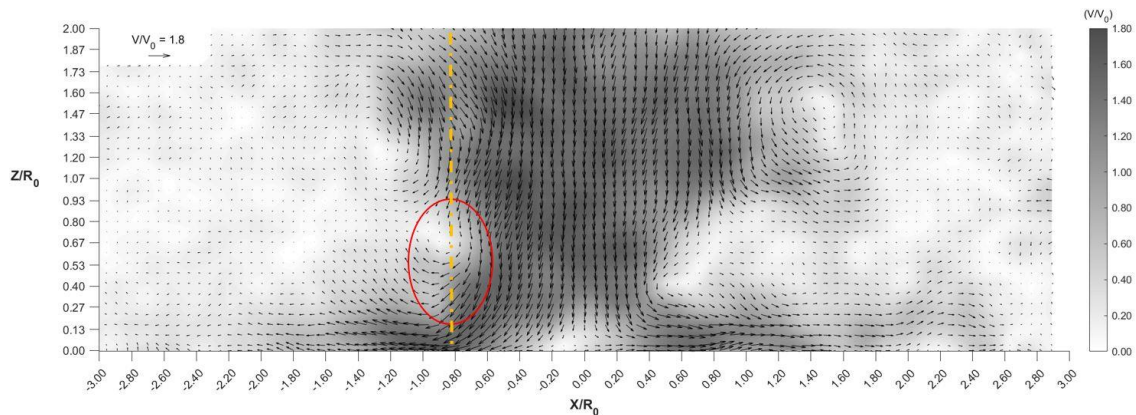
Figure 3-16 – The vertical velocity profiles' contraction at the radial location of the maximum indicated by the yellow line. The red ellipse highlights the region of reduced velocity

This is due to the lead edge of the descending fluid not being contained in a single mass. In some releases, the leading edge is broken into various dense fluid regions that contact the ground before the rest of the dense mass. When this happens, ambient fluid regions are left in between the fluid that has impinged and the remaining falling mass, which creates areas of low velocity. Figure 3-30 shows this happening in the horizontal vector fields.

At the maximum and thereafter, a close agreement between the PIV data of the IJ model from Zhang et al. (2013) and all the release cases was found. However, there is a deviation

in the trend with the numerical cases of Vermeire et al. (2011a) and Zhang et al. (2013) along with the empirical model of Holmes and Oliver (2000) and the field data of NIMROD (Fujita, 1985). As the PIV from this study and the PIV results from Zhang et al. (2013) reach a close agreement in the near-ground region after the maximum, it may be a possibility that this is a consistent result of using PIV. The limited resolution, camera alignment, and particle interference along the ground that occurs in PIV could be affecting the near-ground region. Zhang et al. (2013) attributed that poor agreement to surface roughness differences.

The horizontal profiles follow the empirical function of Holmes and Oliver (2001) both up to and after the maximum. Dips and spikes are present up to the maximum. These are an indication that velocity was fluctuating in and out of the plane of view. The profiles shown are instantaneous captures of transient flows with no smoothing applied, accounting for the variation seen up to the maximum. The IJ and CS simulation by Zhang et al. (2013) show a poor agreement to all data, including the release by the new cylinder. Again, this variation in agreement further supports Oreskovic's (2016) conclusion about the effect of initial conditions on numerical simulations of downbursts.

Beyond the vertical and radial profiles of velocity, the radial and horizontal propagation of a downburst front can also compare different experimental and numerical techniques. Babaei (2018) demonstrated that the novel release system used in this study was able to produce release events with radial and horizontal propagations that fit the past dense fluid models of Lundgren et al. (1992), Alahyari and Longmire (1994), Alahyari (1995) and Yao and Lundgren (1996). A good agreement with the numerical and experimental works of Roberto et al. (2015), as displayed in Figure 3-19, was also shown. It must be noted that all of the cases shown are based on an intensity threshold (as discussed in Section 3.1) from PLIF vertical plane experiments. These experiments feature high contrast based on the intensity difference between the fluorescent dye (Rhodamine B) impregnated dense fluid and the dye-free ambient background fluid. The mixing in the fluid interface interaction region has a lower intensity than the unmixed dense fluid. The contrast relative to the ambient fluid, even in the mixed regions, makes discerning the dense fluid front from the ambient fluid consistent when based on a specified intensity (Figure 3-17).
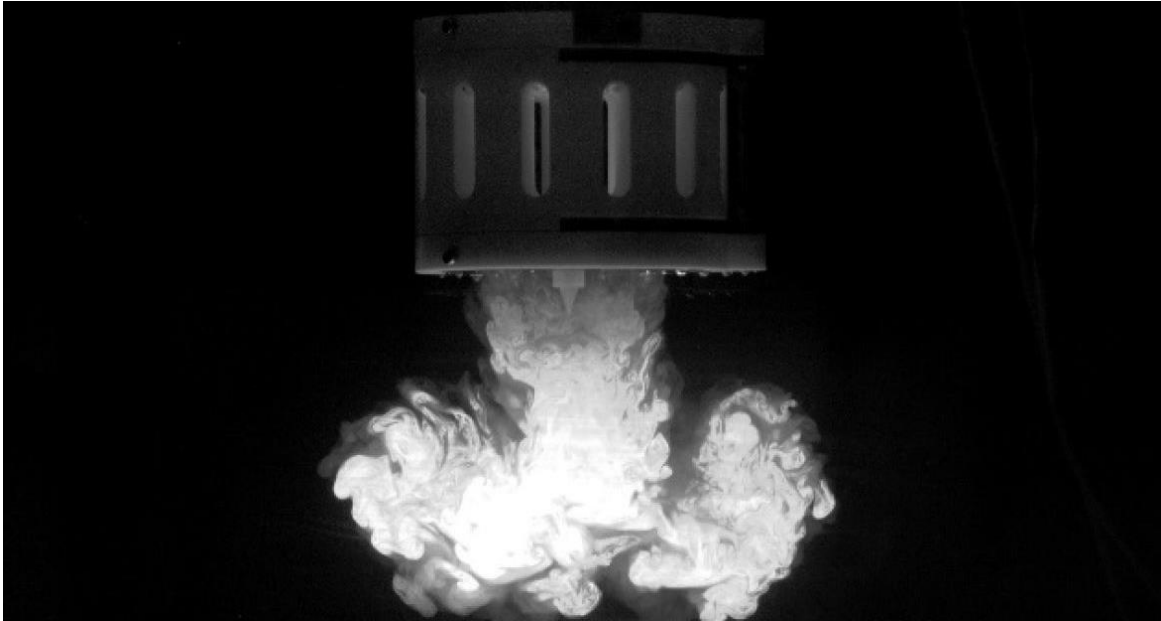
Figure 3-17 - High contrast PLIF capture example of a single downburst release using the system in this study (adapted from Babaei, 2018)

The two single stationary releases, Single DB A and Single DB B, were both performed solely as PIV experiments. Therefore, only vector fields were available to track the dense fluid front both horizontally by the time evolution of the radius and vertically by the time evolution of the event descent. A velocity based threshold was needed to define the leading edge in both the descent and radial spread of each release event.

Two approaches were taken for determining the threshold velocity value: one based on a percentage of the absolute maximum velocity and the other based on acceleration. Twelve points were taken through the centerline of each release; the time history of the velocity magnitude (V) was plotted for each release (Figure 3-18 (a) for Single DB A, and (b) for Single DB B). The velocity magnitude (V) and time (T) were both normalized by the maximum (V_{max} and T_{max}) through each point. Normalizing by the time and associated velocity at the maximum contracted the data about one, which should have made the frontal progression visible from $T/T_{max} = 0$ to $T/T_{max} = 1$ as an increased slope from the highest point to the lowest point.
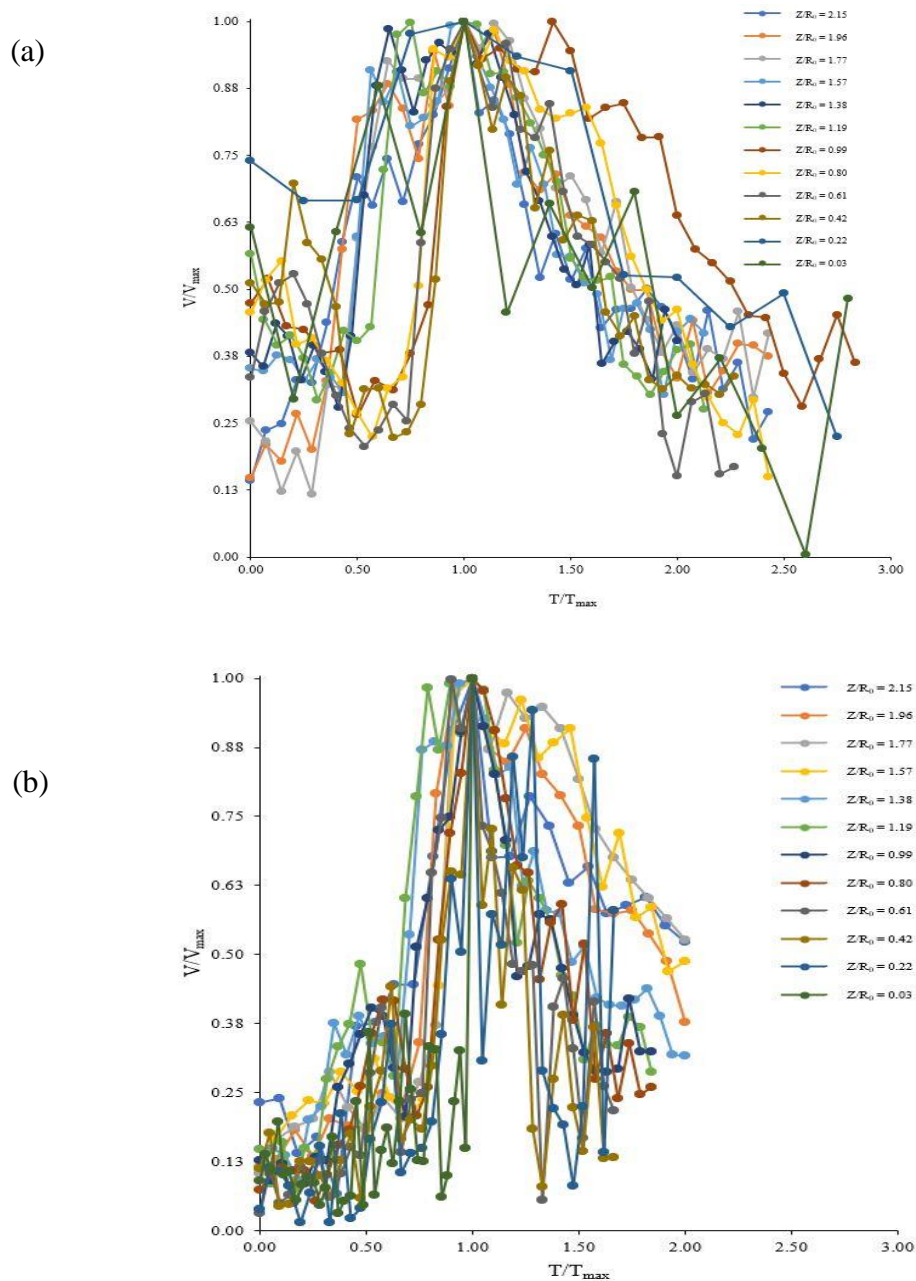
Figure 3-18 – time history of velocity through the centreline of (a) release Single DB A and (b) Single DB B at 12 heights from the ground to the top of the plane of view

Figure 3-18 shows that significant background motion is present before the downburst front passes through each vertical point. A variation between $V/V_{max} = 0.04$ to $V/V_{max} = 0.25$ from $T/T_{max} = 0$ to $T/T_{max} = 0.8$ was recorded for Single DB B. Single DB A had a larger variation, up to 75% of the V_{max}. Ideally, the PIV particles' background motion would have been relatively small compared to those in the dense release fluid. The small motion would

have made discerning the front arrival at each of the twelve points clear compared to the background.
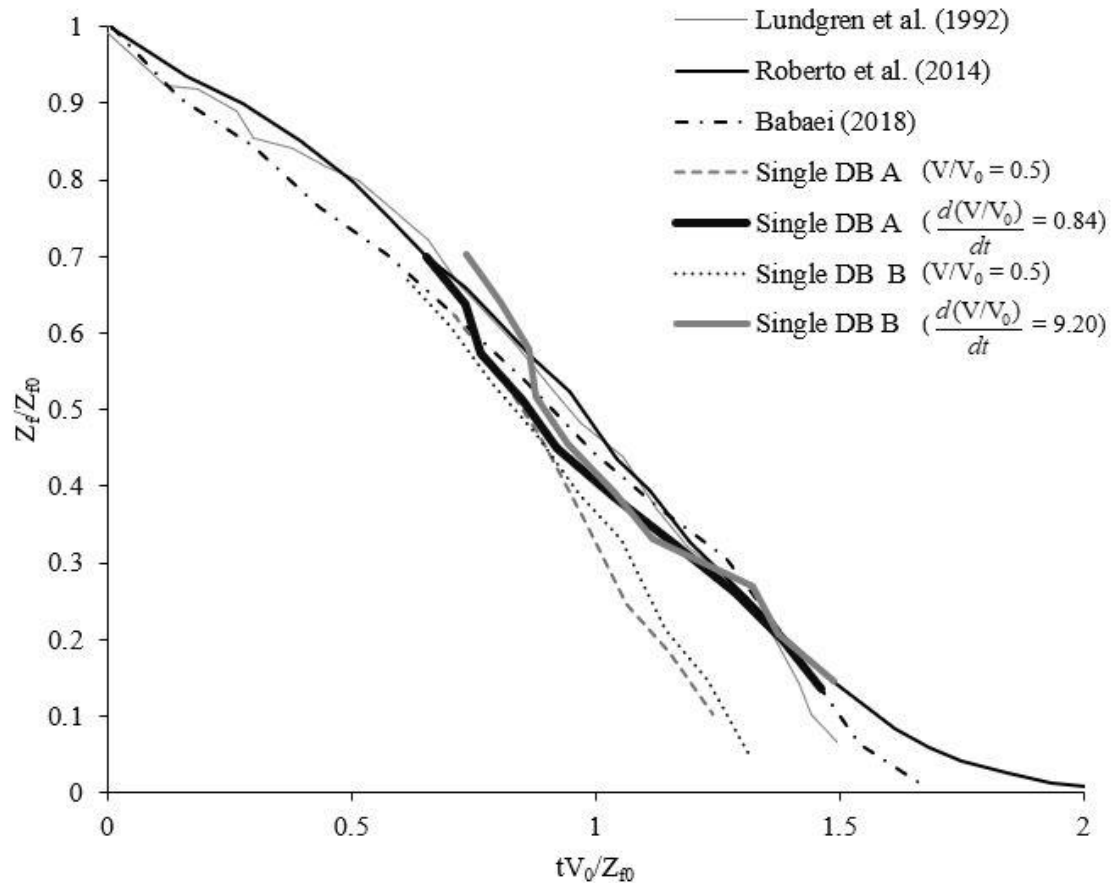
Figure 3-19 – Vertical propagation of the downburst front comparison using different velocity and acceleration thresholds

A velocity threshold of $V/V_0 = 0.5$ was selected as a starting point. In Single DB B, the background motion before the arrival of the downburst front was 0.025 m/s or 10% of the maximum, though is Single DB A it was less clear with values ranging between 13% to 75% of the maximum velocity. An amount of 50% was decided to be a good start. The twelve data points in the vertical direction over the entire time-series were monitored for velocity magnitude values within ±5% of $V/V_0 = 0.5$ and used to produce Figure 3-19. The front height from the ground (Z_f) was plotted normalized by the release height (Z_{f0}) over time scaled by V_0 and the release height. By scaling time in this manner, the difference in release height can be removed from the data as long as the height allows for the circulation

in the flow to develop fully (Lundgren et al., 1992). The 50% criterion created a vertical descent with a slope steeper than that reported by Babaei (2018) using the same system. An acceleration threshold was investigated as a means to capture the front arrival over velocity. Though the background had a high-velocity relative to the approaching front, its acceleration was much less than that of the approaching front. This low acceleration meant that the approaching front's acceleration had a lower threshold value than obtained solely using the velocity.
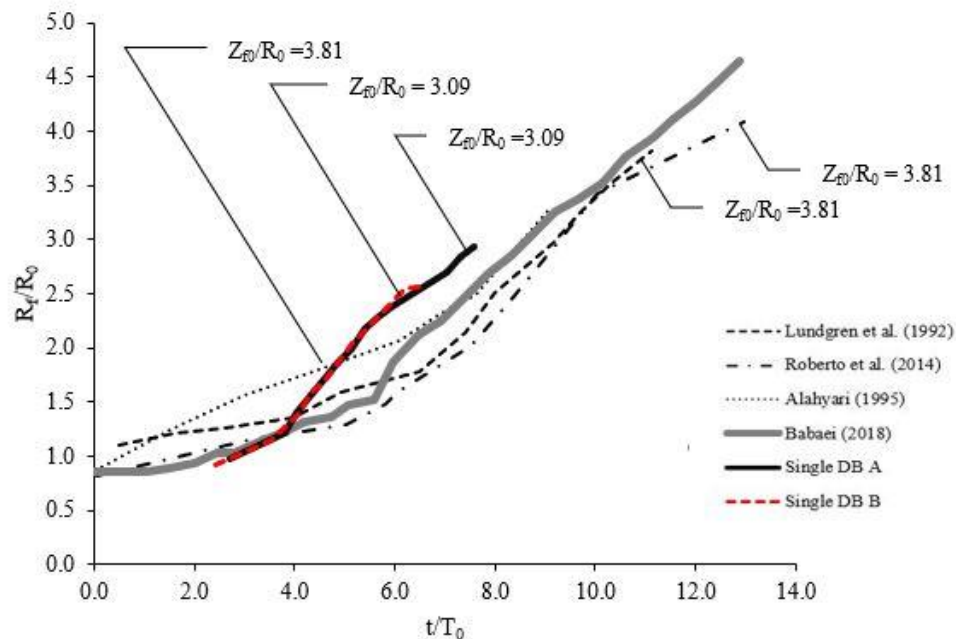
Figure 3-20 – Normalized Radial propagation of both release events using different velocity and acceleration magnitudes to define the leading edge

Figure 3-19 shows that using accelerations of 0.1 m/s^2 (d(V/V$_0$)/dt = 0.84) to 1.1 m/s^2 (d(V/V$_0$)/dt = 9.2) leads to tracking the front head with a reasonable agreement to past experiments in the same facility Roberto et al. (2014) with the same release system Babaei (2018). A lower acceleration threshold was needed for Single DB A as the event had a weaker outflow compared to Single DB B. Smaller values of acceleration as a threshold would have been ideal for indicating when the front had reached a particular point in space and time. It was clear, though, that there was still a limitation from background motion and so choosing smaller values, those below 0.24 m/s^2, were not possible.

Figure 3-20 shows the event's radial propagation based on measurements made from the event centre out to the left-hand side. The same acceleration thresholds used in the vertical descent were also applied for the radial propagation. The radial propagation slope during descent and after impingement is similar to all past dense fluid release experiments. The primary difference noted here is the release height. The release height used in this study was $H/R_0 = 3.09$. The result is that both Single DB A and B reach the ground before the other event is plotted. The acceleration threshold provides propagation profiles that match well with the PLIF data from Babaei (2018) and further validate that the novel release system can produce scaled downburst events with the expected outflow characteristics even though the side gates weaken the outflow.

The near-ground velocity field and radial propagation of a downburst are a result of the horizontal roll vortex. Aside from considering the velocity fields, analysis of the vortical structures further develops an understanding of the outflow of downbursts.

3.3   Vortical structures in the outflow

The horizontal vortex roll is the primary vortical feature of the outflow and an essential aspect of the near-surface wind hazard of a downburst event. The λ_2 criterion (Jeong and Hussain, 1995; Chen et al., 2015) was used to identify the vortex core as it was formed during descent and over its dissipation after impingement. λ_2 criterion places a strict limitation on identifying vortices as it has been shown to reject weaker vortices better than other identification methods (Chen et al., 2015). Vortices are identified as iso-surfaces from connected regions of two negative eigenvalue vectors of the equivalent Hessian pressure tensor (Jeong and Hussain, 1995).

The pressure Hessian can be obtained by taking the gradient of the Navier-Stokes equation (Eq. 3-2) for an incompressible planar flow (Chen et al., 2015):

$$\frac{\partial V}{\partial t} + \nabla((V\Box\nabla)V) = -\frac{1}{\rho}(\nabla P) + v\nabla^2(\nabla V)$$

3-2

where V is the velocity gradient tensor. The pressure Hessian is simplified by neglecting the unsteady irrotational strain and viscosity as (Chen et al., 2015):

$$S^2 + \Omega^2 = -\frac{1}{\rho}\nabla(\nabla P)$$

3-3

where S is the rate of strain tensor and Ω the rate of rotation tensor. A local pressure minimum requires that the right-hand side of equation 3-3 has two positive eigenvalues (Chen et al., 2015). This is equivalent to the left-hand side of equation 3-3, having two negative eigenvalues under the same condition. The λ_2 criterion then identifies connected regions of negative λ_2 as vortices. The λ_2 can be computed as equation 3-4 (Chen et al., 2015) by using the 2-dimension velocity gradient vector:

$$\lambda_2 = \left(\frac{\partial u}{\partial y}\frac{\partial v}{\partial x} - \frac{\partial u}{\partial x}\frac{\partial v}{\partial y}\right) + \frac{1}{2}\left(\frac{\partial u}{\partial x} + \frac{\partial v}{\partial y}\right)^2 + \frac{1}{2}\left|\frac{\partial u}{\partial x} + \frac{\partial v}{\partial y}\right|\sqrt{\left(\frac{\partial u}{\partial x} - \frac{\partial v}{\partial y}\right)^2 + \left(\frac{\partial u}{\partial y} + \frac{\partial v}{\partial x}\right)^2}$$

3-4

Therefore, in its simplest explanation, the λ_2 criterion uses the concept of low pressure in the core of a vortex to identify the vortex core over other methods. The ability to reject regions of weak vorticity helped identify the centre of the horizontal roll vortex in the presented release experiments over the weaker secondary and background motion-based vortices present in the vector fields. The outflow of a downburst is turbulent and combined with the limited resolution of the PIV CCD and the interrogation window size of post-processing, capturing vorticial structures with no relation to the primary vortex ring as can be seen in Figure 3-21 (b). Rejection of these structures, indicated by light contours of red, enabled the vortex ring to be identified.

The high contrast of red indicates the magnitude of the λ_2 criterion for each vector field in Figure 3-21 to Figure 3-24. Regions of high vorticity are identified as dark red, and lighter shades of red identify weaker vorticity areas. A filtering algorithm based on a threshold value (δ_λ) of λ_2 was used to reject weak vortical structures. The threshold value is

dependent on the particular flow being analyzed (Chen et al., 2015). In this study, a $\delta_\lambda = -40$ was used to identify the vortex core in most frames. With the vortex core identified, plots of the centre location of the core concerning the event centres for both release A and B were made. The vortex core trajectory presents a new opportunity to scale simulated and full-scale events and will be explored using the λ_2 criterion. Figure 3-21 (a) shows λ_2 scalar fields of Single DB A at $t/T_0 =$ and Single DB B at $t/T_0 =$ as the initial vortical structures forming as baroclinic vorticity generation begins along the events leading edge. Figure 3-22 to Figure 3-24 shows the progression of the primary vortex throughout its horizontal propagation. The secondary vortex (noted by Yao and Lundgren (1996)) is only visible in Figure 3-24 (b) just below the left-hand horizontal roll vortex as it has lifted. The secondary vortex is caused by contour vorticity that forms from shear along the ground
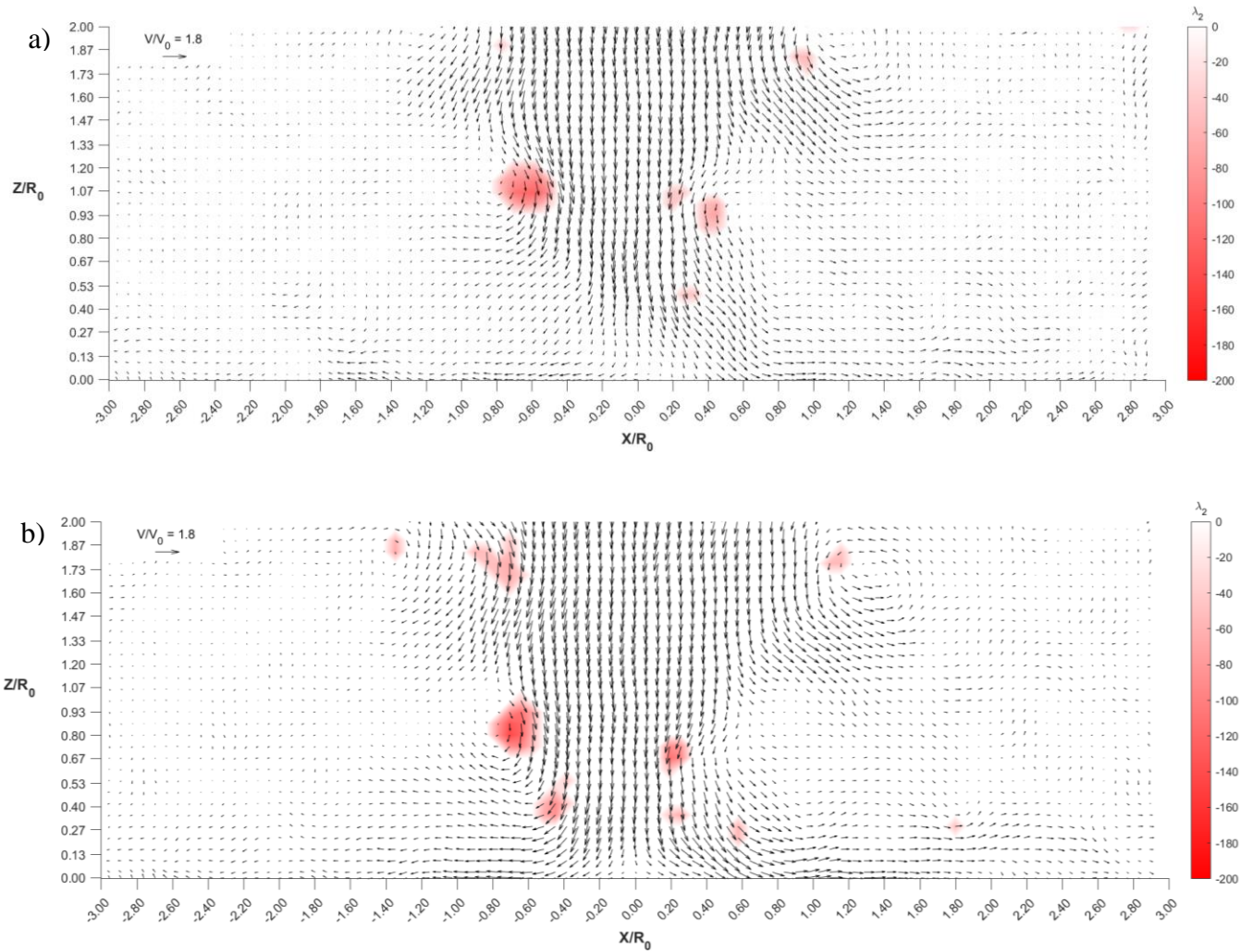
Figure 3-21 – Iso-surfaces of λ_2 showing regions of vorticity for (a) Single DB A at $t/T_0 = 2.97$, (b) for Single DB A at $t/T_0 = 4.05$
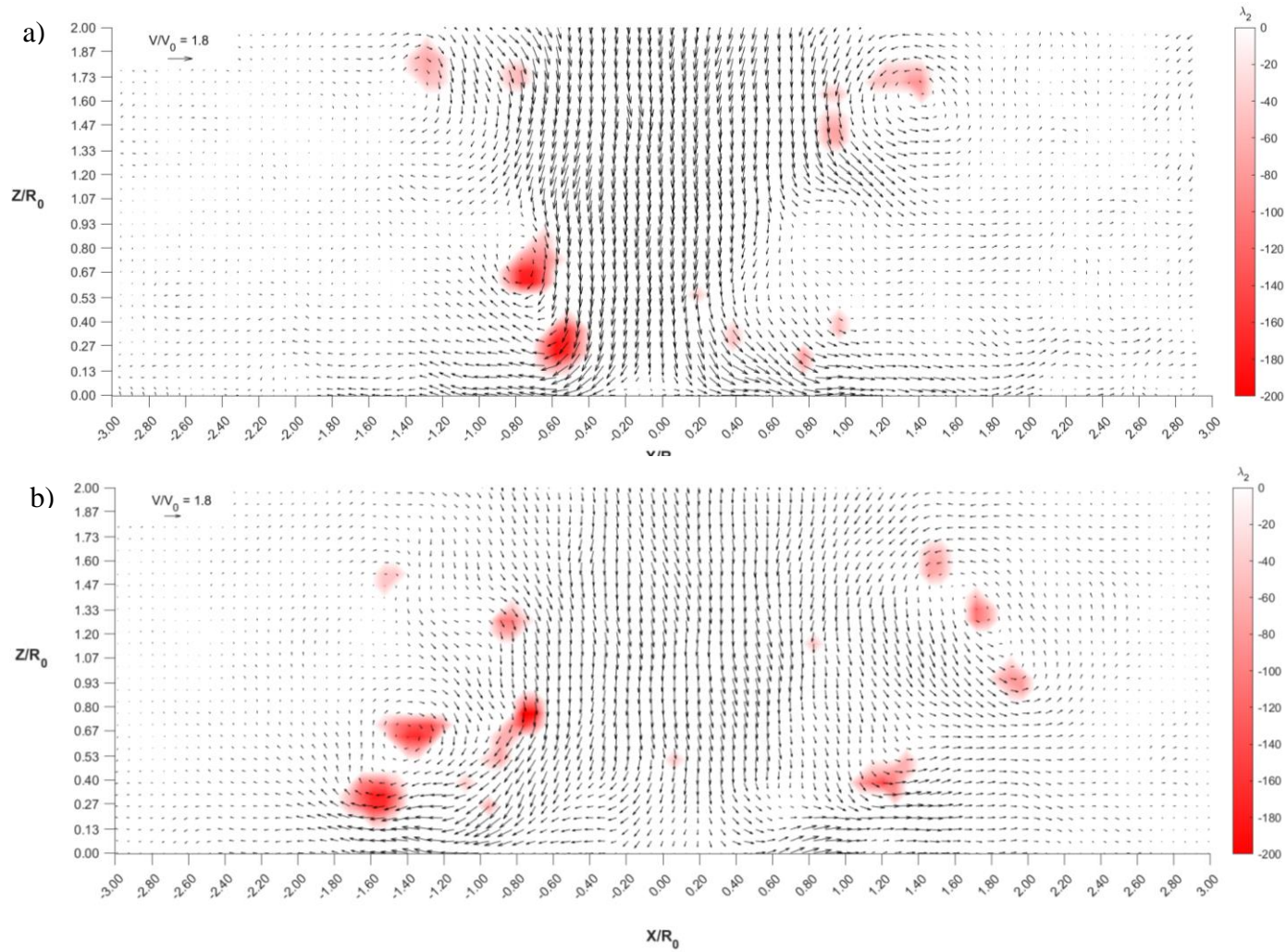
Figure 3-22 - Iso-surfaces of λ₂ showing regions of vorticity for (a) Single DB A at t/T₀ = 4.32, (b) for Single DB B at t/T₀ = 5.13
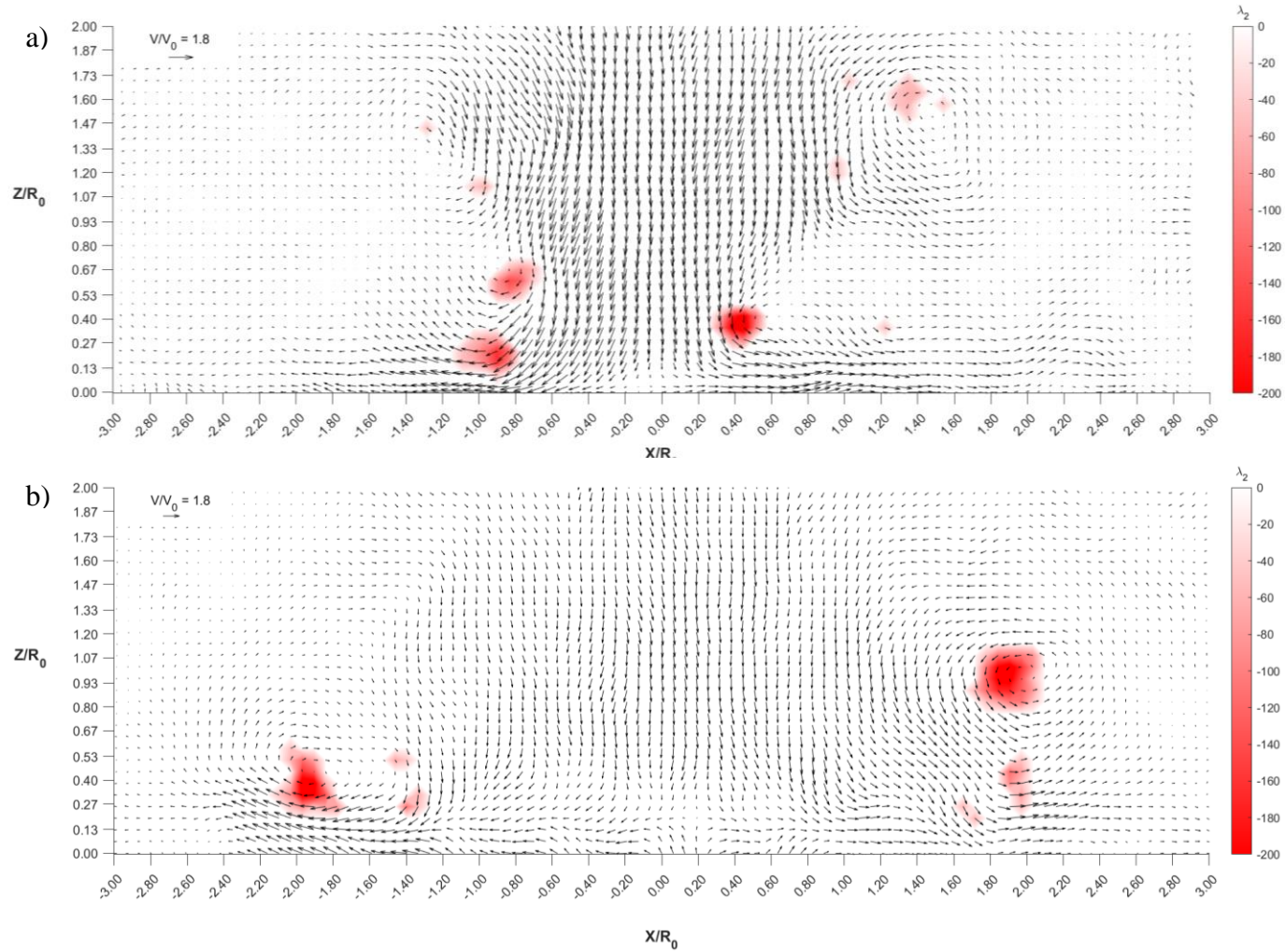
Figure 3-23 - Iso-surfaces of λ_2 showing regions of vorticity for (a) Single DB A at t/T$_0$ = 4.87, (b) for Single DB B at t/T$_0$ = 5.95
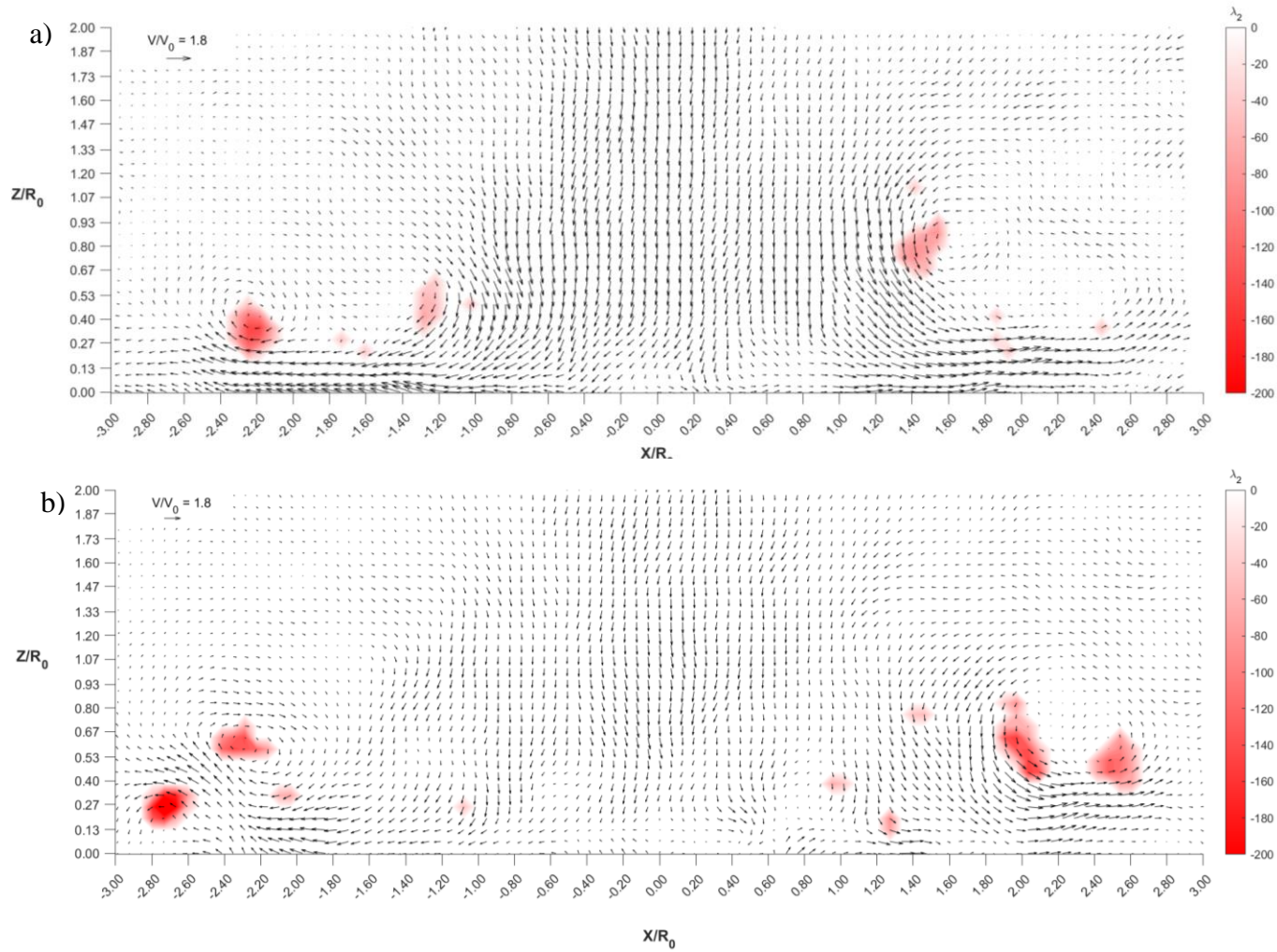
Figure 3-24 - Iso-surfaces of λ_2 showing regions of vorticity for (a) Single DB A at t/T$_0$ = 6.76, (b) for Single DB B at t/T$_0$ = 6.7

3.4   Vortex Trajectory as Scaling

The radial velocities in the near-surface region are affected by the horizontal roll vortex interaction with the ground. This vortical structure's stretching and tilting amplify the radial velocity close to the ground, leading to an entire downburst event's maximum peak value. As this is the case, the height, radial location, and time history of the horizontal roll vortex core location are essential in characterizing the outflow of a downburst event. Considering these locational aspects can serve as a method to scale and compare the outflow of experimental, numerical, and natural downbursts.

A plot (Figure 3-25 (a)) of the horizontal roll vortex core height to the radial location shows the vortex core descending and travelling along the ground plane for the two releases. The characteristic length scale R_0 normalizes the vortex core height and radial location. After reaching the ground, the horizontal vortex roll travels at a constant height of $Z/R_0 = 4.7$, between $X/R_0 = 1.5$ to $X/R_0 = 2.0$, before pitching upwards. A plot of the normalized time history of the vortex core height (Figure 3-25 (b)) captures a similar trend between $t/T_0 = 5.4$ to $t/T_0 = 6$ for both releases.
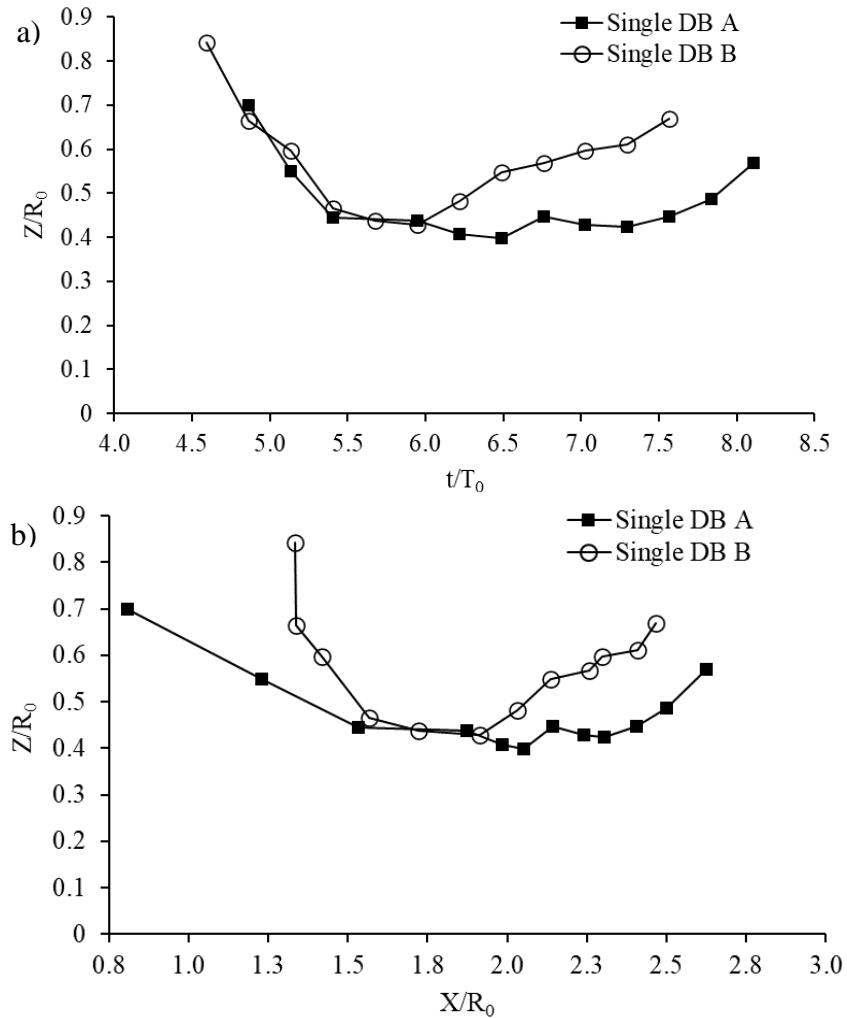
Figure 3-25 – (a) left-hand side vortex core height to the radial location from the centreline of release Single DB A (t/T$_0$ = 4.86 to t/T$_0$ = 8.38) and Single DB B (t/T$_0$ = 4.52 to t/T$_0$ = 7.57), (b) corresponding time history of the vortex height from the centreline of Single DB A (X/R$_0$ = 0.81 to X/R$_0$ = 2.76) and Single DB B (X/R$_0$ = 1.42 to X/R$_0$ = 2.47)

The highest near-ground outflow velocities are recorded at this lowest height between these radial locations and respective times. The baroclinic vorticity generation mechanism causes this to happen, as noted in Vermeire et al. (2011a). The buoyancy gradient causes a strong rotation about the core after the ground stops the vortex cores descent. The radial velocity about the center is then forced parallel to the ground, which amplifies its magnitude. As this is the case, it becomes possible to use the lowest height in the vortex cores trajectory as a scaling point. This approach was applied by Chowdhury (2018) to the

IJ downburst outflows from the WindEEE facility. Figure 3-26 shows the two release cases scaled by the height and radial location of the lowest horizontal roll vortex core height (Z_{min}) and radial location (X_{min}). Figure 3-26 also shows two examples from Chowdhury (2018) (Re = 1.82×10^6 for height to nozzle diameter (H/D) <1 and Re = 4.24×10^6 for H/D>1) that best matched the core height data from Wakimoto's (1982) analysis of the June 16 and June 17, 1978, downburst cases.
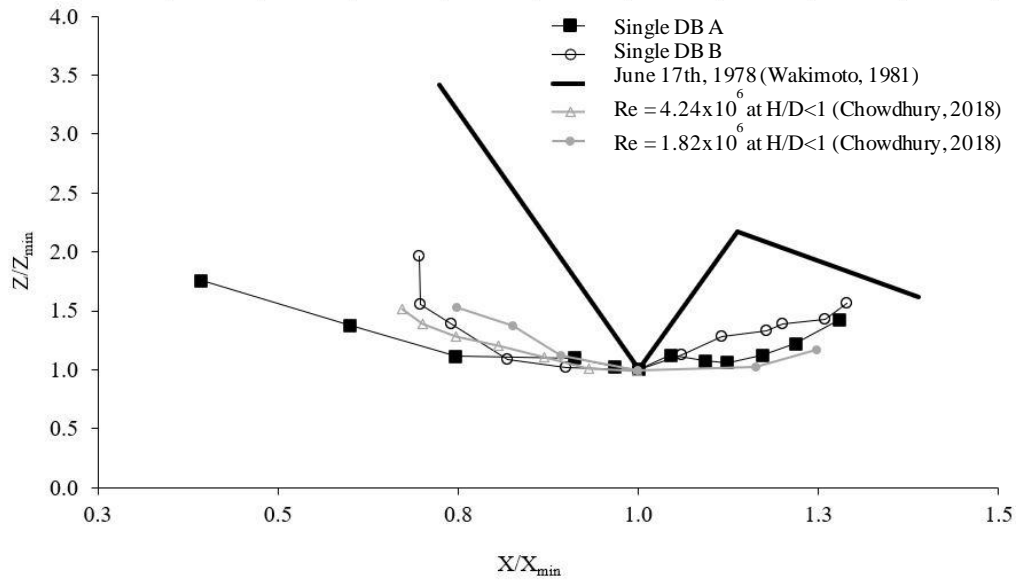
Figure 3-26– (a) left-hand side vortex core height (Z) normalized by the height of the minimum vortex height (Z_{min}) to the radial location (X) from the centreline of release Single DB A (t/T_0 = 4.86 to t/T_0 = 8.38) and Single DB B (t/T_0 = 4.52 to t/T_0 = 7.57) normalized by the location of the minimum height (Z_{min})

The trajectory of the dense fluid releases and IJ experiments from WindEEE by Chowdhury (2018) match well when scaled by the location of the lowest point vortex core point. Only a general trend can be seen with field data from the June 17, 1978, downburst from Wakimoto (1981). The low spatial resolution in the natural downburst trajectory from June 17, 1978, from Wakimoto (1982) limits any possible conclusions that can be made. However, the June 17th data does show that the vortex core descends to the height and radial location of the maximum radial velocity before translating upwards.

It is possible to conclude that there is a similarity in the horizontal vortex roll's spatial location based on the radial site of maximum radial velocity. As this is the case, the same will be valid for the core trajectory in time. As this is the case, scaling downburst events based on the horizontal vortex core trajectory in space and time is a suitable means of validating numerical and experimental models to full-scale data.

The time history of the vortex trajectory for a numerical CS and IJ model was provided by Zhang et al. (2013).
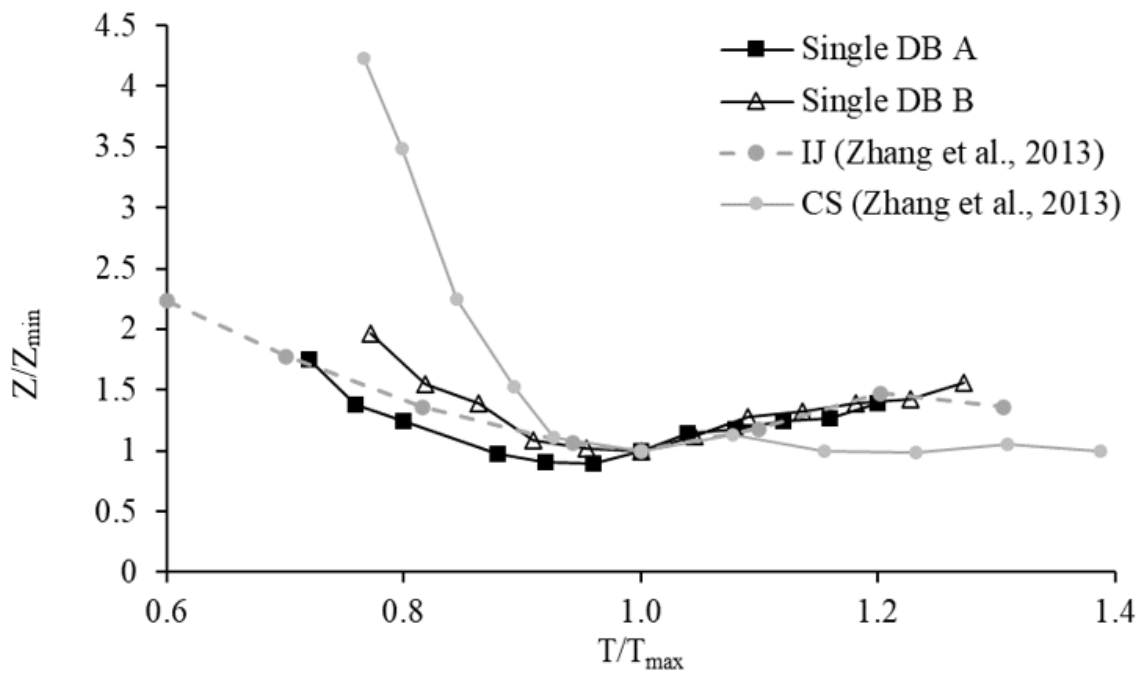
Figure 3-27 - (a) left-hand side vortex core height (Z) normalized by the height of the minimum vortex height (Z$_{min}$) over time (T) from the centreline of release Single DB A and Single DB B normalized by the time of the maximum radial velocity (T$_{max}$)

Aside from using the height and radial location of the lowest point in the vortex cores trajectory, an alternative length scaling approach exists using the core's horizontal diameter (D$_V$) and centre height (C$_z$) as detailed in Vermeire (2011c) (Figure 3-28).
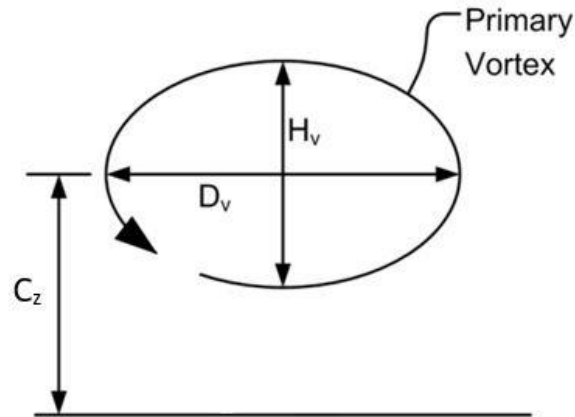
Figure 3-28 – Diagram of the length scales based on the vortex core (adapted from Vermeire, 2011, c)

The vortex core's horizontal diameter was measured at each location based on the λ_2 vortex core identification criterion. A threshold value (δ_L) based on λ_2 of δ_L>-85 was used to determine the vortex core's edges for measuring D_V. It should be noted that the vortex core's diameter is dependent on how well-formed the horizontal roll vortex is in the plane of view. The vortex core part of a radial three-dimensional vortical structure and the core's diameter is prone to variation as this structure fluctuates in and out of the plane of view. Figure 3-29 shows the time history of the height of the horizontal roll vortex core scaled by R_0 for both releases compared to the low surface roughness IJ and CS models from Vermeire (2011c). The nondimensional time ($T = t/T_0$) is scaled by when the maximum radial velocity occurs (T_{max}).
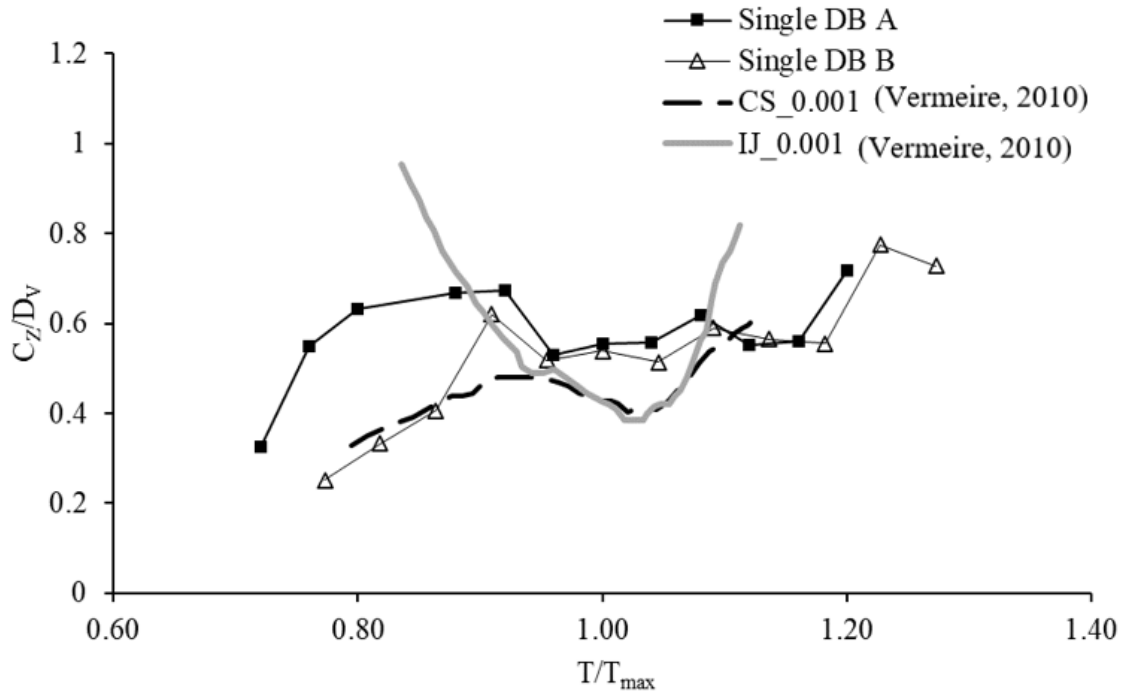
Figure 3-29 – Time series of the horizontal vortex core trajectory for the releases of Single DB A and B using the vortex core width (C_z) to height (D_v) aspect ratio normalized by the time of the max radial velocity (T_{max})

The vortex core width to height AGL (Above Ground Level) aspect ratio over time for Single DB A and B are in close agreement after the maximum radial velocity occurs ($T/T_{max} = 1$). Both event's horizontal vortex cores then follow a similar path in time with a similar height to the vortex core width ratio after impingement. This similarity provides support for repeatability using the new cylinder. However, in the time leading up to the maximum, there is a large deviation between the two releases. Release A showed a curved growth in the aspect ratio over B, which followed Vermeire's (2010) CS simulation. The variation can be attributed to the complex formation of the vortical structure witch can fluctuate in size across the view plane. The IJ simulation by Vermeire (2010) was shown to have rapid growth in the core width to height AGL ratio after reaching the maximum. The rapid growth suggests that the IJ models horizontal vortex core diametre decrease more rapidly than the vortex cores from both CS simulated and dense fluid released downburst simulations. The rapid growth in the aspect ratio of the IJ model highlights the importance that baroclinic vorticity generation has on the horizontal roll vortex after impingement in

density-driven simulations. Vermeire et al. (2011b) showed that baroclinic vorticity generation was significant in the near-surface region after impingement in the CS simulated downbursts. It is the buoyancy gradient that drives the horizontal vortex rolls growth and propagation along the ground. This is in contrast to the IJ model, where momentum in a mono-phase flow is the only driving factor for the horizontal vortex rolls ground prorogation. Scaling the trajectory in time or space (Figure 3-25, Figure 3-26, and Figure 3-27), using the vortex core's height only does not capture the significance of the mechanism for vorticity generation in the outflow between the different simulation techniques. However, this method has a high degree of variability, even though it captures the importance of the outflow's vorticity generation. As mentioned above, the core's diameter is prone to change as the 3-D structure of the horizontal roll vortex fluctuates through the view plane. The variability could be better captured by having a more extensive data set for all techniques.

The vortex trajectory tracking proves to provide a reasonable method to scale downburst events. The technique can be further developed by incorporating more field data with a better temporal and spatial resolution of the horizontal roll vortex.

The flow structure of the outflow in the vertical plane is not the only reference plane to characterizing full-scale to simulated experimental and numerical downbursts. The horizontal plane offers additional information of a downburst outflow that is useful in understanding and scaling downbursts.

3.5   Horizontal Velocity Vector Fields

Horizontal PIV images were captured to provide more detail into the 3D outflow velocity field. The initial conditions are discussed in Section 2.4.2, with each capture taken at the height of $Z/R_0 = 0.16$ (or $7mm$). This height was determined to give the best chance of capturing the maximum radial velocity based on the data reported in **Error! Reference source not found.**; above $Z/R_0 = 0.14$ and below $Z/R_0 = 0.24$. The release cylinder was centred in the field of view to capture as much of the outflow as possible. It should be noted

that these horizontal captures are independent events from Single DB A and B performed in the vertical plane. Figure 3-30 (a) and (b) to Figure 3-31 (a) and (b) show the time sequence of a single release event. Scaled by (Eq. 2.5), the times of each image are $t/T_0 = 4.05$, $t/T_0 = 5.95$, $t/T_0 = 6.76$, and $t/T_0 = 7.30$. The circular sections of no velocity (white regions) represent the interference from the reflection of the release cylinder in the field of view. The interference was a result of the cylinders being made of white plastic. Future studies should investigate painting the bottom of the cylinder black to reduce interference. The radial location of the interference region (between $r/R_0 = 1$ and $r/R_0 = 1.2$) covers the area where the maximum radial velocity was expected to occur and limits this analysis to regions beyond the maximum.

The asymmetry found in the vertical plane releases of Single DB A and Single DB B can also be seen in the horizontal plane release. The left-hand side experiences less outflow that weakens more so than the right-hand side, as seen between $t/T_0 = 5.95$ (Figure 3-30 a) to $t/T_0 = 6.76$ (Figure 3-31 a). Variation in the distribution of velocity about the event circumference can be seen in all velocity vector fields shown. The mixing of the dense and ambient fluid caused by the buoyancy gradient in the vortex ring introduces a high instability close to the view plane. This instability is represented in the fluctuation of high and low-velocity regions throughout the outflow. It supports that horizontal roll vortex is a complex non-uniform three-dimensional structure that can occur randomly about the event circumference. The lack of uniformity further supports that the added wall porosity has introduced turbulence through mixing at the initial onset of the event descent. The non-uniform outflow structure along the ground plane presents an opportunity to apply the scaling method developed by Orf et al. (2014).
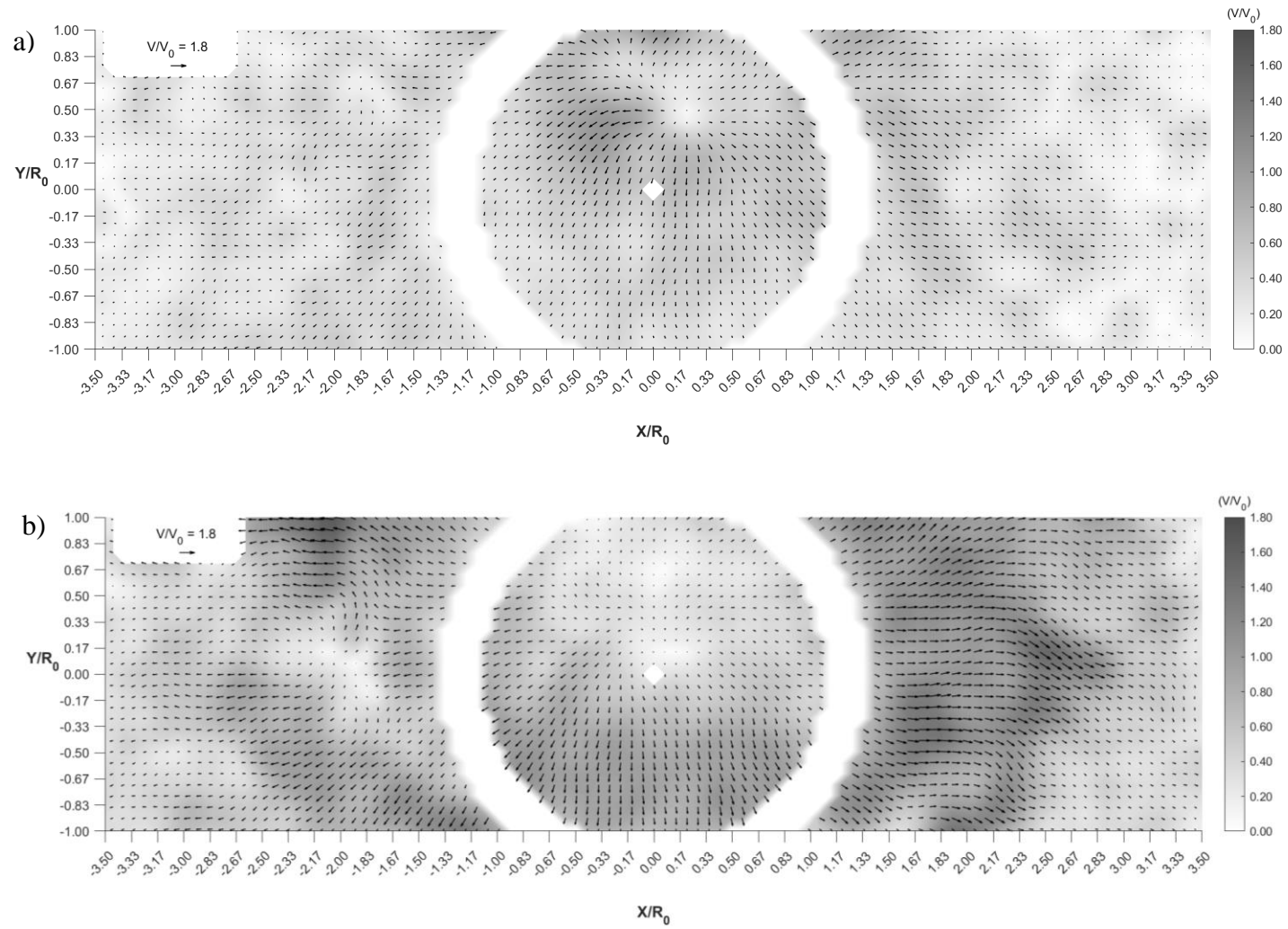
Figure 3-30 - (a) Scaled horizontal velocity vectors and contour fields (V/V₀) at t/T₀ = 4.05, (b) at t/T₀ = 5.95
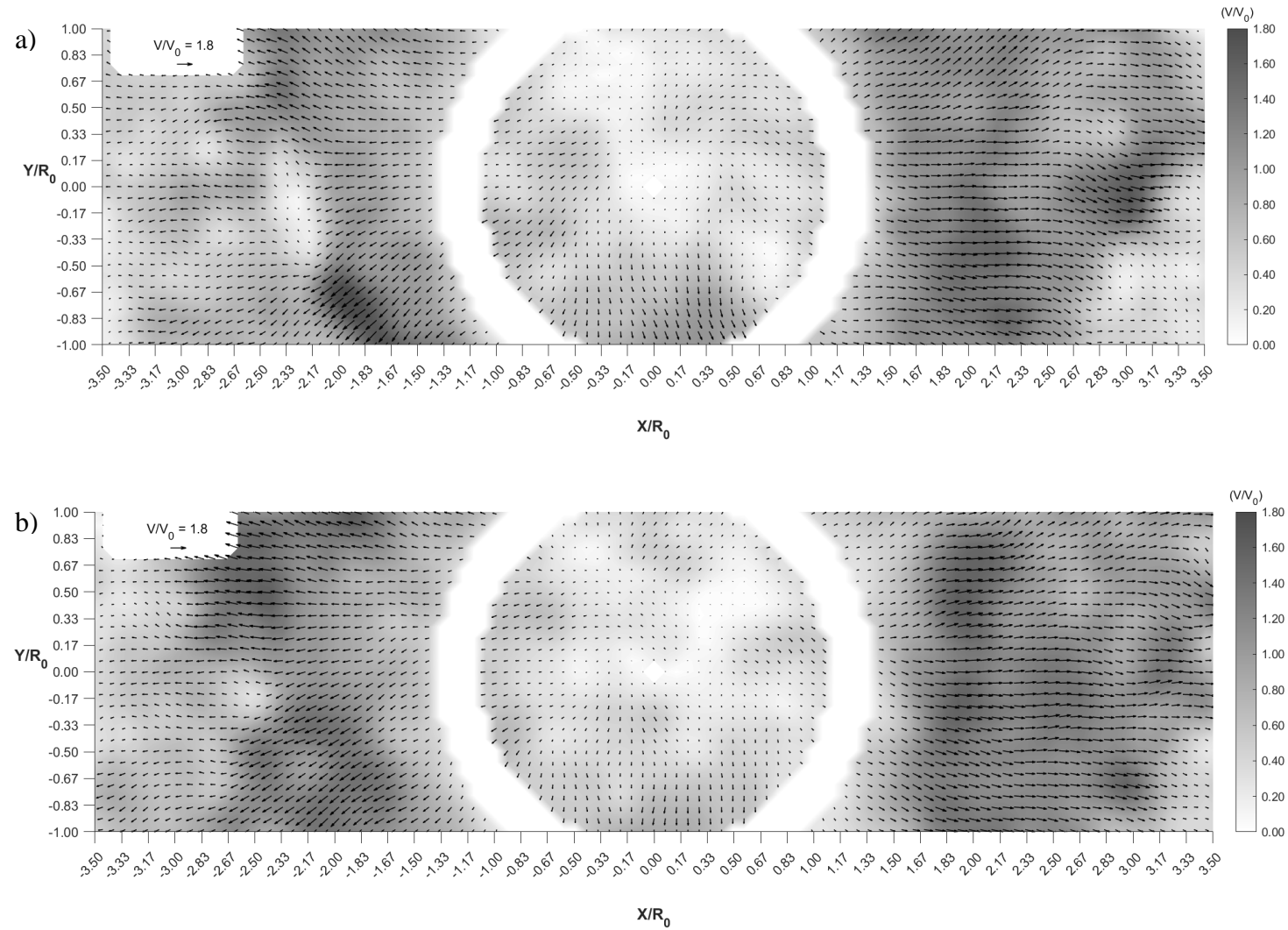
Figure 3-31 - (a) Scaled horizontal velocity vectors and contour fields (V/V$_0$) at t/T$_0$ = 6.76, (b) at t/T$_0$ = 7.30

High-resolution Cooling Source-based CM1 (Bryan, 2000) numerical simulation, with precipitation and wind-shear, of downbursts described in Orf et al. (2012, 2014) and Oreskovic (2016) showed asymmetry in the distribution of velocity about the periphery of a downburst outflow. They attributed the asymmetry resulting from turbulence induced by the complex interaction of atmospheric conditions such as ambient wind conditions, precipitation, etc. Analysis of the circumferential distribution of the maximum, average, and minimum radial velocity magnitude was used to analyze these high-resolution numerical events as an axisymmetric equivalent. A good agreement between this circumferential analysis and axisymmetric simulations was found. Orf et al. 2014 and Oreskovic (2016) expanded the study to include finding a scaling factor (equation 3-5), using linear regression, that can be applied to the average circumferential velocity profile of a downburst (at radii close to the peak radial velocity) to predict the peak radial velocity. A scaling factor of 1.984 was found for the particular CM1 model discussed.

$$u_{scaled} = 1.984 u_{ave} \qquad \text{(3-5)}$$

The same analysis was applied here to investigate the possibility of developing a similar scaling factor for dense release experiments. The use of a multiplier on the circumferential average helps establish a set of normalized curves that can account for the inherent horizontal spatial variability in the distribution of velocity about natural downbursts. This will help improve the current wind engineering models in predicting the location and magnitude of the peak velocity in downburst events in the near-surface region, all of which combined is of importance for estimating wind loading of structures. The goal is to complement the work of Orf et al. (2014) and Oreskovic (2016) by providing an additional set of data from laboratory events that encompass the primary physical process of environmental downburst outflows. With this in mind, two sets of constant multipliers were investigated to satisfy equations 3-6 and 3-7:

$$u_{scaled} = k_1 u_{avg} \qquad \text{3-6}$$

$$u_{scaled} = u_{avg} + k_2 u_{rms} \qquad \text{3-7}$$

Only a segment of the circumference (C_x) was captured in the field of view (Figure 3-32). Radial velocity was interpolated along with the LH and RH parts of C_x as a function of the radius at different times and as a function of time at different radii (Figure 3-33 and Figure 3-34).
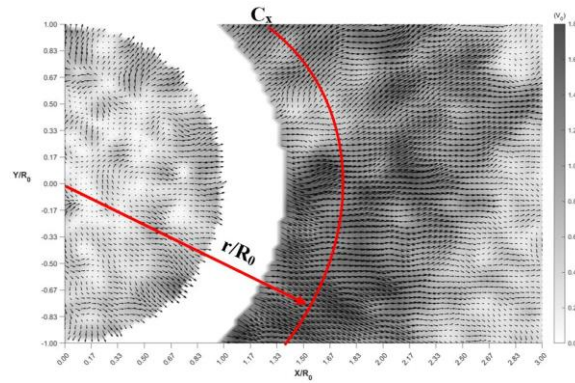
Figure 3-32 – Diagram of the limitation of the circumference segments
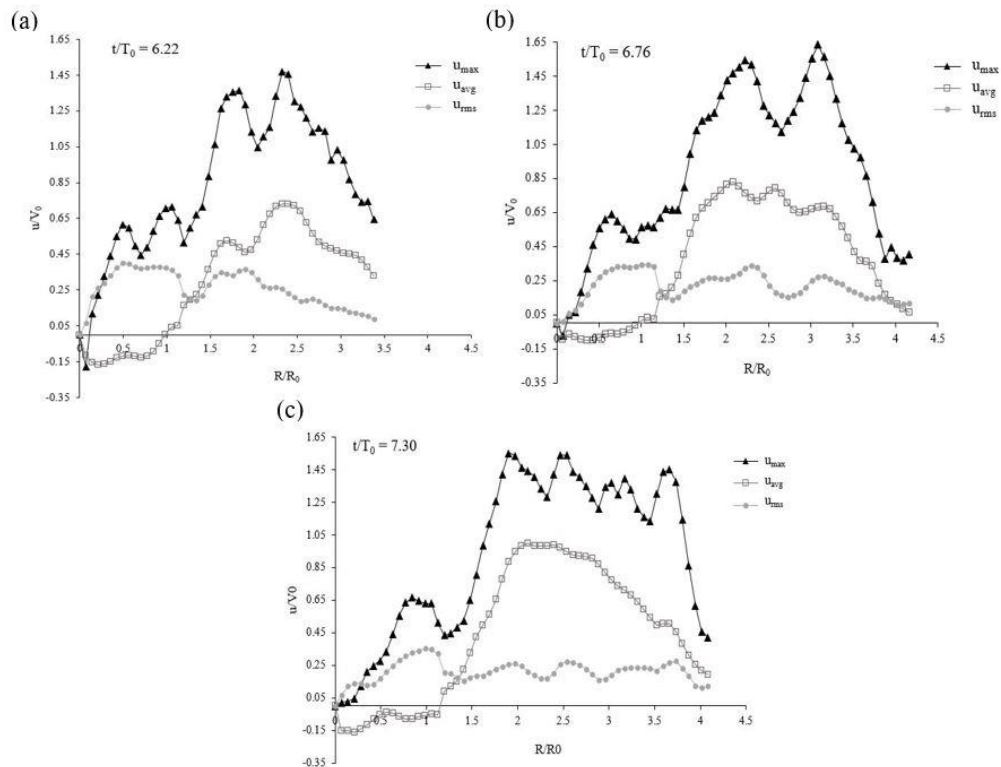
Figure 3-33 – The maximum radial velocity (u_{max}), average velocity (u_{ave}), and mean fluctuating velocity about the average (u_{rms}) over different radii at (a) $t/T_0 = 6.22$, (b) $t/T_0 = 6.76$, and (c) $t/T_0 = 7.30$

The circumferential maximum, mean, and rms of radial velocity as a function of radius for times (a) $t/T_0 = 6.22$, (b) $t/T_0 = 6.76$, and (c) $t/T_0 = 7.03$ are shown at an above ground level (AGL) at $Z/R_0 = 0.16$ in Figure 3-33. The time history of the circumferential maximum, mean, and rms at different radial positions (d) $R/R_0 = 2.32$, (e) $R/R_0 = 2.75$, and (f) $R/R_0 = 3.28$ is shown in Figure 3-34 a, b, and c respectively.
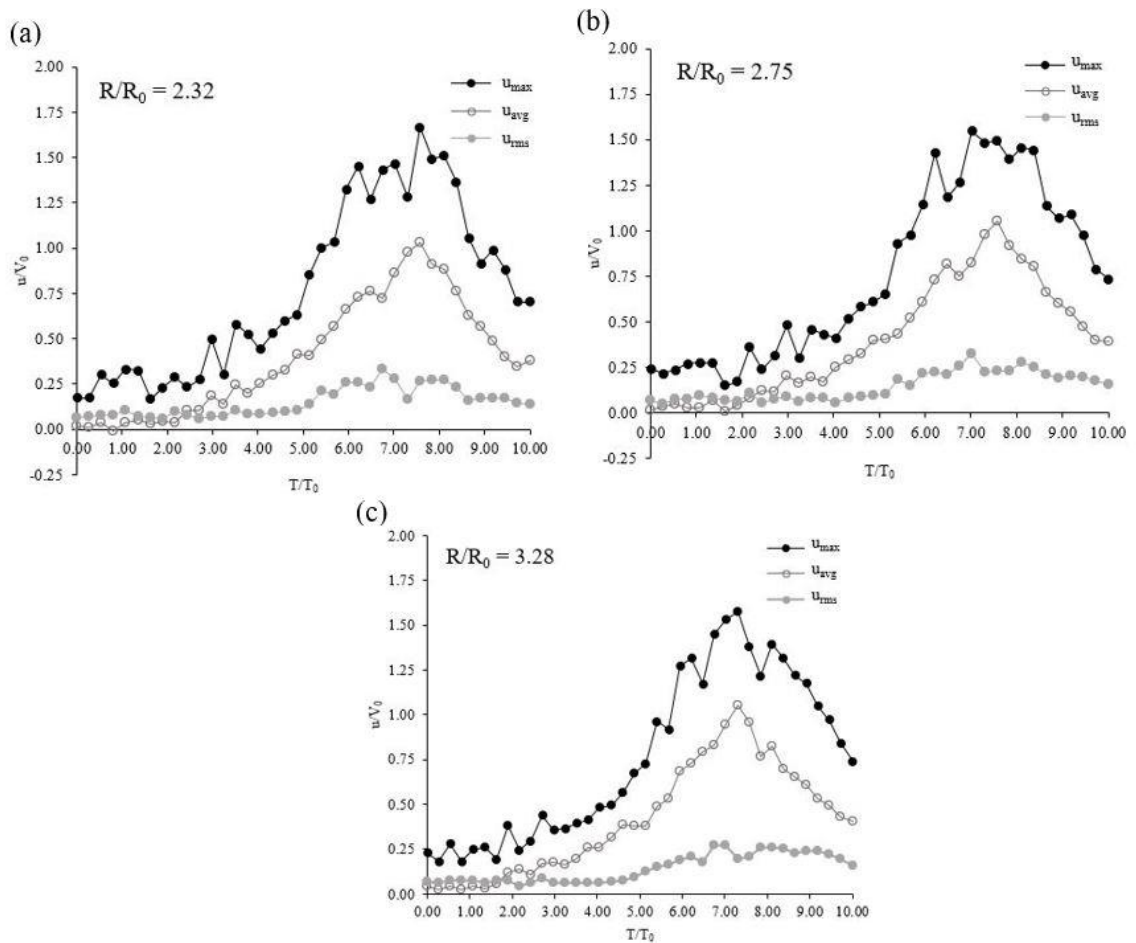
Figure 3-34 - The time history of the maximum radial velocity (u_{max}), average velocity (u_{ave}), and mean fluctuating velocity about the average (u_{rms}) over different radii at (a) $R/R_0 = 2.32$, (b) $R/R_0 = 2.75$, and (c) $R/R_0 = 3.28$

The time history over different radii and the maximum, mean, and RMS values over radii at the specified times provides coverage over the domain in space and time for how velocity is distributed radial. Figure 3-33 a and c and Figure 3-34 a, b, and c, the peak in the average velocity corresponds closely to the peak radial velocity for both time and space. No clear

trend exists in the mean of the fluctuating velocities. As the average about each circumference peaks as the maximum values peaks both over space and time, a constant multiplier can be used on the average to predict the peak. The region $1.3 < R/R_0 > 3.5$ was selected as the area of interest for finding a multiplier as the high outflow velocities are expected to occur in this region.
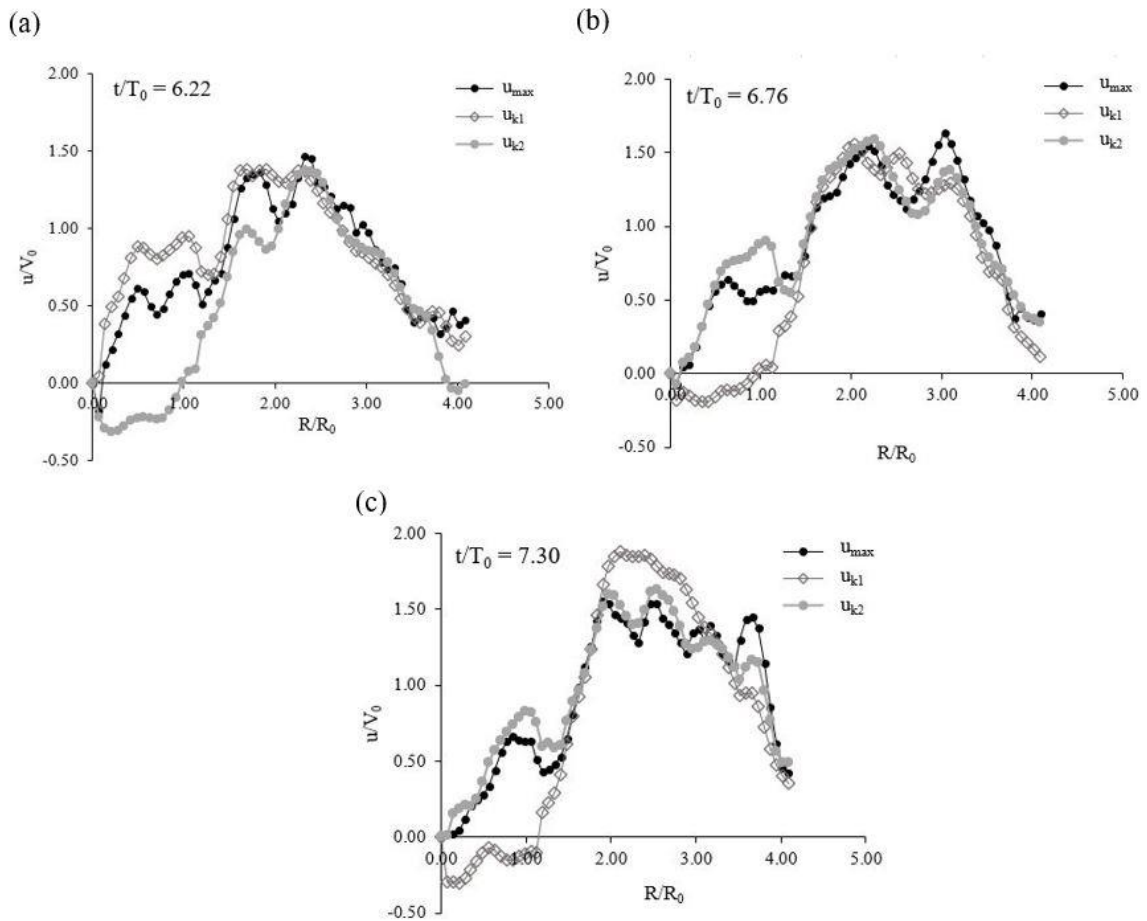
Figure 3-35 – The maximum radial velocity (u_{max}) with the scaled velocities by k_1 (u_{k1}), and k_2 (uk1) over different radii at (a) $t/T_0 = 6.22$, (b) $t/T_0 = 6.76$, and (c) $t/T_0 = 7.30$

Using equations 4.2 and 4.3, the constants k_1 and k_2 were solved and their respective values derived from the data in Figure 3-33 with a range of radii between $1.3 < R/R_0 > 3.5$ and time about the peak radial velocity between $4 < t/T_0 < 8$. Linear regression was performed to find values for k_1 and k_2 that best fit the spatial and temporal data such that, in general, the peak radial velocity is best predicted in times and radial regions close to the peak radial

velocity. Applying this method yielded $k_1 = 1.88$ and $k_2 = 2.51$. When applied to the region and time of the maximum, these two values provide a fit with an R^2 value of 0.981. Figure 3-35 shows the resulting curves when equations 4.2 and 4.3 are used to predict the peak radial velocity as a function of the radius at (a) $t/T0 = 6.22$, (b) $t/T_0 = 6.76$, and (c) $t/T_0 = 7.03$ and for all times for the event release at radii of (d) $R/R_0 = 2.32$, (e) $R/R_0 = 2.75$, and (f) $R/R_0 = 3.28$, incorporating the RMS about the circumference provides a better prediction of the peak radial velocity in both space and time about the region of the maximum. Overall, applying the values of k_1 and k_2 underestimate the peaks at $t/T_0 = 6.22$ and $t/T_0 = 6.76$ and radii either side of the maximum at $R/R_0 = 1.3$ and $R/R_0 = 3.50$. The underestimation limits the scope to radial locations within $1.3 < R/R_0 > 3.5$. Also, no smoothing was applied to the data to maintain the transience observed in the outflow.
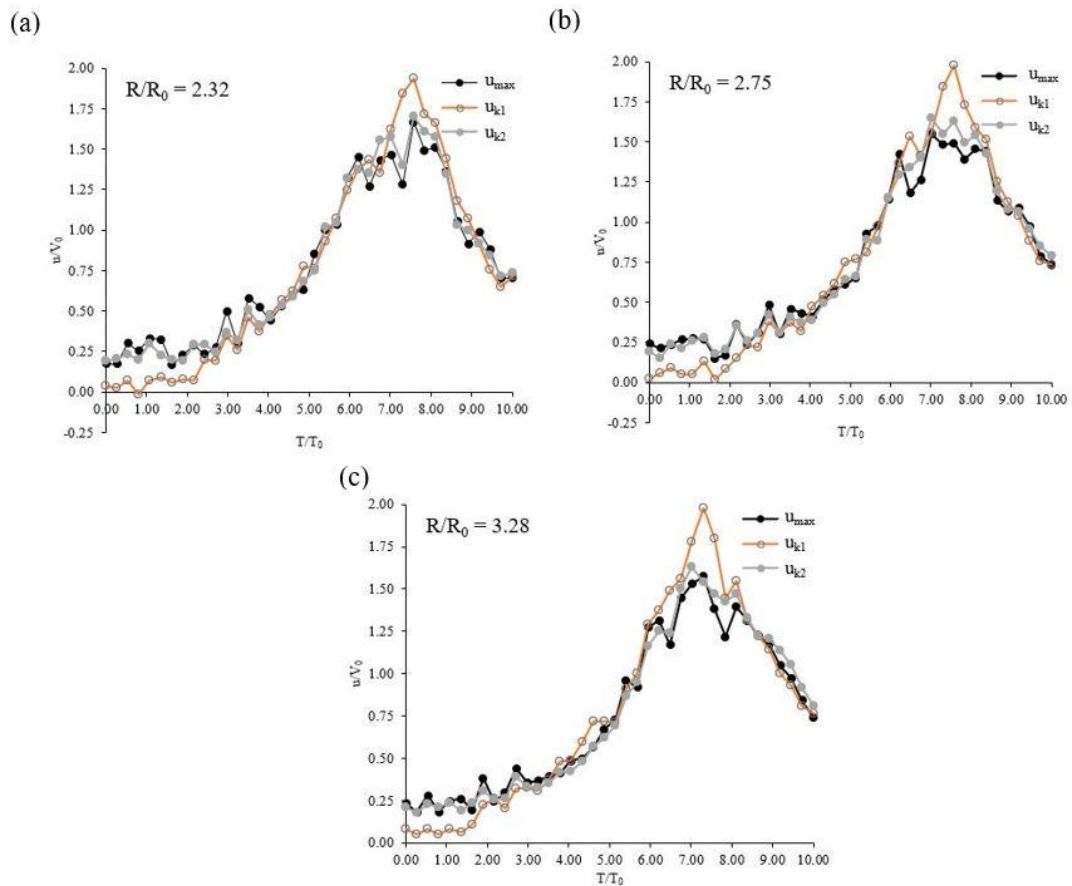
Figure 3-36 - The time history of the maximum radial velocity (u_{max} with the scaled velocities by k_1 (u_{k1}), and $k2$ (u_{k2}) over different radii at (a) $R/R_0 = 2.32$, (b) $R/R_0 = 2.75$, and (c) $R/R_0 = 3.28$

$k_1 = 1.88$ is a lower constant multiplier than what was proposed by Orf et al. (2014) and Oreskovic (2016) at 1.936. Orf et al. (2014) considered the constant factored as a function of radius over times t = 3588 s, t = 3606, and t = 3628 in the region from 0 < R/R$_0$ >2, which encompassed the location in the maximum radial velocity occurs. Interference from the cylinder prevented this region from being included in this analysis. The value for k_1 could be higher if data from this region were included. Using the RMS in conjunction with the average radial velocity results in a better fit, and the value of $k_2 = 2.5$ satisfies the prediction of the peak radial velocity well in both space (Figure 3-35) and time (Figure 3-36). The RMS represents how far, on average, the velocities are from the average velocity. The peak radial velocity in each segment (C_x) over space and time is included in these fluctuations. A notable increase in the u_{rms} can be seen in Figure 3-33 (a) at R/R$_0$ = 2.5, (b) at R/R$_0$ = 3.2 and (c) at R/R$_0$ = 2 and in Figure 3-34 (b) and (c) at t/T$_0$ = 7 all corresponding close to the peak radial velocity recorded in each case. As this is the case, the peaks in u_{rms} better follow the radial velocity peaks over the average. Scaling by k_2 is a more effective approach than simply using the average.

The horizontal profiles as a function of radius scaled by k_2 at different times of Figure 3-30 are plotted against the empirical function of Holmes and Oliver (2000). The empirical function captures the profile that downbursts recorded from NIMROD follow and represents the general shape of the velocity in horizontal of natural downburst outflows.
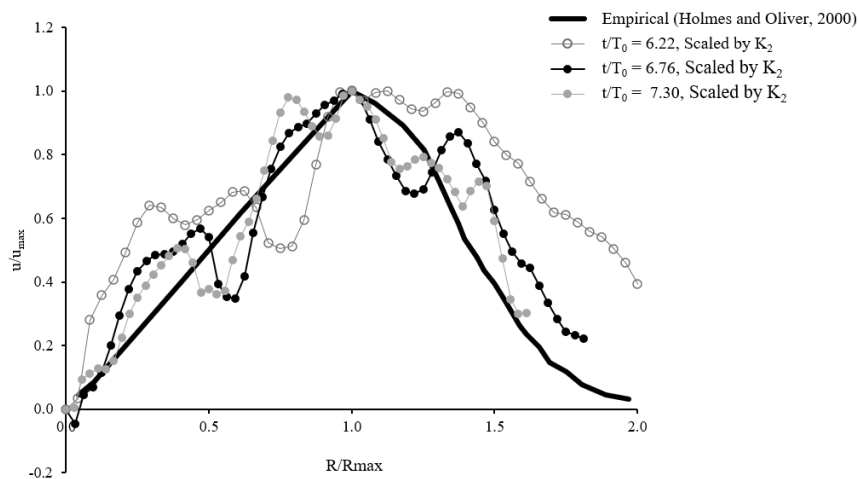
Figure 3-37 – Normalized circumferentially-averaged radial velocity Scaled by k_2 with the empirical model from Holmes and Oliver (2000)

Applying equation 3.4 with the scaling factor of $k_2 = 2.5$ to radial profiles maintains the general shape of a downburst outflow as captured by Homes and Oliver (2000). The agreement follows the trend up to and after the maximum. However, the analysis performed excluded the maximum radial velocity region, accounting for the deviation seen. Therefore, the values of k1 and k2 from this analysis serve as a general approximation that can be applied to the instantaneous velocity vector fields in the horizontal orientation plane of dense fluid release experiments to obtain the potential peak maximum radial velocity.

3.6   Summary

PIV captures of the vertical and horizontal outflow velocity vector fields using the new release cylinder proved that the outflow is comparable to past work. Eight single release experiments were conducted with the cylinder centred in the field of view for resolving the vertical cross-plane velocity vector fields of a stationary downburst. Of the eight experiments, only two were found suitable for analysis: Single DB A and B. Release Single DB A was found to be weaker than Single DB B as significant leaking from the release cylinder was found. A comparison of the total domain velocity and radial velocity to the outflow of the solid wall release experiments of Alahyari (1995) did not find any measurable effect from the newly added sidewall slots. Break-up of the outflow's leading boundary prior to impacting the ground plane lead to contractions in the vertical profiles of radial velocity from the new cylinder compared to other experimental techniques. Vortex tracking using the lambda 2 (λ_2) criterion proved to provide a new way to scale downbursts outflow. Scaling by the maximum time was found to provide a closer fit after the vortex reaches the ground than using the min-height time as in Chowdhury (2018).

In addition to a summary of the first phase of this study above, the following major conclusions were found:

1. Symmetry in the outflow based on a percent difference velocity magnitude, radial location, and height above the ground found that the new cylinder's outflow was symmetrical within a margin of acceptance. The velocity magnitude varied from

the left-hand side to the right-hand side by 8.3%, radial location by 3 % and height by 50%. The height difference was consistent in time about the maximum radial velocity and was attributed to a possible setup error.

2. The wall effect from adding the wall gates was not measurable, given the current data set. The maximum domain velocity and radial velocity from the new release cylinder of the release Single DB B were found to match with data available from Alahyari (1995). The release of Single DB A had a weaker outflow and provided no comparison to Single DB B or Alahyari's (1995) outflow. The cylinder release height was $H/R_0 = 0.09$ lower than Alahyari's (1995), which should have increased the near-surface velocity in conjunction with the newly added gates' lower wall effect. As the velocities compared well, it was concluded that the wall gates reduced the overall strength of the outflow by introducing initial mixing before descending. Further investigation is needed to understand how the wall gates affect the outflow.

3. The outflow velocities recorded were weaker overall compared to past dense fluid release experiments with a peak radial velocity of $V/V_0 = 2.19$ occurring at a radial location close to $X/R_0 = 1$ from the event centreline. It was noted that the current PIV system's limited spatial and temporal resolution might have put the maximum outside the data set presented here. It was also concluded that as the flow is complicated turbulent and 3-D, the peak velocity could be out of the view plane. Adding additional release to the data is recommended to establish the actual peak expected.

4. The vertical profiles in the vertical were found to match the profiles of past experiments and field data. A noticeable trend with PIV data was found in the near ground portion of the profiles when compared to the PIV IJ model of Zhang et al. (2013). This suggested that the limited resolution of PIV experiments in the near-surface region affects the outflow profile definition. A contraction in the upper portion of the profile was found and resulted from the breakage of the descending front edge prior to impacting the ground. Studies focusing on the near region of the outflow for PIV-based captures are recommended better to understand the effect of capture resolution on near-surface profiles.

5. An acceleration threshold of $d(V/V_0)/dt = 9.2$ was found to define the horizontal descent and radial propagation of the Single DB B release events well against the PLIF data of Babaei (2018). A lower value of $d(V/V_0)/dt = 0.84$ was needed to release Single DB A as its outflow was weaker than Single DB B. Further single release experiments are needed to define the threshold acceleration value better.

6. Tracking the core of the horizontal roll vortex using the λ_2 criterion proved successful using a threshold value of $\delta_\lambda = -40 \pm 5\%$ for this study. Scaling the vortex trajectory by the time of the minimum vortex height or the time of the maximum radial velocity showed that the vortex path of the dense fluid releases matched well with the high Re number transient jet cases from Chowdhury (2018). The lowest horizontal (Z/X_0) point in the vortex core's travel for the two dense fluid releases of this study coordinated with the second-highest velocity magnitude in the near-surface outflow. Tracking the trajectory of the horizontal roll vortex core using the core diameter (Dv) to core centre height (Dz) aspect ratio provided preliminary experimental support to the conclusion by Vermeire (2011a) that using modelling techniques that simulate the buoyancy gradient is vital in modelling the structure of the outflow especially after the time of the maximum radial velocity.

7. The horizontal vector field captured at the height of $Z/X_0 = 0.16$ (7 *mm* AGL) confirmed that the right-hand side of the single releases from the new cylinder design had a higher outflow volume than the left-hand side. As this was the case in combination with the fact that all data was instantaneous, a circumferential averaging analysis was performed following Orf et al. (2014). The averaging considered the maximum, average, and average fluctuation about the mean velocities over circumferential arc segments (C_x) at different times and radial positions. Two scaling factors were explored, one focusing on using only the circumferential mean (k_1) and a second on the mean plus a scaled RMS value (k_2), following the findings of Oreskovic (2016). Oreskovic (2016) found that using a scaling factor of 1.984 with the circumferential mean velocity in the radial region close to the expected maximum peak radial velocity could estimate the peak in non-axis-symmetric high-resolution CS downburst simulations. The outflow of

the new cylinder design used in this study found that using the mean fluctuations scaled by a factor of 2.5 plus the circumferential average produced a better estimation of the maximum value in the outflow in the region beyond the radial location of the maximum. The region encompassing the maximum could not be studied due to the release cylinder's interference in the velocity vector fields. Adding a low reflectivity coating to the cylinder bottom was recommended to enable the maximum region to be included.

3.7   References

Alahyari, A.A., 1995. Dynamics of laboratory simulated microbursts. Ph.D. Dissertation, University of Minnesota, USA.

Alahyari, A.A., and Longmire, E.K., 1994. Particle image velocimetry in a variable density flow: application to a dynamically evolving microburst. Exp. Fluids, 17, 434-440.

Babaei, R., 2018. Experimental simulation of density-driven thunderstorm downbursts. MESc. Dissertation, The University of Western Ontario, Canada.

Bryan G.H., Fritsch J.M., 2002. A benchmark simulation for moist hydrostatic numerical models. Monthly Weather Review 130, 2917-2928.

Chen, Q., Zhang, Q., Qi, M., Wang, X., 2015. Comparison of vortex identification criteria for planer velocity fields. Phys. Of Fluids 27, 085101.

Chowdhury, J., 2018. Transient analysis of full scale and experimental downburst flows. MESc. Dissertation, The University of Western Ontario, Canada.

Fujita, T.T., 1979. Objectives, operation, and results of project NIMROD. 11th Conf. on Severe Local Storms, Kansas City, American Met. Soc., 259-266.

Fujita T.T., 1985. The downburst microburst and macroburst. The University of Chicago, Department of Geophysical Sciences, 128.

Geerts, B. (2001). Estimating downburst-related maximum surface wind speeds by means of proximity soundings in New South Wales, Australia. Weather Forecast. 16, 261–269.

Holmes, J.D., Oliver, SE., 2000. An empirical model of a downburst. Eng. Struct. 22, 9, 1167-1172.

Hjelmfelt, M.R., 1987. The microburst of 22 June 1982 in JAWS. J. Atmos. Sci. 44, 1646-1665.

Hjelmfelt M. R., 1988. Structure and life cycle of microburst outflows observed in Colorado. Journal of Applied Meteorology 27, 900-927.

Jeong, J., Hussain, F., 1995. On the identification of a vortex. J. Fluid Mech. 285, 69.

Lundgren, T.S., Yao J., Mansour, N.N., 1992. Microburst modelling and scaling. J. Fluid Mech, 239, 461-488.

Oreskovic, C., 2016. Numerical Investigation of full-scale thunderstorm downbursts: a parametric study and comparison to meteorological model. MESc. Dissertation, The University of Western Ontario, Canada.

Orf, L.G., Oreskovic, C., Savory, E., Kantor, E., 2014. Circumferential analysis of a simulated three dimensional downburst-producing thunderstorm outflow. J. Wind Eng. Ind. Aerodyn. 135, 182-190.

Orwig, K. D., and Schroeder, J. L., 2007. Near-surface wind characteristics of extreme thunderstorm outflows. J. Wind Eng. Indus. Aerodyn. 95, 565–584.

Wakimoto, R. M., 1982. The life cycle of thunderstorm gust fronts as viewed with Doppler radar and Rawinsonde data. Mon. Weather Rev. 110, 1060–1082.

Jeong, J., & Hussain, F., 1995. On the identification of a vortex. J. of Fluid Mechanics, 285, 69-94.

Porto, J., 2015. Numerical modelling of density-driven downbursts. Intern Report, The University of Western Ontario, Canada.

Roberto, M., Oreskovic, C., Porto, J., Savory, E., 2014. Unsteady RANS modelling of density driven experimental thunderstorm downbursts. In: 25th Canadian Congress of Applied Mechanics, London, Canada, 4 June.

Solari, G., 2020. Thunderstorm downbursts and wind loading of structures: Progress and Prospect. Front. Built Environ. 6, 63.

Vermeire, B.C., Orf, L.G., Savory, E., 2011a. Improved modeling of downburst outflows for wind engineering applications using a cooling source approach. J. Wind Eng. Ind. Aerodyn. 99, 8, 801–814.

Vermeire, B.C., Orf, L.G., Savory, E., 2011b. A parametric study of downburst line near-surface outflows. J. Wind Eng. Ind. Aerodyn. 99, 4, 226–238.

Vermeire, B.C., 2010. Numerical modeling of thunderstorm downbursts and downburst lines. MESc. Dissertation, The University of Western Ontario, Canada.

Wood, G.S, Kwok, K. C.S., Motteram, N.A., Fletcher, D.F., 2001. Physical and numerical modelling of thunderstorm downbursts. J. of Wind Eng. and Ind. Aerodyn., 89, 535-552.

Yao, J., Lundgren, T.S., 1996. Experimental investigations of microbursts. Experiments in

Fluids. 21, 17-25.

Zhang, Y., Hu, H., Sarkar, P. P., 2013. Modelling of microburst outflows using impinging jet and cooling source approaches and their comparison. Eng. Struct. 56, 779-793.

Chapter 4

4 Particle Image Velocimetry (PIV) Study of Downburst Line Near-surface Outflows

Chapter 4 introduces the first experimental data set of downburst line simulations based on two event dense fluid release experiments. Two event-centre-to-event-centre distances of $X/R_0 = 3.64$ and $X/R_0 = 6.14$ with three different release timing differences of $\Delta T = 0.235$, $\Delta T = 0.37$, and $\Delta T = 0.71$ are used .Two plane orientations in the vertical (one in the length of the events and one in the depth of the events) were considered and found that maximum radial velocity in the length of releases was unaffected by the temporal and spatial variation used in this study. The radial extent of regions of scaled EF velocity regions in the outflow depth was investigated in the outflow width's horizontal plane. The shortest time and closes distances caused the greatest radial extent of scaled EF velocity regions. The radial extent of these regions was considered only in the horizontal plane located at the approximant height of the maximum radial velocity at an event release time separation of zero between the minimum and maximum separation distances. The chapter concludes by looking at how event spacing and timing impact the horizontal vortex core trajectory in the interaction regions.

4.1 Effect of Spatial and Temporal Variation on the location of the Maximum Radial Velocity

The release system detailed in Babaei's (2018) work and Chapter 3 was expanded to study the near-surface flow fields of downburst lines. A planner analysis in the release outflow's length and depth is used to investigate the effect of spatial and temporal variation between two simultaneous downburst releases. The objective was to create a first experimental model for the wind fields of downburst line events according to the numerical observations of Orf et al. (1996) and Vermeire et al. (2011a,b).

The data from the Joint Airport Weather Studies (JAWS) (McCarthy et al. 1982) and the Classify Locate and Avoid Wind Shear (CLAWS) (McCarthy and Wilson 1986) observed

that up to 1/8th of downburst events could be classified downburst lines. Though this is a relatively low frequency compared to an isolated downburst event, the damage footprint can be much larger, approximately 150 km^2, in comparison to isolated downburst events (roughly 15 km^2) (Hjelmfelt, 1988). This increases the probability of infrastructure and aircraft being subjected to damaging wind loads (Oliver et al. 2000). The numerical work of Orf et al. (1996) showed that interaction between the outflows of downbursts within downburst lines could create violent near-surface wind fields that are much more different than that of an isolated downburst event. Vermeire et al. (2011a, b) performed a parametric study on the outflow of two event-based downburst lines and found that the hazard bearing regions equivalent to EF1 to EF2 wind speeds (redefined to EF_+ to indicate the non-association with tornadic damage) increased in the outflow depth of downburst lines and increased hazardous wind speeds up to 1.55 times that of a single event.

The location of the maximum horizontal (radial) velocity (u) in both the length and depth of the outflow in two event-based downburst lines is considered first. Figure 1-17 provides a visual overview as to how downburst line event length and width are defined based on the definition proposed by Hjelmfelt (1988). As described in section 2.4.2, two event-based releases observed in the vertical and horizontal planes were performed at two separation distances and three release time differences (ΔT) (Table 2-3) with the attempt to model the most hazardous case in Vermeire et al. (2011a,b) and the Soliton like outflows from Orf et al. (1996). The highest wind speed amplification (defined as V_{max}/V_{base}) was found to be at an event centre-to-centre distance of 2 km, with an event-to-event release time delay of 30 s. The first part of this study considers how the maximum horizontal velocity in the vertical plane of the length of downburst line events is affected by temporal and spatial variation. Figure 4-1 (a) shows the vertical plane's cylinder orientation covering the line event length at the minimum release distance and (b) at the maximum release distance.

a)

b)
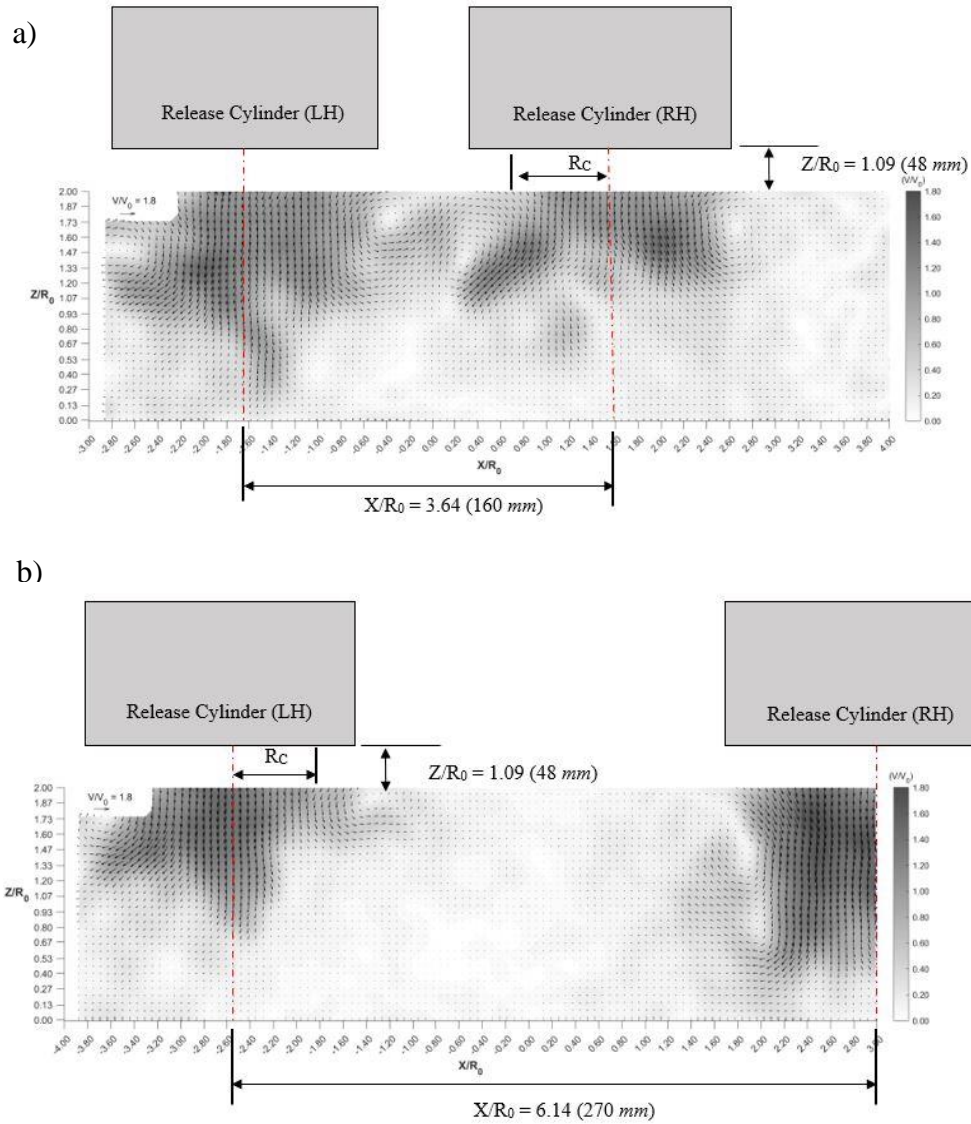
Figure 4-1 – a) The release cylinder locations for the downburst line simulations of X_d (R_0) = 3.64, and b) at X_d (R_0) = 6.14

The separation time (ΔT) is defined as the delay in releasing the second cylinder after the first cylinder was initiated. The right-hand cylinder was the first to release in each experiment and was the cylinder that was moved for each separation distance.

Of the cases defined by Orf et al. (1996) and later expanded upon by Vermeire et al. (2011a, b), only the complex interacting or Soliton like noninteracting (called here as discrete) downburst line cases could be experimentally performed due to the limitations discussed

in section 2.4.2. Coalescent interactions between two downbursts occurring at or near to the same time produce the most significant near-surface horizontal wind speeds (Orf et al., 1996). In the coalescent cases, the interaction region in the depth of a downburst line forces the outflow to swell and push out in strong horizontal roll vortices with increased outflow depth. The same behaviour is present in complex interacting downburst lines but lessened as the horizontal roll vortices have space to develop and oppose each other in the interaction region. This study will not capture the most hazardous downburst line condition but will show the closest event separation distances and the smallest time differences result in the highest near-surface horizontal outflow velocities. Five releases were performed for each separation, distance and time. The best vector field, defined by the least number of interpolated vectors, was selected for analysis. As described in section 2.4, issues impacted the quality of the images and imposed a limitation on the quality of data that could be obtained. The main challenge was collecting PIV images that had as little cross-plane motion as possible. Avoiding cross-plane motion proved challenging as flow in the interaction region was predominantly out-of-plane and turbulent. Therefore, the variation in the outflow of each condition was not captured. The location and magnitude of the outflow velocities are based on instantaneous realizations of turbulent flows and subject to the limitation imposed by the variation present in each case.

Figure 4-2 (a) captures the vertical outflow of the smallest separation distance of $X_d/R_0 = 3.64$ at the smallest timing difference of $\Delta T = 0.235$. Unfortunately, the outflow velocities recorded in the vertical plane of the outflow were weak. The other attempts at the same release distance and time were of low quality to use. The flow about the sidewall gates may have included a flow field that could add significate mixing in the initial stages of the release reducing the overall outflow strength in the descending downbursts. Further investigation is needed to determine the exact cause. Figure 4-2 (a) shows the velocity vector field at $t/T_0 = 4.87$, the time when both events reach the ground. No significant horizontal velocities are seen in the region of $Z/X_0 = 0.2$ in the length of this close separation distance and timing. This is especially true in the interaction region where the opposing outflows work against forming high horizontal velocities. Progressing in time to $t/T_0 = 6.49$ in Figure 4-2 (b) shows that this remains the case throughout time.

Figure 4-2 - Scaled velocity vectors and contour fields (V/V₀) for ΔT = 0.235, X_d/R_0 = 4.87, (a) t/T₀ = 4.87 and (b) at t/T₀ = 6.49

Figure 4-3 - Scaled velocity vectors and contour fields (V/V$_0$) for ΔT = 0.37, X$_d$/R$_0$ = 4.87, (a) t/T$_0$ = 5.14 and (b) at t/T$_0$ = 7.84
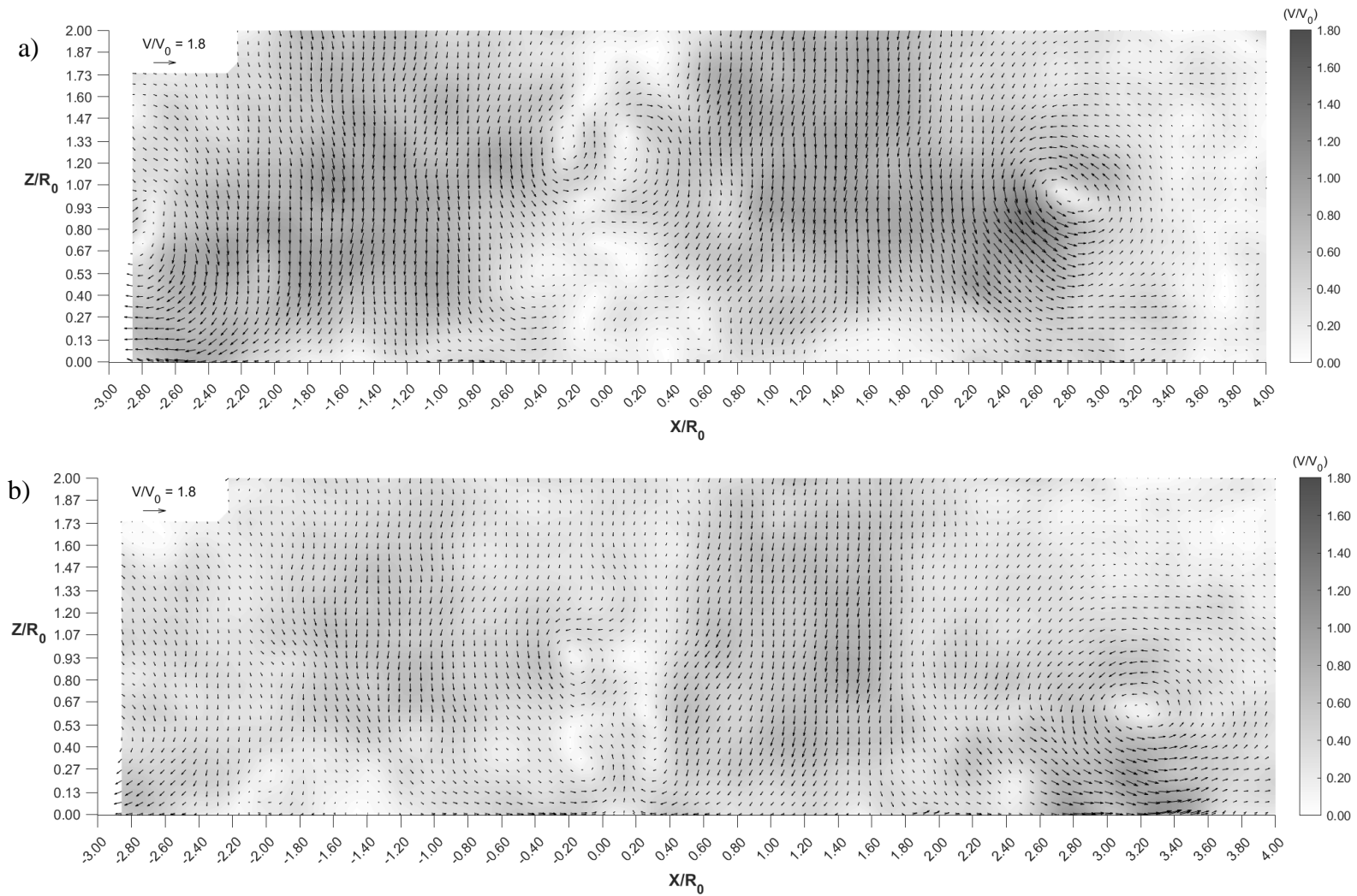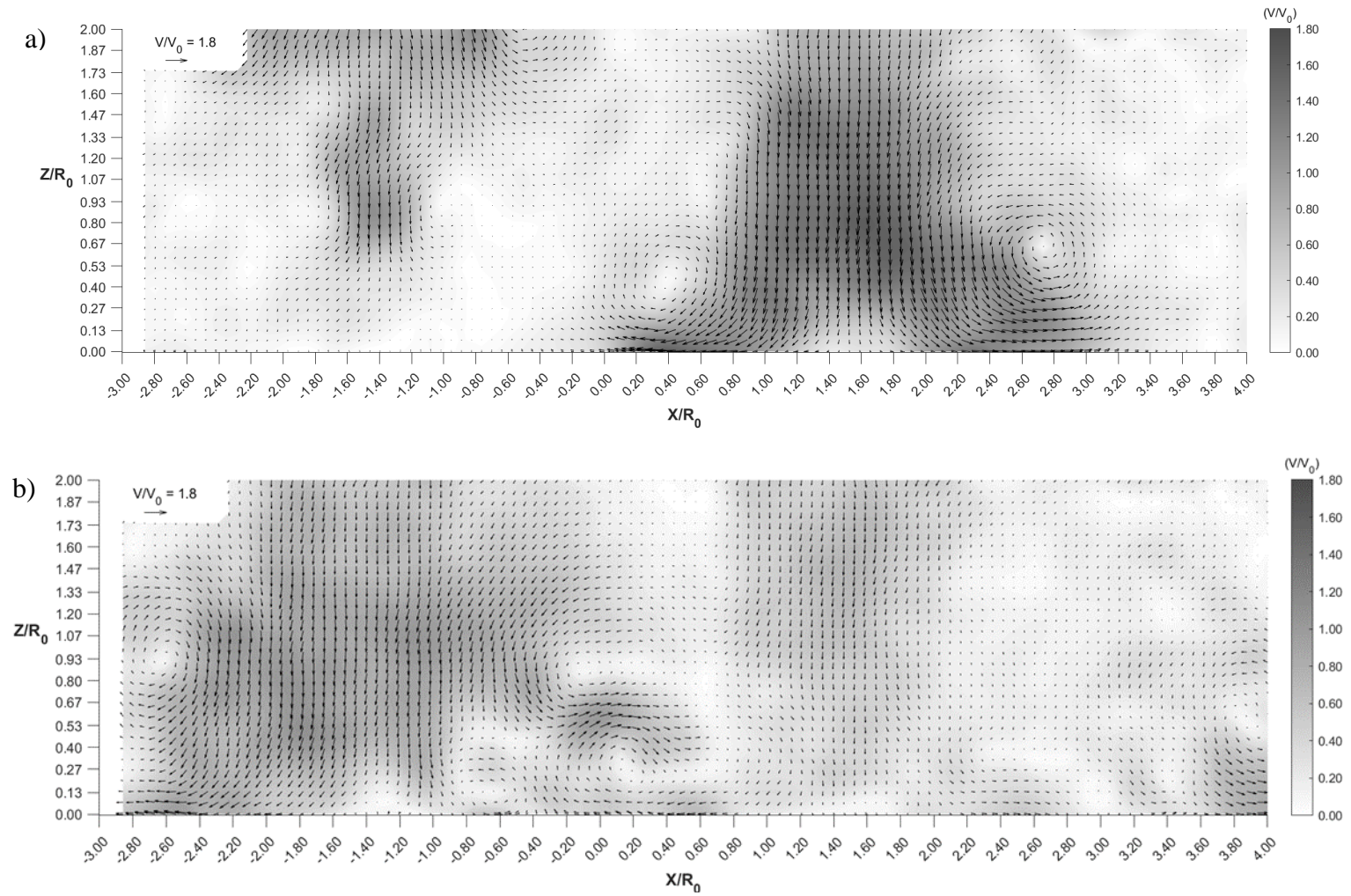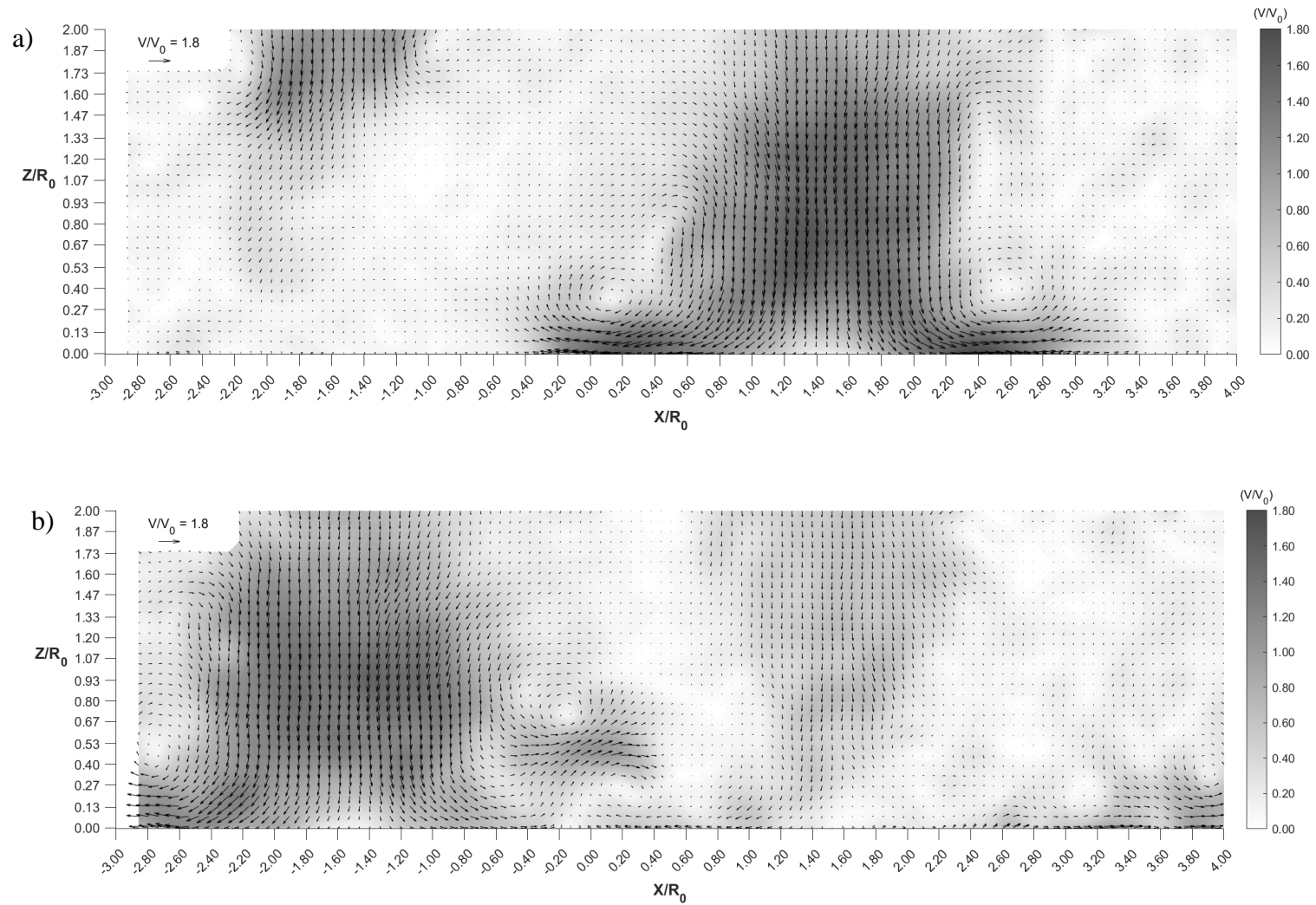
Figure 4-4 - Scaled velocity vectors and contour fields (V/V$_0$) for ΔT = 0.74, X$_d$/R$_0$ = 4.87, (a) t/T$_0$ = 5.14 and (b) at t/T$_0$ = 8.11

With release times greater than zero, in these cases at $\Delta T = 0.37$ and $\Delta T = 0.74$, the right-hand event forms and dissipates much the same a singular event with only the horizontal roll vortex in the interaction region being affected by the outflow of the second release. Figure 4-3 (a) shows the $\Delta T = 0.37$ right-hand event at the time of its respective maximum radial velocity ($t/T_0 = 5.14$) and (b) at the left-hand release's maximum radial velocity ($t/T_0 = 7.84$). Similarly, Figure 4-4 (b) shows the $\Delta T = 0.71$ right-hand event at the time of its respective maximum radial velocity ($t/T_0 = 5.14$) and (b) at the left-hand release's maximum radial velocity ($t/T_0 = 8.11$). The radial location and height of the maximum horizontal velocity remain within the same location as that of a singular event (Table 4-1) for the right-hand release after it impinges for both time differences.

Table 4-1– Summary of the radial and horizontal location of the maximum radial velocity after impingement of the right-hand event

	$X_d/R_0 = 3.64$		$X_d/R_0 = 6.14$		
	$\Delta T = 0.37$	$\Delta T = 0.74$	$\Delta T = 0.24$	$\Delta T = 0.37$	$\Delta T = 0.74$
X/R_0	1.06	1.18	1.20	0.90	1.25
Z/R_0	0.12	0.09	0.12	0.13	0.12
u/V_0	1.82	1.77	1.75	1.73	1.71

Interestingly, the same result is also observed for the left-hand side of the left-hand release after it has impinged on the ground. This result will be discussed further on. The near-ground velocities in the interaction region remain suppressed by the opposing outflow from the adjacent event. The timing difference between $\Delta T = 0.37$ and $\Delta T = 0.74$ is such that the right-had event impinges before the left-hand event reaching the ground. The left-hand event does not impart an influence until after the right-hand events outflow has already formed. Shorter ΔT's that see the left-hand event's outflow reaching the ground near the same time as the right-hand event would see the maximum radial velocity in the interaction

region diminished in the plane of the downburst line events length. The interaction of the horizontal roll vortices is of more interest.

The timing difference most notably impacts the horizontal roll vortex. The shortest timing difference ($\Delta T = 0.235$) shown in Figure 4-2 (b) results in the vortical structure tangling into a singular vortex after $t/T_0 = 6.41$. A more detailed analysis is provided in section 4.3. Increasing the timing difference causes the right-hand right-side horizontal vortex roll to remain close to the ground plane (no vortex lift) as the second events push on top of and against its propagation. Figure 4-3 (b) and Figure 4-4 (b) show the primary horizontal vortex roll of the right-hand event in the interaction region forced to remain close to the near ground region as the primary horizontal roll vortex of the left -hand event falls on top. This interaction causes higher velocities to form further above the ground. Figure 4-5 shows the scaled velocity magnitude (V/V_0) with scaled height (Z/R_0) in the centre of the interaction regions defined as $X/R_0 = 0$ for all three-time separations at the time of the maximum radial velocity of the left-hand side of the left-hand event.
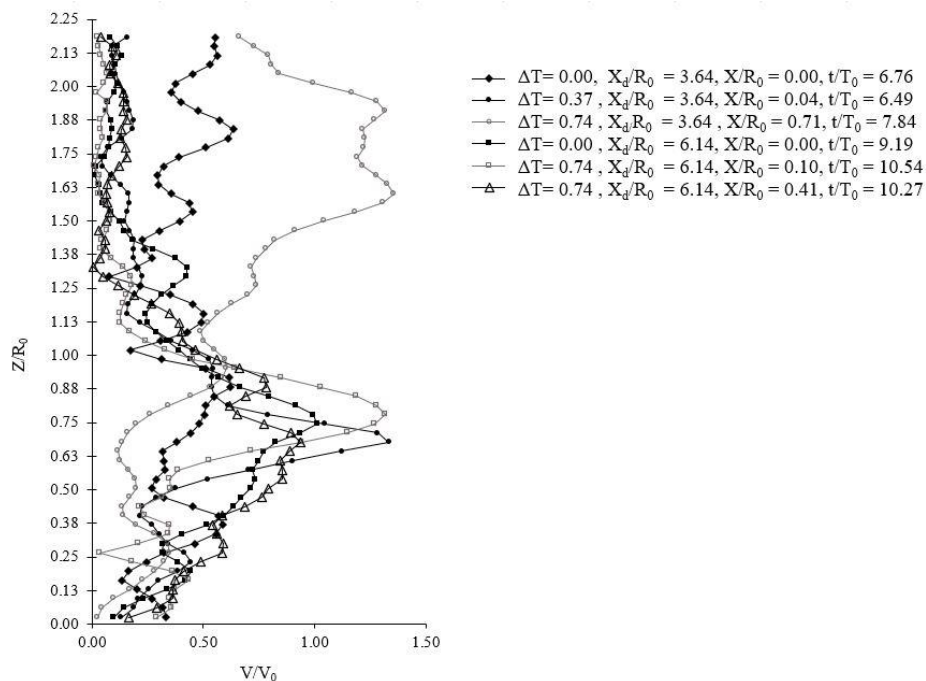
Figure 4-5 – Vertical profiles of velocity through the interaction regions of the vertical length plane of the close ($X_d/R_0 = 3.64$) and far ($X_d/R_0 = 6.14$) separation cases for the different time delays of $\Delta T = 0.24$, $\Delta T = 0.37$, $\Delta T = 0.74$ at location of the highest velocity after collision

High velocities of $V/V_0 = 1$ to $V/V_0 = 1.3$ are seen at heights above $ZR_0 = 0.63$, which (using the DL191 (Yao et al., 1992) scaling) corresponds to speeds of 48 *m/s* at heights of 400 *m*. An increase to the maximum spacing difference of X_d $(R_0) = 6.14$, with the same ΔT separation times, removes much of this effect in the interaction region. At X_d $(R_0) =$ 6.14, the events' distance allows for each event outflow to develop and the horizontal roll vortex to form and dissipate. Figure 4-6 (a) and (b), Figure 4-7 (a) and (b), and Figure 4-8 (a) and (b) capture how the distance allows for enough space such that the outflow of each event produces a weak interaction leading to the Soliton like noninteracting outflows discussed in Orf et al. (1996). Figure 4-6 (a) shows the $\Delta T = 0.24$ case at $t/T_0 = 4.87$, the time where the maximum radial velocity was recorded in the right-hand event, and (b) at $t/T_0 = 6.22$ when the left-hand event maximum radial velocity was recorded. Likewise, for Figure 4-7 (a) and (b) for $\Delta T = 0.37$, and Figure 4-8 (a) and (b) for $\Delta T = 0.71$.

Figure 4-6 - Scaled velocity vectors and contour fields (V/V$_0$) for $\Delta T = 0.24$, X$_d$/R$_0$ = 6.14, (a) t/T$_0$ = 4.87 and (b) at t/T$_0$ = 6.22
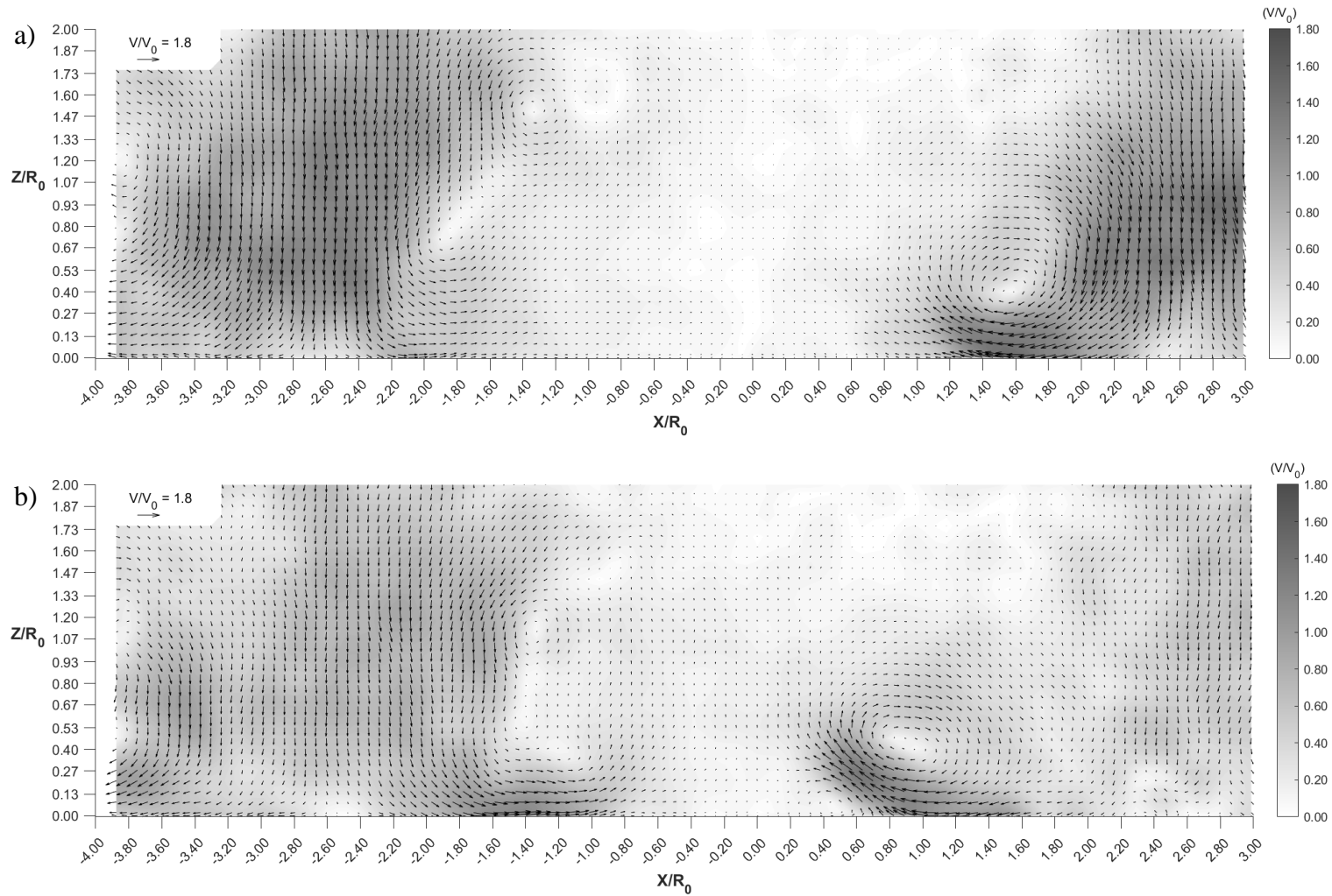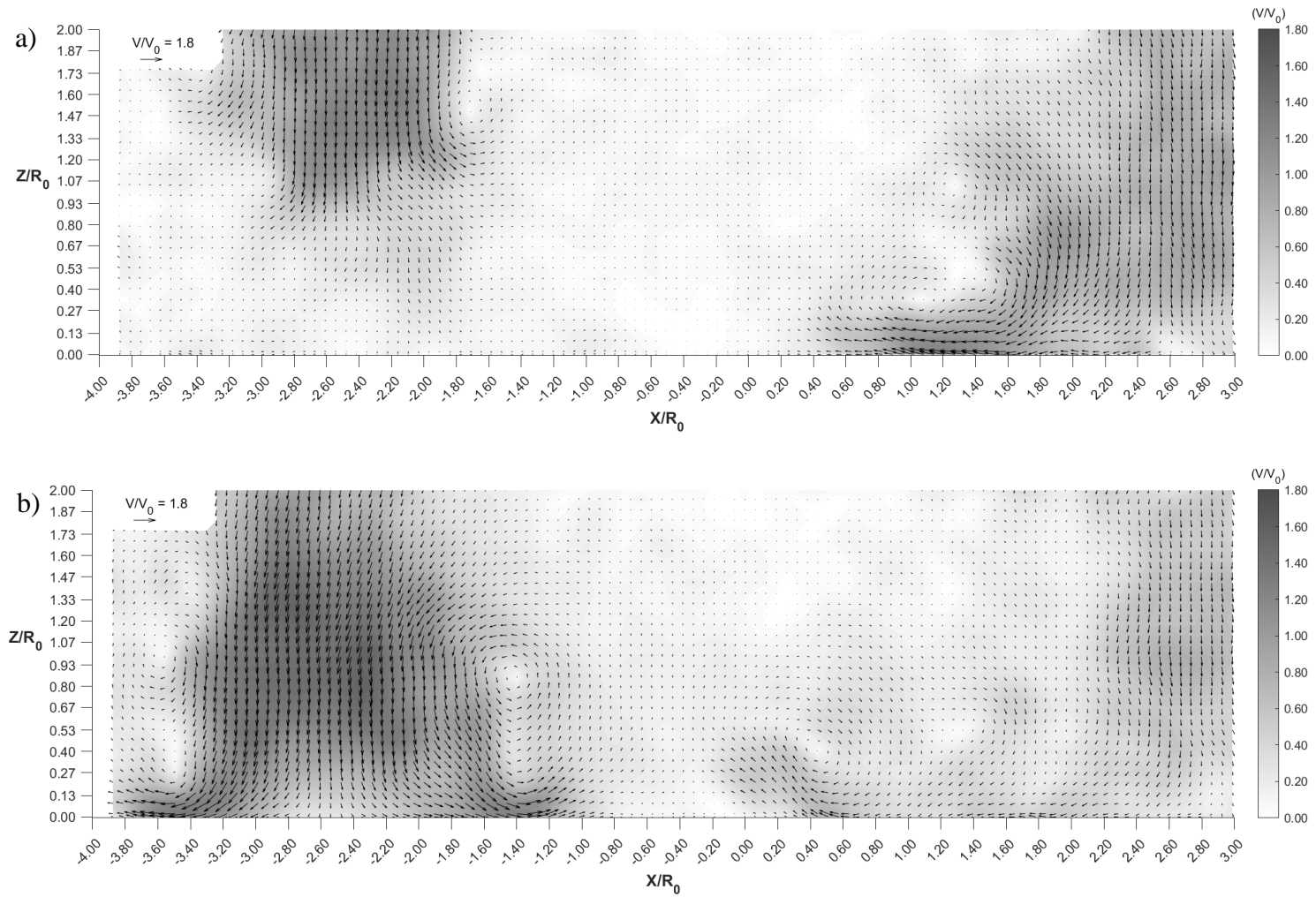
Figure 4-7 - Scaled velocity vectors and contour fields (V/V$_0$) for $\Delta T = 0.37$, X$_d$/R$_0$ = 6.14, (a) t/T$_0$ = 4.60 and (b) at t/T$_0$ = 7.03
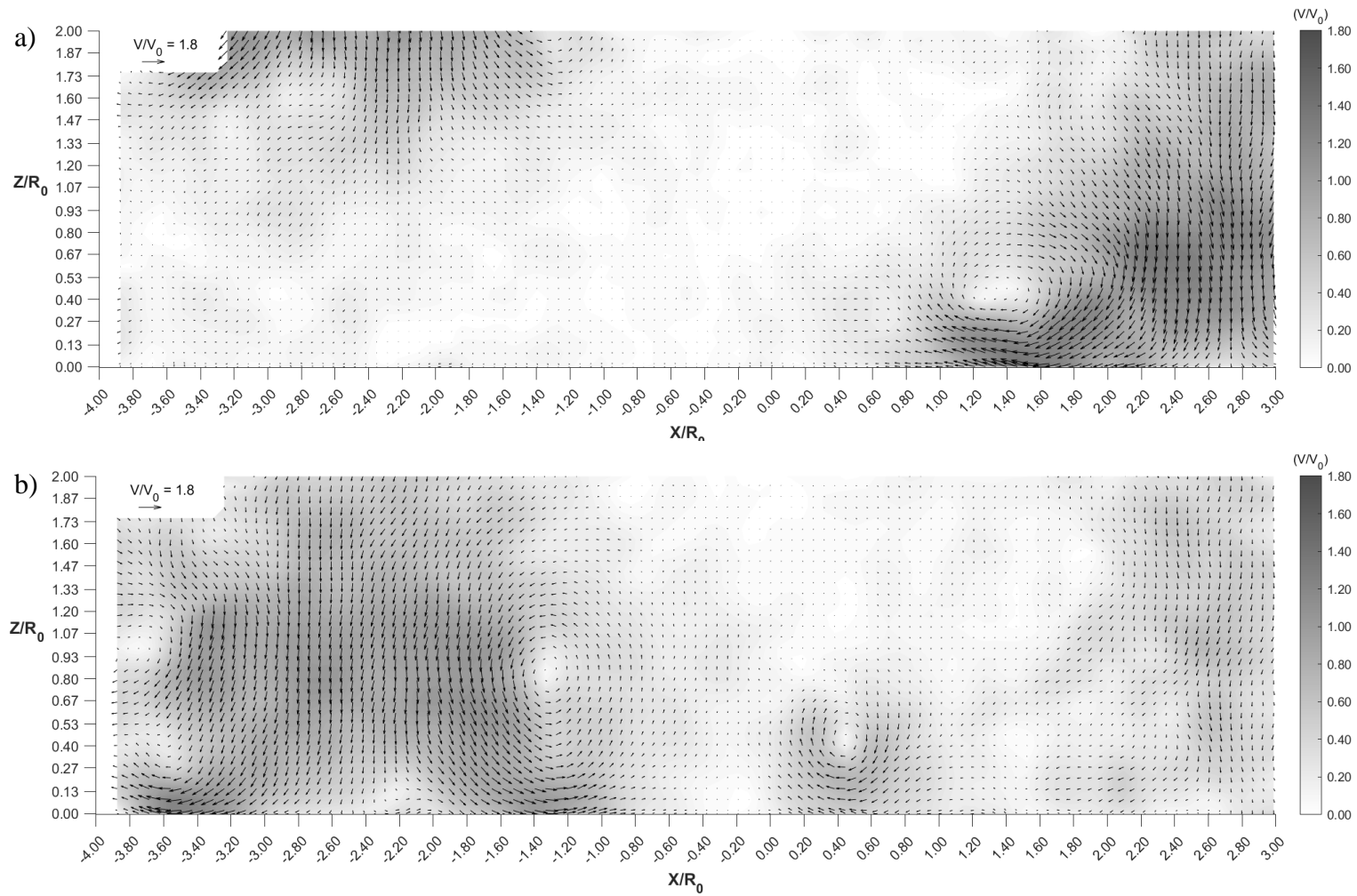
Figure 4-8 - Scaled velocity vectors and contour fields (V/V₀) for ΔT = 0.74, Xₐ/R₀ = 6.14, (a) t/T₀ = 5.41 and (b) at t/T₀ = 8.38

As the time difference (ΔT) is increased, the outflow of the right-hand event reaches close to the left-hand event as the left-hand event impinges the ground. The horizontal roll vortices of each event meet as two counter-rotating vortical structures. The counter vorticity in each forces them upwards, creating high vertical velocities in the interaction region. This upwards convection was detailed in the CS study by Orf et al. (1996). The horizontal speeds in the interaction region are reduced to $u/V_0 = 1.2$, as each event's opposing flow works against each other's outflow. Increasing the timing sees the right-hand events horizontal velocity remains closer to that of a single event.

As noted above, in all spatial and temporal variation cases, the location and magnitude of the maximum radial velocity in the outer radial location of the left-hand release events remain constant. The radial location in consideration is detailed in Figure 4-9.
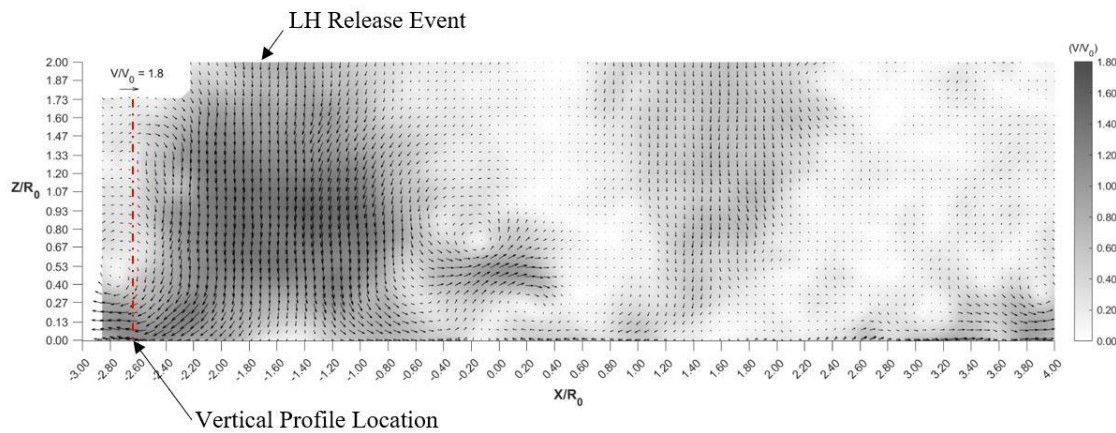
Figure 4-9 – Location of the vertical profiles plotted in Figure 4-10, the location indicated by the red line

The red centre line shows the location of the region under consideration. Each vertical profile at the time and radial location of the maximum radial velocity for the left-hand side of the left-hand release are shown in Figure 4-10. The left-hand event was used as its location between all separation times, and distances relative to the frame of view remained constant.
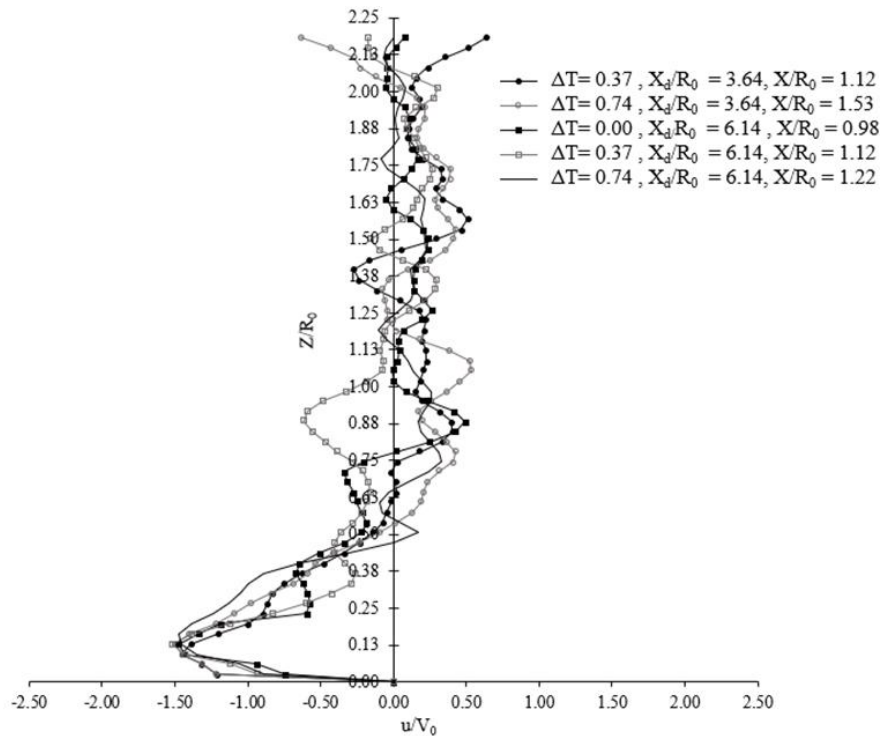
Figure 4-10 – Vertical velocity profiles at the radial location if the maximum radial velocity for both events in each separation distance and time delay, the sign represents direction only

The magnitudes remain close at $u/V_0 = 1.5$, similar to the single releases, and at the same height of $Z/X_0 = 0.14$. The radial locations from their respective event centres deviate between $X/R_0 = 0.8$ to $X/R_0 = 1.5$ but are close to that of a single event. Figure 4-10 shows that horizontal velocities in the outer regions of a downburst line length are uninfluenced by the spatial and temporal variation explored here. A similar conclusion was found by Hjelmfelt (1988) and Orf et al. (1996). Therefore, the outflow in the width of a downburst line is of greater importance to engineers as the velocities in this region is more dependent on the timing and spacing of events in a downburst line.

Investigating the velocity in the width of the outflow of the interaction region was attempted. As noted, though, high out-of-plane motion present in the interaction region limited the quality of PIV images. Only the case of $\Delta T = 0.24$ was possible for both the minimum separation distance and the maximum separation distance as the velocities at these times in the interaction region's outflow is predominately in-plane. Figure 4-11 shows the location of the release cylinders in each of the displayed velocity vector fields.
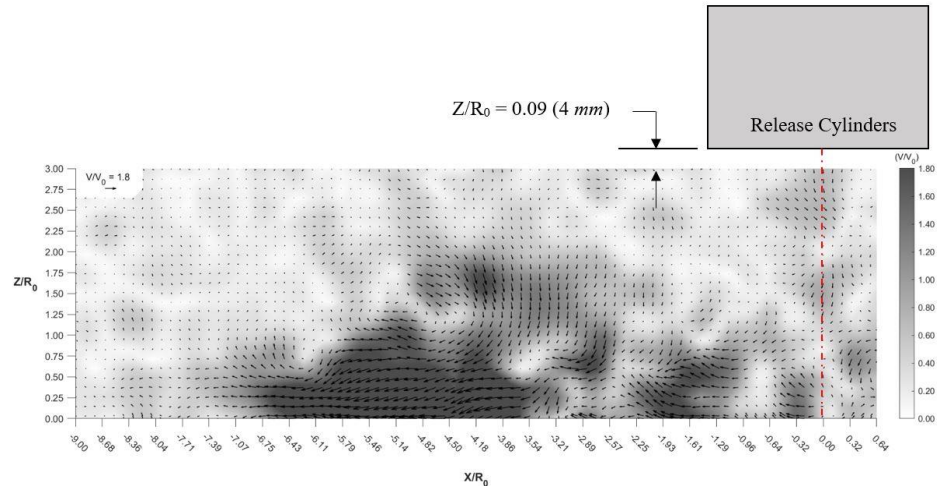
Figure 4-11 – The location of the release cylinders relative to each velocity vector field for Figure 4-12 (a) and (b) and Figure 4-17 (a) and (b)

Figure 4-12 (a) is the velocity vector field in the $\Delta T = 0$ ($T_a = 0.235$) cases at the minimum separation distance. The maximum velocity of $V/V_0 = 3.31$ was recorded at a radial extent of $Y/R_0 = 3.74$ and a height of $Z/R_0 = 0.49$. When scaled, this corresponds to 120 *m/s* at the height of 300 *m*, located 2.3 *km* from the event origin. That is significantly higher in velocity than in the single downburst case and represents 1.51 times the highest value recorded in the Single DB B release case. Even closer to the ground, at $Z/R_0 = 0.14$, horizontal velocities of $V/V_0 = 2.6$ were recorded in the same region. This multiplier in velocity agrees well with Vermeire et al.'s (2011a,b) of 1.55 times that of a single event. Though, as with the single cases, the limitation on the PIV captures' spatial and temporal resolution may mean that the maximum could be outside of the range of images captured and be higher than $V/V_0 = 3.31$. Even a few time steps after, $t/T_0 = 12.46$, the maximum horizontal velocity, high velocities of $V/V_0 = 2.5$ were found (Figure 4-12 b) at distances of $Y/R_0 = 6.3$. In the maximum separation cases, the release cylinders were within $X/R_0 = 1.5$ of the flume sidewalls. This distance to the walls would have caused the outflow to swell and push towards the interaction region and increase the outflow velocity beyond if there were no walls. Therefore, containment was considered erroneous for a separation distance of $X_d (R_0) = 6.14$ in the width plane orientation.
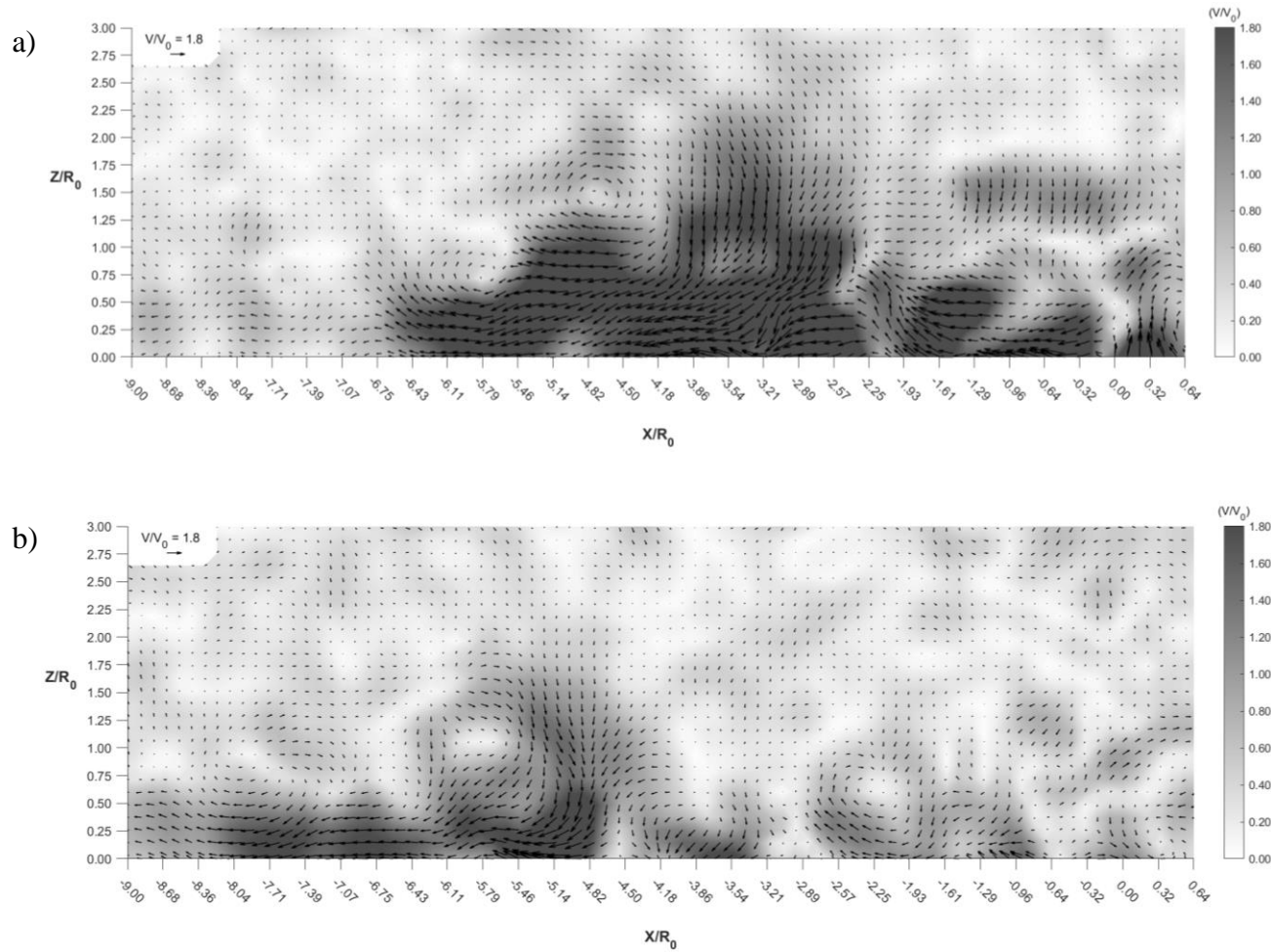
Figure 4-12 - Scaled velocity vectors and contour fields (V/V₀) for ΔT = 0.24, X_d/R_0 = 3.64, (a) t/T_0 = 11.28 and (b) at t/T_0 = 12.46 in the vertical width plane

The instantaneous horizontal velocity profile at the maximum velocity ($Y/R_0 = 3.74$) was added to the profiles shown in Figure 3-14. The horizontal velocity was scaled by the maximum and plotted normalized by the characteristic length R_0. The profile shows that higher velocities exist above $Z/R_0 = 1$ in the outflow in the interaction region of a complex interacting downburst line outflow compared to single events.
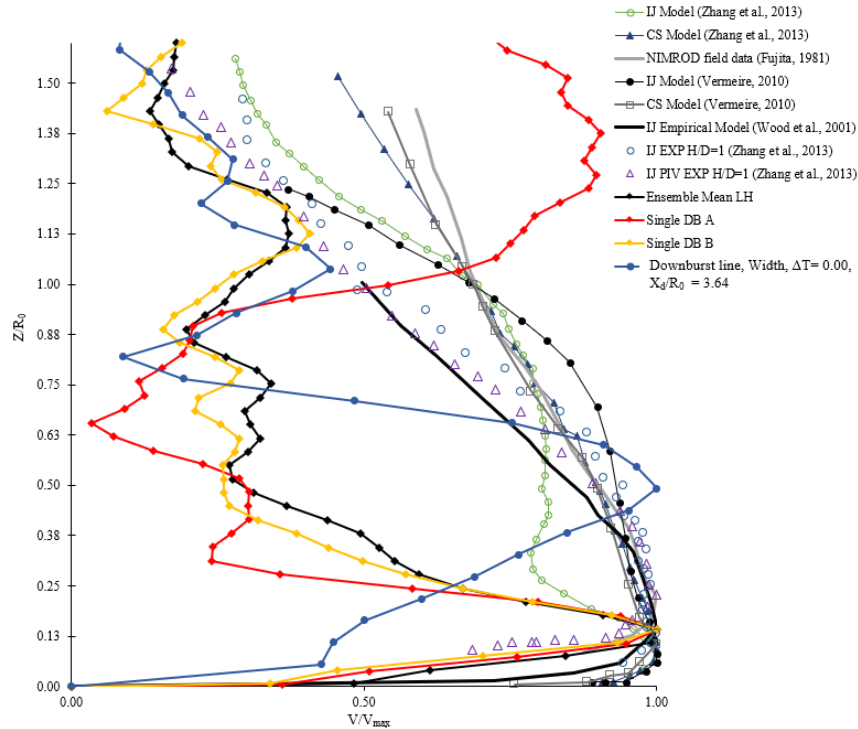
Figure 4-13 – Vertical profiles of normalized velocity at the radial location and time of the maximum velocity for various experimental and numerical works with the $\Delta T = 0.24$, $X_d/R_0 = 3.63$ viewed in the width of the outflow downburst line case

The near-surface part of the profile also contains elevated velocities over that of single events. After the maximum velocity, the slope of the profile indicates this as it decreases less than that of single events. A more detailed, higher resolution study into the near-surface region would better capture the velocities and wind hazards within this outflow area. The profile indicates that high wind loads can be expected below $Z/R_0 = 0.38$ or 250 m.

4.2   Enhanced Fujita (EF) Scaling in the lateral (width) Plane of The Interaction Region

Vermeire et al. (2011b) and Oreskovic et al. (2018) considered the outflow area sizes (also called the maximum surface wind swath) defined by the velocity limits based on the Enhanced Fujita scale (EF) (Fujita 1971, 1981) in the horizontal plane located at the height of the maximum radial velocity. In the case of Vermeire et al. (2011b), the area was defined as a two-dimensional wind plane where the velocity at each point was recorded only for the maximum radial velocity. Vermeire et al. (2011b) used these regions to estimate the damage footprint posed by downburst lines varied in space and time. Oreskovic et al. (2018) expanded that analysis to include an instantaneous capture of the area defined by the EF scale at a specific height above the ground. Oreskovic et al. (2018) compared full-scale CS simulations to the Lundgren et al. (1992) scaling parameters to establish an equivalent length scale, time scale and velocity scale that could be used over the DL191 scaling to find the appropriate scaled velocity values for the equivalent EF0, EF1, and EF2 ratings. Oreskovic (2016) concluded that the Lundgren et al. (1992) scaling parameters were effective at scaling CS events to dense fluid release event data with a modified approach to scaling the density difference. Though the EF scale was explicitly defined for tornadic wind damage, the EF scale used here (as with Vermeire et al. (2011b) and Oreskovic et al. (2018)) is only used as a relative measure to indicate wind speed and not the type of damage the velocities represent. Therefore, the scale is denoted as EFD to indicate the relative measure to wind speed and not wind speed related to tornadic damage.

Near-ground regions that experience EFD0 or greater winds are of interest to Engineers. The Enhanced Fujita scale is a modified version of the Fujita scale (F scale) (Fujita 1971, 1981) that categorizes the damage caused by tornadic events (McDonald and Mehta, 2006). EF0 wind damage occurs from winds between 29 *m/s* to 37 *m/s*, EF1 between 38 *m/s* to 49 *m/s*, and EF2 from 50 *m/s* to 61 *m/s* (McDonald and Mehta, 2006). The EF scale continues to EF5 at over 90 *m/s*, though speeds above the EF2 range are not considered here. Oreskovic's (2016) simulation 008_1200_1800_2000 was selected as the most applicable to this study. The simulation CS centre was located at 2 *km* above the ground matching closely with the release height scaled equivalent of 1.9 *km*

Table 4-2 – table of the scaling parameters for the equivalent CS simulation used to determine the scaled velocities for the definition of EFD0, EFD1, EFD2

Parameter	
$R_0\,[m]$	1337
$T_0\,[s]$	94.55
$V_0\,[m/s]$	16.08
$\Delta\rho/\rho$	0.019

Using an estimation based on Oreskovic's (2016) CS simulation of the velocity scale (V_0) from the full-scale high-resolution CS simulation, the upper-velocity limits of the scaled EFD are tabulated in **Error! Reference source not found.**:

Table 4-3 – Scaled upper EF velocity limits used to define the regions of EFD0, EFD1 and EFD2

	Lower Velocity Limit [m/s]	Upper Velocity Limit [m/s]	Scaled in terms of V_0
EFD0	29	37	1.8 – 2.3
EFD1	38	49	2.4 – 3.0
EFD2	50	61	3.1 – 3.8

The above velocity limits were applied to velocity contours and overlaid on to the velocity vector fields of the horizontal plane's outflow of the interaction region width. Only the $X_d(R_0) = 3.64$ with a time delay between the events of $\Delta T = 0.24$ was investigated. According to Orf et al. (1996) and Vermeire et al. (2011a), this combination represented the most significant hazard.

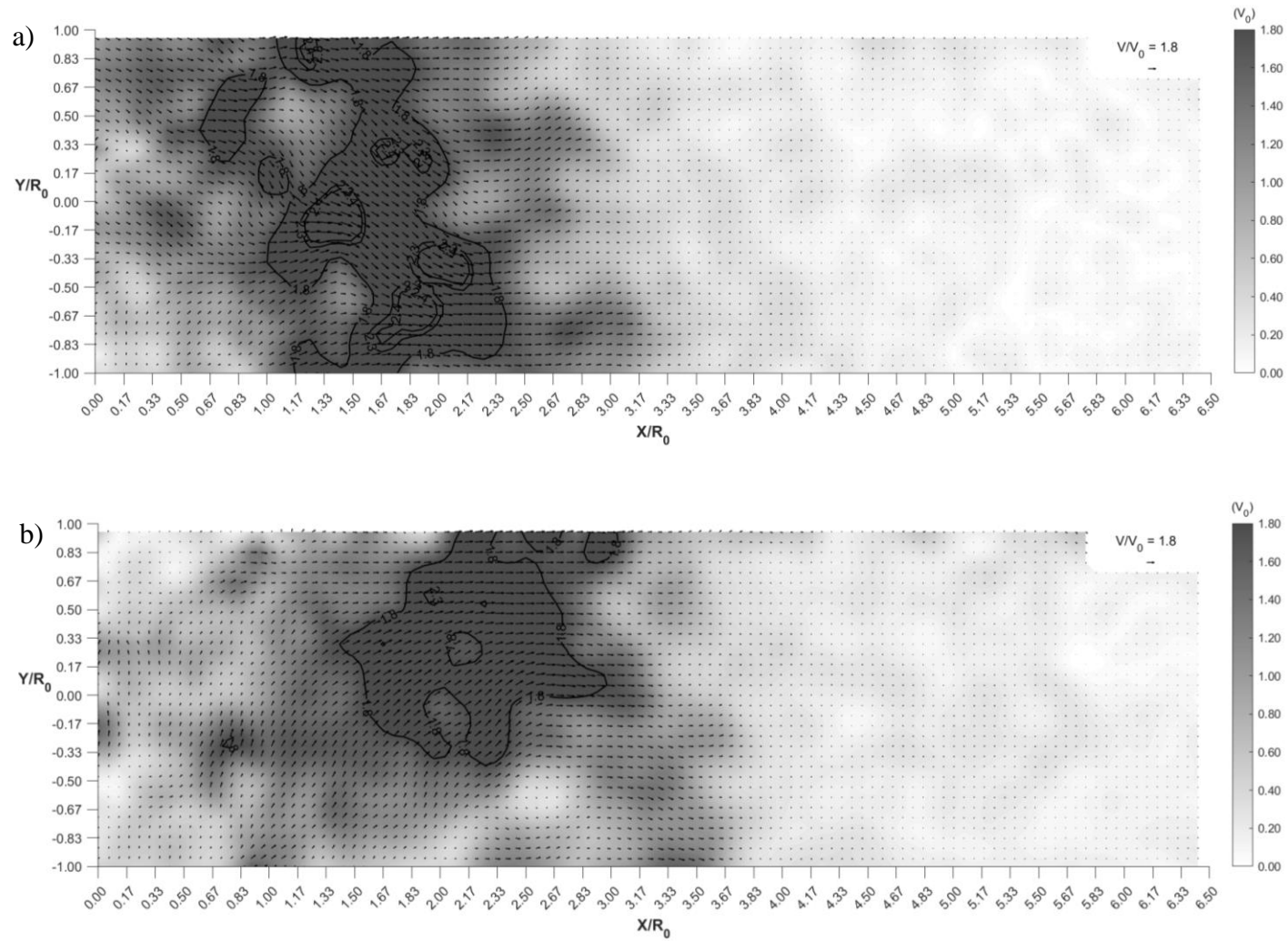**Figure 4-14 - Scaled velocity vectors and contour fields (V/V₀) for X_d(R₀) = 3.64, (a) ΔT = 0.24 , t/T₀ = 9.12 and (b) ΔT = 0.71 at t/T₀ = 12.35**
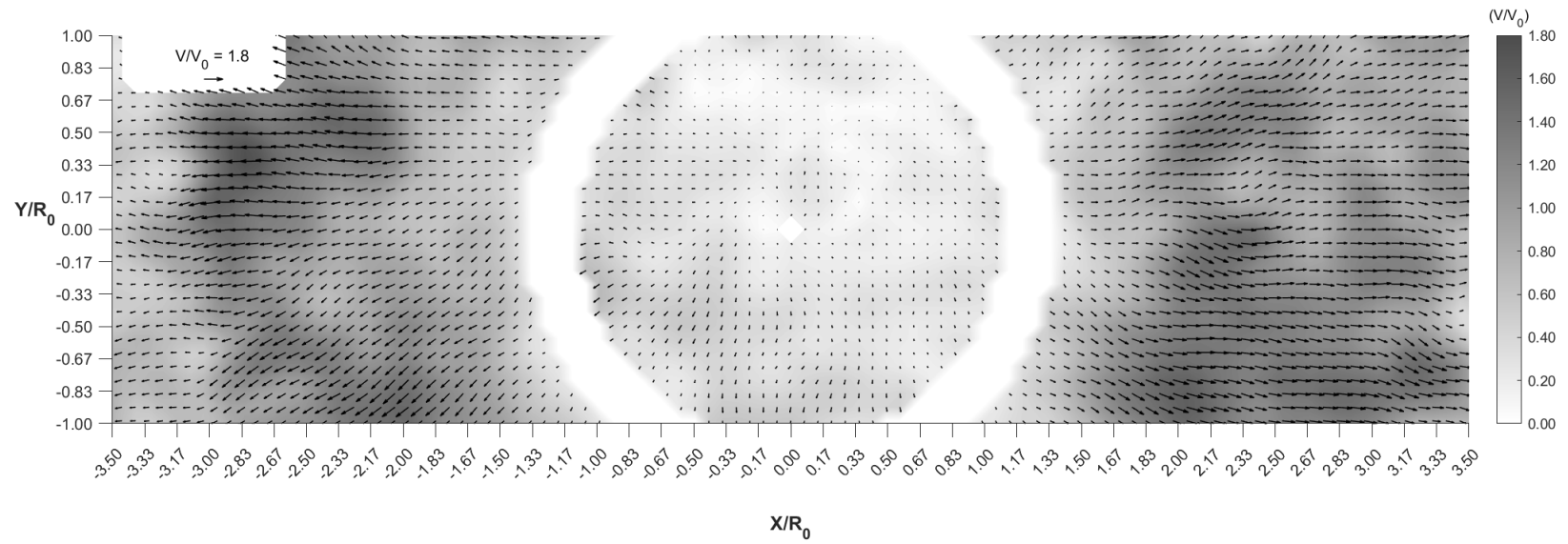
Figure 4-15 - Scaled velocity vectors and contour fields (V/V$_0$) for the single horizontal downburst at t/T$_0$ = 7.84

Figure 4-14 (a) shows the greatest extent of scaled EFD velocities regions in the width of the interaction plane of the close downburst line case at a scaled time delay equivalent to 30 seconds, which represents the greatest outflow in this study. Regions of scaled EFD2 extend up to $X/R_0 = 2.33$. Increasing the time delay to $\Delta T = 0.71$ reduces the extent of scaled EFD1 regions to $X/R_0 = 2.83$. In contrast, the single release event, shown in Figure 4-15, had no regions of scaled EFD or scaled EFD0 speeds. The complex interacting downburst line case at a time delay of zero between the events produced the furthest reaching regions of EFD2. Vermeire et al. (2011b) found that the closest cases (coalescent) produce the largest regions of EFD0 to EFD1 speed. The region's size and extent could be larger at lower or higher heights than reported here. This study used a $Z/R_0 = 0.16$, which was selected based on the maximum radial velocity found in single release cases. A further investigation looking at different heights is recommended to know the full extent to which EFD scaled speeds occur for downburst collisions in downburst lines. Also, this case considers a smooth wall. Surface roughness and topography will have an effect on the extent of high-velocity regions in the outflow.

This study's most exciting features are the horizontal roll vortices that form and interact in the simulated downburst lines' vertical length plan. These horizontal roll vortices are essential to understanding the near-surface velocities resulting from interacting downburst outflow in downburst lines. The next part of this study focuses on tracking the cores of the horizontal roll vortices to understand better how they interact along the ground.

4.3   Vortex Trajectory in The Collision Region of Complex Interacting and Discrete Downburst lines

Unable to use the vertical width plane for analysis using PIV, the vortical structures are considered in the vertical length plane's interaction region. In this interaction region, the collision of the horizontal roll vortices from each event represents a complex region of winds in full-scale events (Orf et al. 1996). The interaction of the horizontal roll vortices caused an increased hazard both in the near-surface of the outflow and higher up AGL.

The left-hand side event's left side horizontal roll vortex trajectory was tracked for this analysis. The left-hand event was chosen as, in all cases, it was the first event released and marked the time in which ΔT was based. The left-hand roll vortex propagated towards the interaction region and collided with the second release event. This collision was the reason why it was selected for tracking its trajectory.

As the analysis for tracking the trajectory of the horizontal roll vortices of the single release events, the lambda two (λ_2) criterion was also used here. The same threshold value ($\delta_\lambda = -40$) was applied to limit the isosurfaces to show only the most substantial vorticity regions.

At the lowest time delay between the events ($\Delta T = 0.24$), the horizontal roll vortices collided at the separation distance's halfway mark. Both horizontal roll vortices exist as contour rotating structures, and when they collided at $\Delta T = 0$, they force each other upwards away from the ground plane. Figure 4-16 (a) at X_d (R_0) = 3.64 and Figure 4-19 at X_d (R_0) = 6.14 show the collision and lifting of the roll vortices at $\Delta T = 0.24$. For the separation distance of X_d (R_0) = 6.14, the same can always be observed for the range of times investigated (Figure 4-19). At a separation distance of X_d (R_0) = 3.64, increasing the time delay forces the second event to fall on to the vortex roll of the first (Figure 4-17 and Figure 4-18); this forces the horizontal roll vortex of the first event close to the ground.

Figure 4-16 - Scaled velocity vectors and contour fields (V/V$_0$) for $\Delta T = 0.24$, X$_d$ (R$_0$) = 3.64, (a) t/T$_0$ = 4.60 and (b) at t/T$_0$ = 8.38

Figure 4-17 - Scaled velocity vectors and contour fields (V/V_0) for $\Delta T = 0.37$, X_d $(R_0) = 3.64$, (a) $t/T_0 = 7.57$ and (b) at $t/T_0 = 8.38$
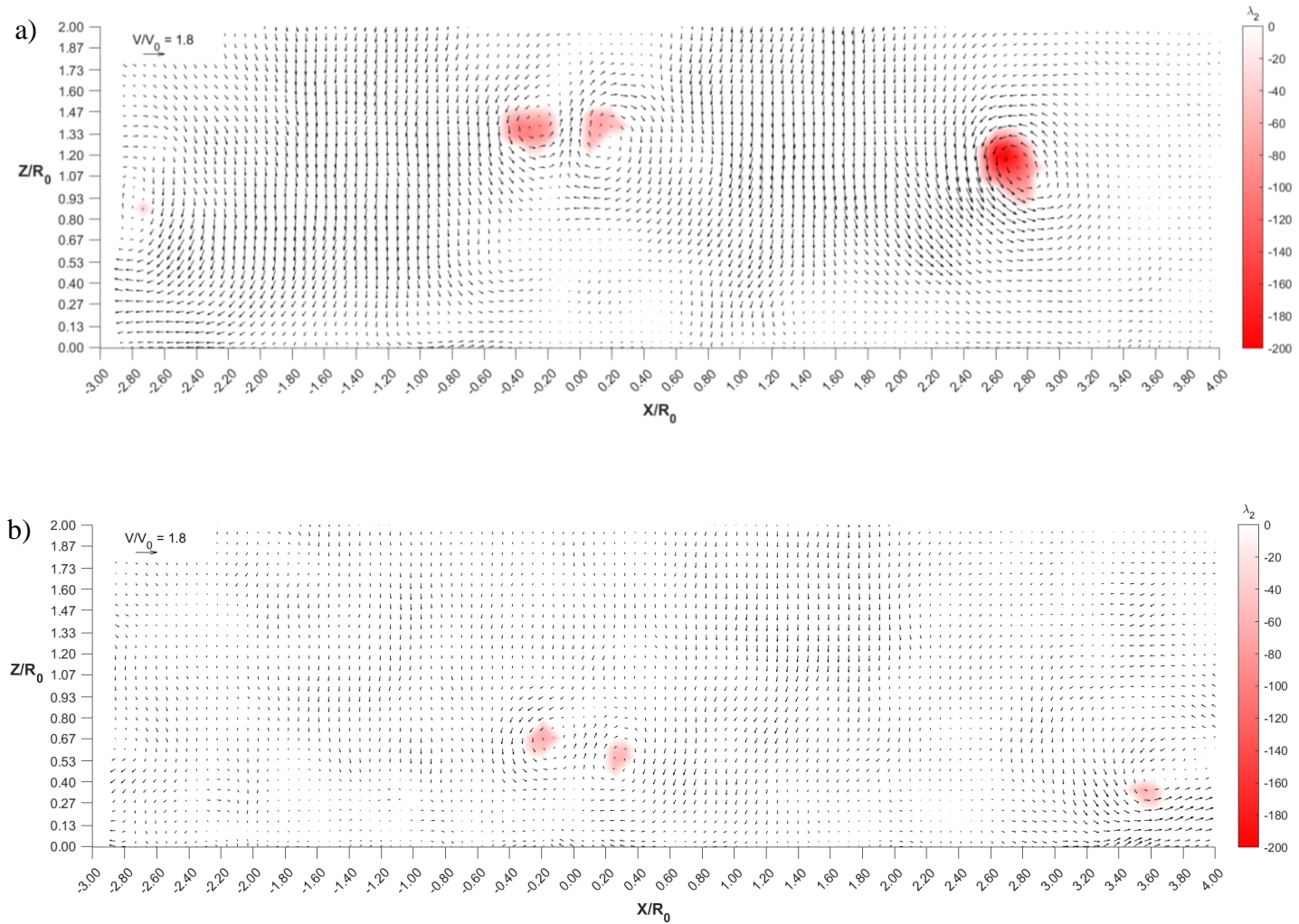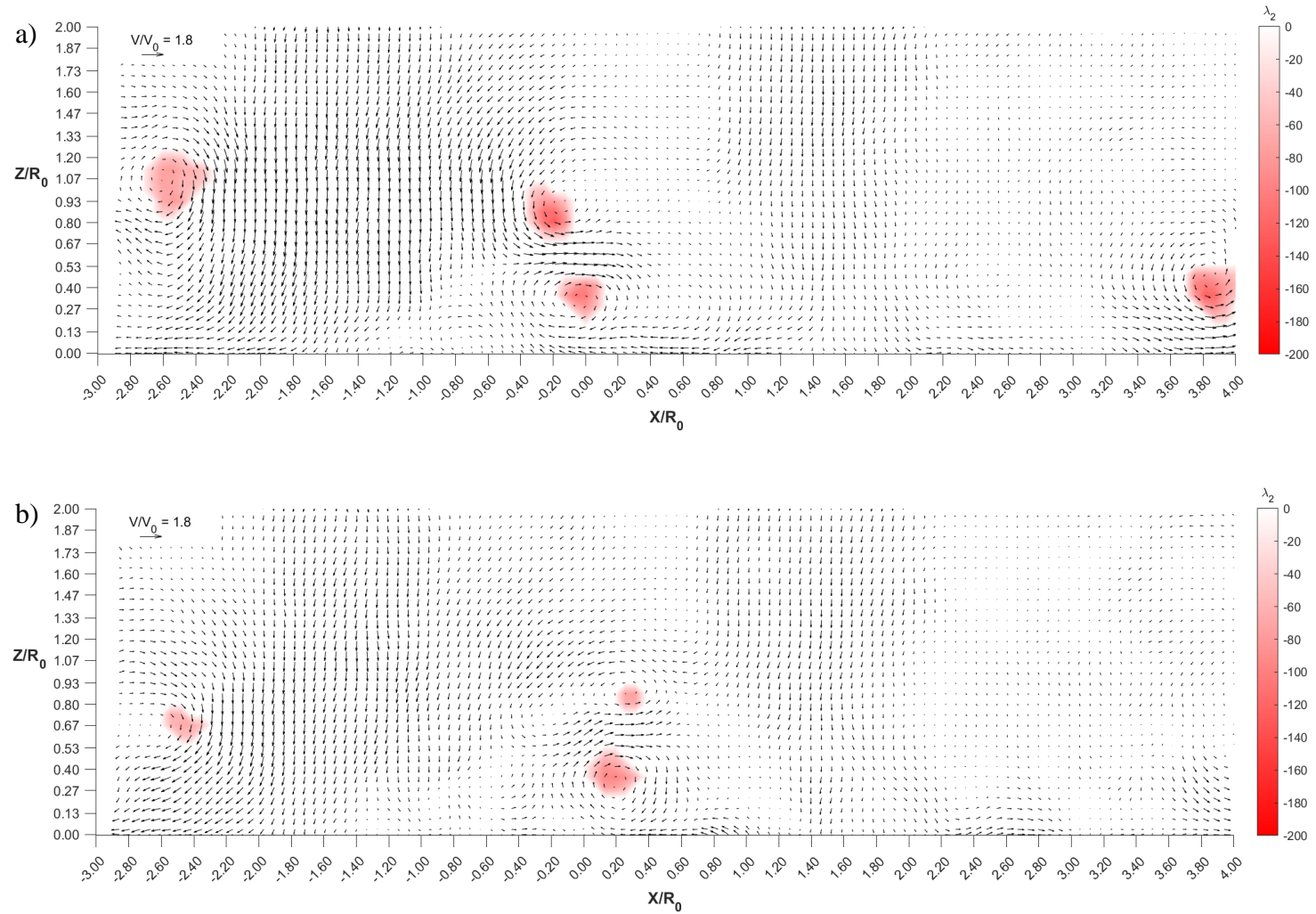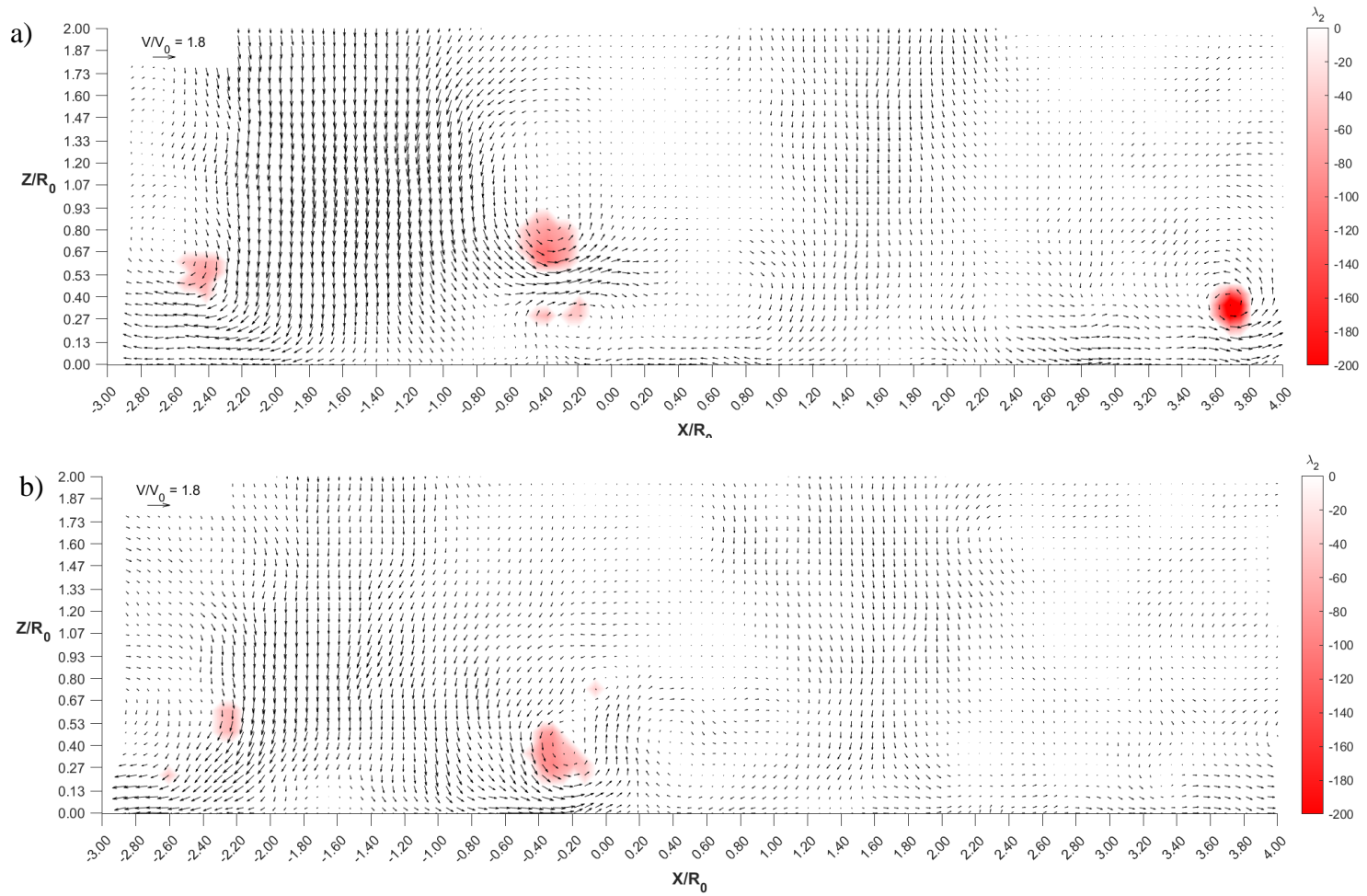
Figure 4-18 - Scaled velocity vectors and contour fields (V/V$_0$) for $\Delta T = 0.74$, X$_d$ (R$_0$)= 3.64, (a) t/T$_0$ = 7.57 and (b) at t/T$_0$ = 8.92
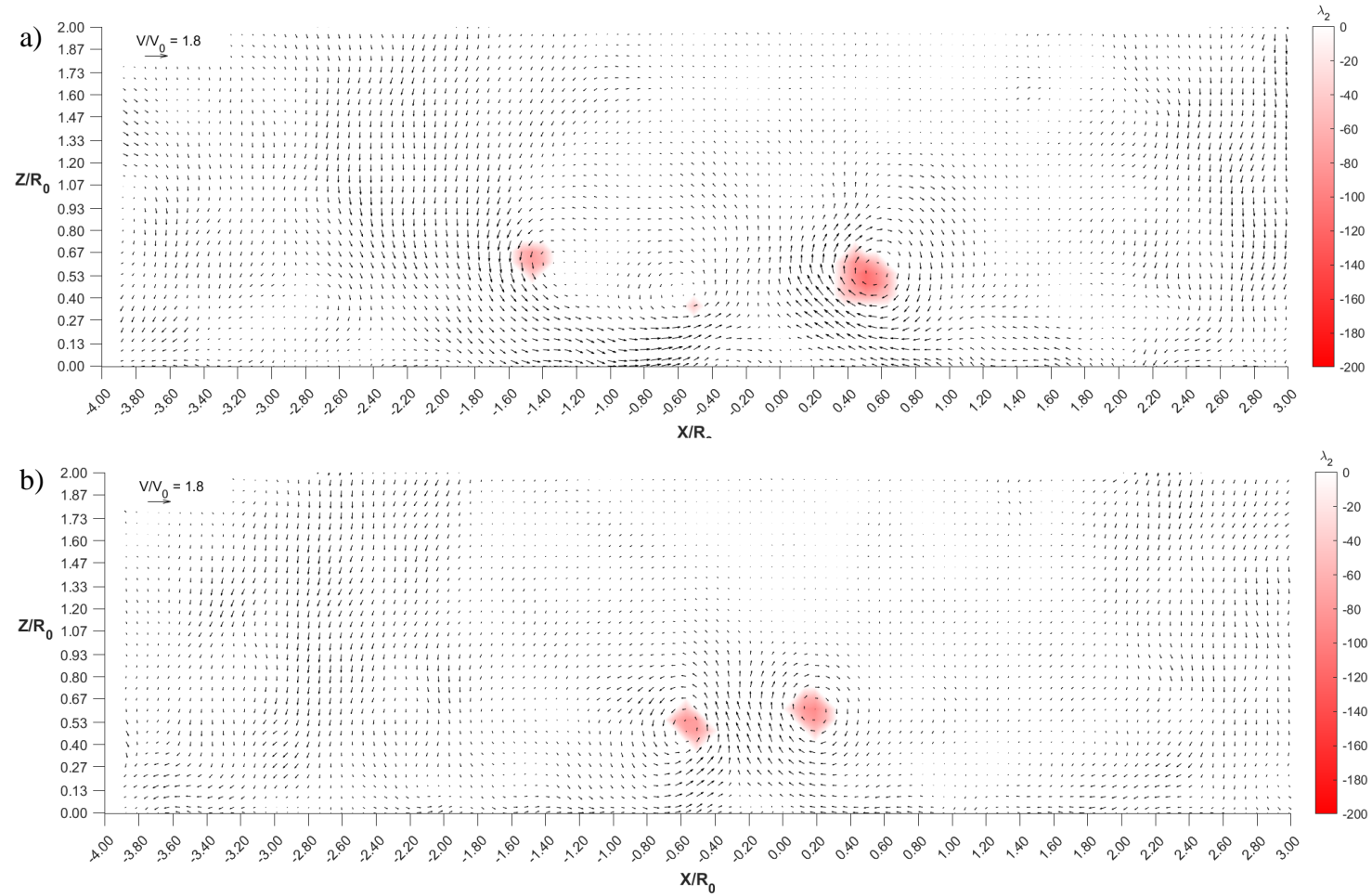
Figure 4-19 - Scaled velocity vectors and contour fields (V/V₀) for ΔT = 0.74, X_d (R_0) = 6.14, (a) t/T_0 = 7.57 and (b) at t/T_0 = 9.73

The trajectory of the close release cases was tracked only for $\Delta T = 0.37$ and $\Delta T = 0.74$. The horizontal roll vortex remains in place for the zero-time delay case, falling slowly due to gravity. The counter vorticity from the other event's vortex roll reduces the speed at which they both fall. Figure 4-20 shows the trajectory of the vortex roll core for the left-hand event through the interaction region the time delays of $\Delta T = 0.37$ and $\Delta T = 0.74$ at the close separation distance of X_d $(R_0) = 3.64$. Figure 4-20 (a) tracks the vortex core height (Z) scaled by R_0 as a function of scaled distance (X/R_0) from the event centreline and Figure 4-20 (B) the scaled height along scaled time (t/T_0).

Figure 4-20 – (a) the scaled roll vortex height to distance from the event centreline over the time series of the release events shown in (b), the time history of vortex height for both time delays of $\Delta T = 0.37$ and $\Delta T = 0.74$ with the single reference case Single DB B

In Figure 4-20 (a), the roll vortex is forced down as it collided with the second release's outflow. As the outflow increased in strength, the vortex roll is forced back along the path it travelled before colliding with the second event outflow. Increasing the time delay allows the vortex roll to weaken before colliding with the second event's outflow. The weakened vortex roll is forced closer to the ground over the shorter time delay while being forced

back. As the outflow from the second release collides with the first, the near-surface velocities are reduced in both cases. The reduction occurs as both outflows oppose each other. The interaction in this close case suggests that the outflow in the close case at the shortest time in the width plane would have a unique outflow comprised of two merging vortices (Orf et al. 1996). Applying the normalizing method explored in chapter 3 (Chowdhury, 2019), Figure 4-21 (a) shows the vortex core height (Z) normalized by the min-height (Z_{min}) as a function of time normalized by the time of maximum radial velocity (T_{max}). Figure 4-21 (b) height (Z) normalized by the min-height (Zmin) as a function of time the time at the minimum vortex core height (T_{min}).
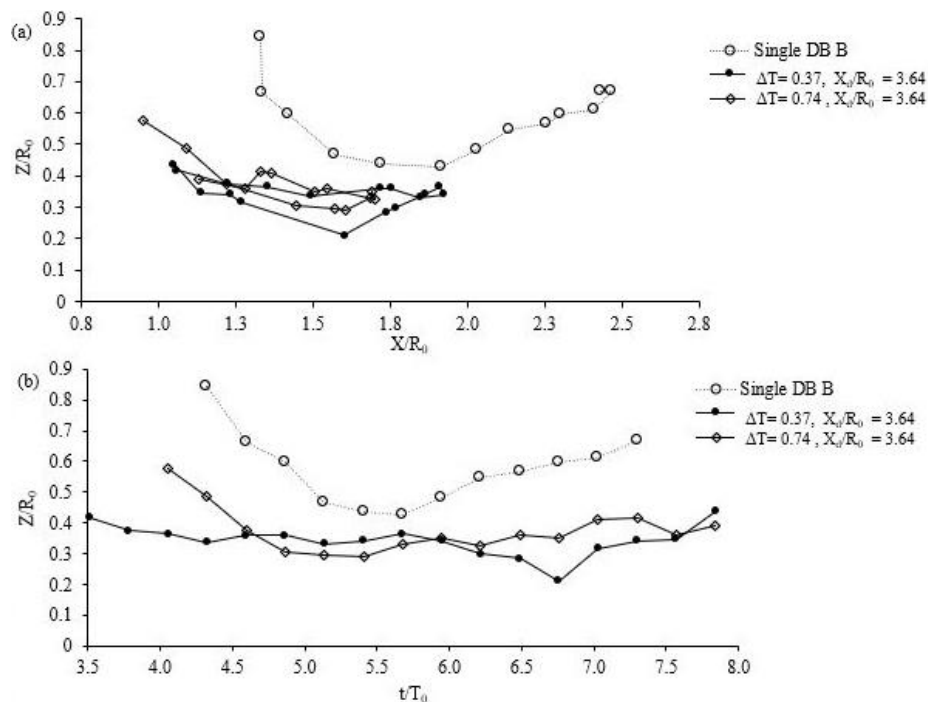

Figure 4-21 - (a) the scaled roll vortex height to distance from the event centreline over the time series of the release events shown in (b), the time history of vortex height for both time delays of ΔT = 0.37 and ΔT = 0.74 with the single reference case Single DB B

Normalizing by both the time of the maximum radial velocity (Figure 4-21 a) and the time of the minimum vortex height (Figure 4-21 b) accentuates the suppression of the vortex core height by the second release as the time delay is increased.

Tracking the horizontal roll vortices over ΔT = 0.24, ΔT = 0.37 and ΔT = 0.74 for the separation distance to X_d (R_0) = 6.14, supports the interaction in discrete events leads to

the vortices lift off the ground. Figure 4-22 (a) tracks the vortex core height (Z) scaled by R_0 as a function of scaled distance (X/R_0) from the event centreline and Figure 4-22 (b) height along scaled time (t/T_0).

Figure 4-22 - (a) the scaled roll vortex height to distance from the event centreline over the time series of the release events shown in (b), the time history of vortex height for both time delays of $\Delta T = 0.37$ and $\Delta T = 0.74$ with the single reference case Single DB B

The vortex cores follow nearly the same path as that of the single release experiment, as seen in Figure 4-22 (a) between $X/R_0 = 1.1$ to 2.3 and (b) from $t/T_0 = 5.0$ to 7.5. As the time delay is increased from $\Delta T = 0.37$ and $\Delta T = 0.74$, the lift from counter vorticity from the second release event is more evident Figure 4-22 (a) at $X/R_0 = 2.6$ and Figure 4-22 (b) at $t/T_0 = 9.5$. Normalizing by both the time of the maximum radial velocity (Figure 4-23 a) and the time of the minimum vortex height (Figure 4-23 b) shows that the outflow at a separation distance X_d (R_0) = 6.14 leads to discrete Soliton like events, as shown by Hjelmfelt (1987) and Orf et al. (1996).
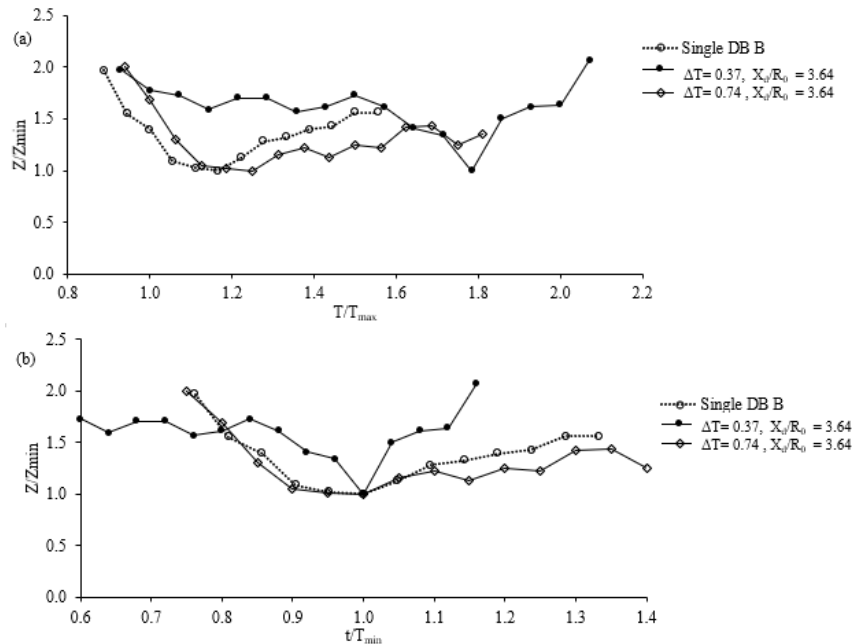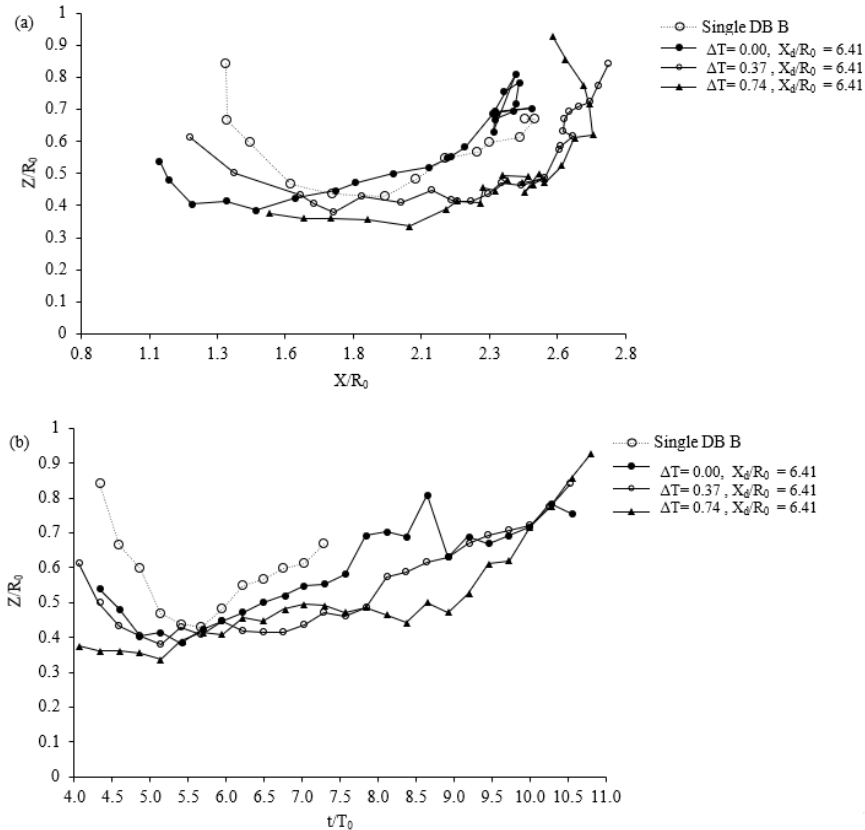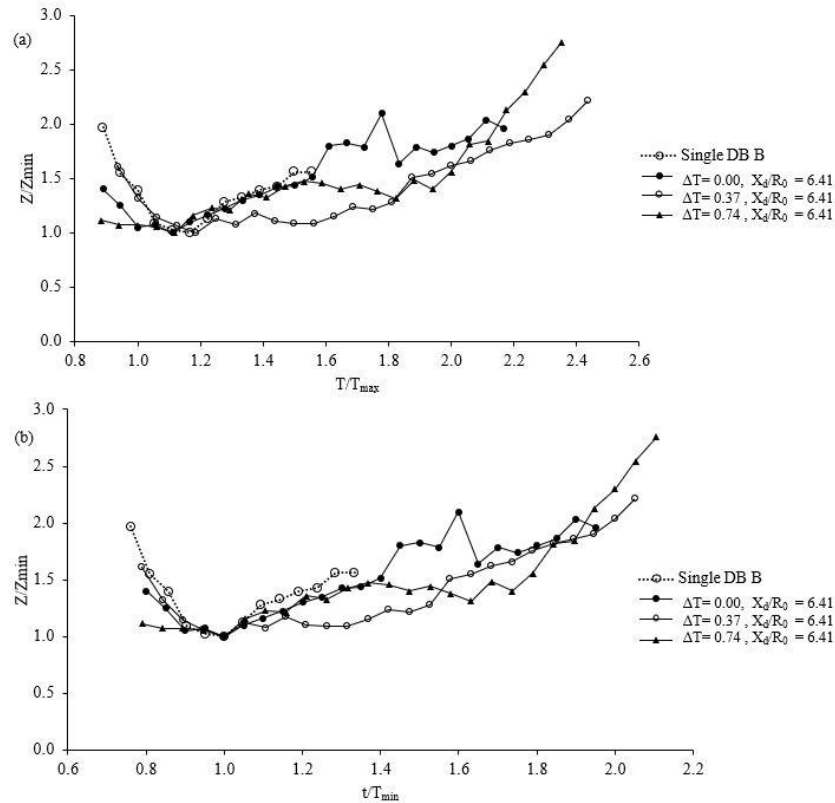
Figure 4-23 - (a) the scaled roll vortex height to distance from the event centreline over the time series of the release events shown in (b), the time history of vortex height for both time delays of ΔT = 0.37 and ΔT = 0.74 with the single reference case Single DB B

All the time delays studied scale to an agreeable fit with the single release DB B in both scaling time by the time of the maximum radial velocity and by the time of the minimum roll vortex core height. The agreement is seen after impingement from T/T_{max} from 1 to 1.6 (Figure 4-23 a), and T/T_{min} of 1 to 1.4 (Figure 4-23 b).

4.4   Summary

The addition of a second release cylinder to simulate the interaction of two downbursts as part of a downburst line has created the 1st experimental data set of this type. Three orientation planes, two in the vertical and one in the horizontal, were used to observe the outflow velocities and horizontal roll vortex structure. Two separation distances of Xd (R_0) = 3.64 and 6.14 were used in conjunction with three delays of ΔT = 0.24, 0.37, and 0.71 to

investigate how spatial and temporal variation affects the interaction of downbursts in downburst lines to support the numerical works of Vermeire et al. (2011a,b) and Orf et al. (1996). A limited field of view combined with significant cross-plane motion limited the analysis to the following conclusions:

1. Varying the separating distance between X_d (R_0) = 3.64 to X_d (R_0) = 6.14 and changing the delay time between $\Delta T = 0.24$ to $\Delta T = 0.71$ did not affect the location of the maximum radial velocity in the vertical length plane of the interaction of the outflow for the left-hand side of the left-hand event. The velocity magnitude radial location and height above the ground was found to be similar to that of a single downburst event. This similarity provided experimental proof that the lateral vertical plane (width plane) contains the most significant outflow dynamics.

2. In the case (X_d (R_0) = 3.14, ΔT=0.24) closest to Vermeire et al.'s (2011a) and case with the highest amplification factor (equivalent to X_d (R_0) $\approx$ 1.9, at $\Delta T \approx$ 0.19), the highest velocity in the width plane of the outflow was amplified by V_{max}/V_{base} = 1.5 of that of a single release event. This amplification in velocity magnitude remained close to Vermeire et al.'s (2011a), considering that the release separation distance and time delay were larger in this study. The location was found to be $X/R_0 = 3$, approximately twice that of a single event.

3. At separation distances X_d (R0) > 6, the near-surface velocities in the outflow interaction region of simulated downburst lines are no more significant than that of single downburst events. The interaction of the two release events followed the form of discrete downburst events with Soliton like features and provided experimental support to the observations of Hjelmfelt (1987) and Orf et al. (1996).

4. Regions of EF_+2 were found to extend out $X/R_0 = 1.5$ further than any other time or spacing variation than a time delay of ΔT=0.24 and close separation distances of X_d (R_0) = 3.14.

5. Tracking the vortex core of the left-hand event over the interaction region showed that the events are discrete at a far enough separation distance. At distances closer

than $X/R_0 = 6.14$, the vortex core was pushed toward the ground by the second event. When separation delay times are close to zero, the counter-rotating vortices' interaction produces high vertical velocities above the ground at a scaled height of 400 m.

4.5   References

Chowdhury, J., 2018. Transient analysis of full scale and experimental downburst flows. MESc. Dissertation, The University of Western Ontario, Canada.

Hjelmfelt, M. R., 1987. The Microbursts of 22 June 1982 in JAWS. J. Atmos. Sci., 44, 1646-1665.

Holmes, J.D., Oliver, SE., 2000. An empirical model of a downburst. Eng. Struct. 22, 9, 1167-1172.

McCarthy, J., Wilson, J., Fujita, T.T., 1982. The joint airport weather studies project. Bulletin of the American Meteorological Society. 63, 15-22.

McCarthy, M.M., 1996. Severe weather elements associated with September 5, 1996, hydro tower failures near Grosse Isle, Manitoba, Canada. Manitoba Environmental Service Centre, Environment Canada, 21.

McCarthy, J., Wilson, J., 1986. Classify, locate and avoid wind shear (CLAWS) project at Denver's international airport: operational testing of terminal weather hazard warnings with emphasis on microburst wind shear, American Institute of Aeronautics and Astronautics Monographs 32, 17-26.

Oreskovic, C., 2016. Numerical investigation of full-Scale thunderstorm downbursts: a parametric study and comparison to meteorological model. MESc. Dissertation, The University of Western Ontario, Canada.

Oreskovic, C., Orf, L.G., Savory, E, 2018. A parametric study of downbursts using a full-scale cooling source model. J. Wind. Eng. and Ind. Aerodyn. 180, 168-181.

Orf, L.G., Anderson, J.R., Straka, J.M., 1996. A three-dimensional numerical analysis of colliding microburst outflow dynamics. J. of the Atmos. Sci. 53, 2490-2511.

Vermeire, B.C., Orf, L.G., Savory, E., 2011a. Improved modelling of downburst outflows for wind engineering applications using a cooling source approach. J. Wind. Eng. Ind. Aerodyn. 99, 801-814.

Vermeire B.C., Orf, L.G., Savory, E. 2011b. A parametric study of downburst line near-surface outflows. J. Wind. Eng. Ind Aerodyn., 99, 226-238.

Vermeire, B.C., 2010. Numerical modeling of thunderstorm downbursts and downburst lines. MESc. Dissertation, The University of Western Ontario, Canada.

Chapter 5

5   Conclusions and Recommendations

This thesis's objective was to provide the first experimental study of downburst lines modelled as a collision between two downburst events to support the numerical work completed by Vermeire et al. (2011b) and Orf et al. (1996). The dense fluid release model (Lundgren et al., 1992) was used to recreate the scaled downburst outflows as the technique utilized density to recreate the mechanism of baroclinic vorticity generation. Numerical studies by Vermeire et al. (2011a) and Vermeire (2010), along with experimental and numerical studies by Zhang et al. (2013), demonstrated the difference in using momentum-based simulations compared to density-driven models. The near-surface buoyance gradient in the density-driven models increased the baroclinic vorticity generation leading to the high near-surface velocities. The dense fluid release model was used with PIV captures in both a vertical and horizontal orientation plane to resolve the velocity vector fields for both single downbursts and downbursts line events using a new release cylinder design. The new release cylinder design incorporated sidewall gates with the intent of reducing the wall effect compared to past dense fluid studies of Lundgren et al. (1992), Alahyari (1995), Yoa and Lundgren (1996).

The new cylinder design's outflow velocity vector field was evaluated prior to conducting the two event-based downburst collision simulating a downburst line in the first phase of this study. Comparing the outflow to data available from Alahyari (1995) proved that the new design produced weaker outflows, presumably due to the onset of initial mixing (Babaei, 2018). An agreement based on the maximum radial velocity's magnitude and the location was found in the Single DB B release case to past dense fluid releases, numerical work, and field study data. In addition, the propagation of the fronts' vertical descent and horizontal radial expansion matched to past experiments by use of an acceleration threshold based on the velocity vector fields. However, there was a noticeable asymmetry in the volume of outflow about the centreline of the cylinder. This was attributed to an error in the release mechanism setup. The importance of using modelling techniques that capture the buoyancy forcing of actual downburst events, especially in studies that consider the

near-surface velocities at times and locations after the maximum radial velocity, was supported by tracking the horizontal roll vortex core trajectory using the core diameter to centre height aspect ratio. The mapped trajectory of all single releases supported the conclusions by Vermeire et al. (2011) and Vermeire (2010). Velocity vector captures in the horizontal plane were performed by limited by the field of view available from the flumes structure. The release cylinder could only be centred in the field of view showing just the left-hand and right-hand outflow on either side of the cylinder. The entire outflow around the cylinder could not be captured.

Once the velocity vector field from the outflow of the new cylinder design was characterized, a study of thunderstorm downburst lines was performed using the same dense fluid release model. The downburst outflows were simulated to recreate the complex interacting and Soliton like interactions described by Orf et al. (1996) and the homogenous and discrete downburst line conditions described by Hjelmfelt (1987). The experimental outflows simulating a discrete line following a Soliton like an outflow interaction were found to support the conclusion that the outflows interact with no elevation in near-surface velocities over that of a singular event. The outflow in the length of a downburst line remains unaffected by the collision of its constituent events, and that the majority of the outflow from the interaction is directed into the lateral width plane. Observing the velocity vector fields from the releases simulating a complex interacting collision of a homogenous downburst line was able to support Orf et al.'s (1996) and Vermeire et al.'s (2011b) observation that under certain temporal and spatial variations, the interaction of downburst outflows in the collision region develop a strong horizontal component of velocity (higher than a single event in the near-surface region) that covers a larger radial extent with higher velocities above the height of the maximum velocity.

5.1   Recommendations

The following recommendations for future studies available to the wind engineering community based on this work are provided below:

1. Buoyancy driven experiments as detailed in this study and in the studies of Babaei (2018) along with numerical models that use the cooling source method (Vermeire

et al., 2011a,b; Oreskovic et al., 2018) should continue to be used in the investigation of the near-surface wind hazards posed by downburst events. These techniques capture the buoyancy forcing present in downburst events and thus allow an opportunity to further understand the actual mechanism that causes the increased near-surface wind speeds of downbursts.

2. Continue the investigation to the effect of the added wall porosity in the new cylinder design, as noted here and in Babaei (2018).

3. Expand the current experimental set-up to include a third release cylinder to investigate the spatial and temporal effects of a two-event downburst line as affected by the outflow of a third external event.

4. Include translation and ambient flow into the two-event-based dense fluid release experiments to simulate different atmposheric conditions that affect the strength of a downburst line outflow.

5. Investigate the possibility of adding mirrors to the current setup to allow for larger fields of view for capturing the outflow of two event-based downburst lines.

6. Employ the stereoscopic PIV technique to resolve 3-D velocity vector fields in the collision region of the release events. This would allow for a better understanding of the velocity fields and vortical structures that form from the collision of temporally and spatially varied events used to simulate a downburst line.

5.2   References

Alahyari, A., 1995. Dynamics of laboratory simulated microbursts. Ph.D. Dissertation, University of Minnesota.

Babaei, R., 2018. Experimental simulation of density-driven thunderstorm downbursts. MESc. Dissertation, The University of Western Ontario.

Hjelmfelt, M. R., 1987. The Microbursts of 22 June 1982 in JAWS. J. Atmos. Sci., 44, 1646-1665.

Lundgren, T.S., Yao, J., Mansour, N.N., 1992. Microburst modelling and scaling. Journal of Fluids Mechanics 239, 461-488.

Oreskovic, C., Orf, L.G., Savory, E, 2018. A parametric study of downbursts using a full-scale cooling source model. J. Wind. Eng. and Ind. Aerodyn. 180, 168-181.

Orf, L.G., Anderson, J.R., Straka, J.M., 1996. A three-dimensional numerical analysis of colliding microburst outflow dynamics. J. of the Atmos. Sci. 53, 2490-2511.

Vermeire, B.C., Orf, L.G., Savory, E., 2011a. Improved modelling of downburst outflows for wind engineering applications using a cooling source approach. J. Wind. Eng. Ind. Aerodyn. 99, 801-814.

Vermeire B.C., Orf, L.G., Savory, E. 2011b. A parametric study of downburst line near-surface outflows. J. Wind. Eng. Ind Aerodyn., 99, 226-238.

Vermeire, B.C., 2010. Numerical modeling of thunderstorm downbursts and downburst lines. MESc. Dissertation, The University of Western Ontario, Canada.

Yao, J., Lundgren, T.S., 1996. Experimental investigations of microbursts. Experiments in Fluids. 21, 17-25.

Zhang, Y., Hu, H., Sarkar, P.P., 2013. Modelling of microburst outflows using impinging jet and cooling source approaches and their comparison. Eng. Struct. 56, 779-793.

Curriculum   Vitae

Name: Kyle   Graat

Post-secondary   The University of Western Ontario
Education and   London, Ontario, Canada
Degrees: 2013-2017 B.E.Sc.

                             Fanshawe Colledge
                             London, Ontario, Canada
                             2009-2012 Diploma Mech. Eng. Tec.

Related Work   Teaching Assistant
Experience   The University of Western Ontario
                             2017-2019

Publications:

R.B. Koli, K. Graat, C. Chan, E. Savory. (2017). Characterizing the liquid release mechanism performance in the experimental simulation of density-driven thunderstorm downburst. Environmental Fluid Mechanics. Submitted.

Sarkar D, Graat K & Savory E. (2017). Effect of free-stream turbulence on flat plate heat transfer", Univ. Windsor, Ontario, Canada, June. 25th Annual Conference of the CFD Society of Canada. Proc 25th Annual Conference of the CFD Society of Canada.